DISCLAIMER

IS-T--1409

DE91 000740

Synchrotron Radiation Photoemission Study of Metal Overlayers o Hydrogenated Amorphous Silicon at Room Temperature

by

Pi, Jonathon

PHD Thesis submitted to Iowa State University

Ames Laboratory, U.S. DOE

Iowa State University

Ames, Iowa 50011

Date Transmitted: September 21, 1990

PREPARED FOR THE U.S. DEPARTMENT OF ENERGY

UNDER CONTRACT NO. W-7405-Eng-82.

Synchrotron radiation photoemission study of metal overlayers on hydrogenated amorphous silicon at room temperature

by

Tun-Wen Pi

A Dissertation Submitted to the
Graduate Faculty in Partial Fulfillment of the
Requirements for the Degree of
DOCTOR OF PHILOSOPHY

Department: Physics
Major: Solid State Physics

Approved:

David W. Lynch
In Charge of Major Work

David W. Lynch
For the Major Department

For the Graduate College

Members of the Committee:

Thomas A. Weber

Ronald Fuchs

D K Finnemore

P. A. Thiel

Iowa State University
Ames, Iowa

1990

TABLE OF CONTENTS

Synchrotron radiation photoemission study of metal overlayers on hydrogenated amorphous silicon at room temperature

Tun-Wen Pi

Under supervision of David W. Lynch

From the Department of Physics

Iowa State University

We study Au, Cr, and Ag metals evaporated on rf-sputtered a-Si:H at room temperature using high-resolution photoemission techniques. For Au/a-Si:H, three regions of coverage can be classified: an unreacted region with an equivalent thickness of 2 Å, followed by an intermixed Au/a-Si overlayer (~ 9 Å), and a dual-phase region at higher coverage. Au adatoms are dispersely distributed in the unreacted region. They subsequently cluster in the intermixed region, where they attach to Si atoms that are not hydrogen-bonded, suggesting that the intermixed Si were mainly those that had dangling bonds. In the dual-phase region, two sets of Au 4*f* core levels evolve with higher binding energy, one from Au intermixed with Si, and the lower one exhibiting pure gold character. The interface eventually ends up with the sequence: a-Si:H(sub.) + (pure Au mixed with intermixed Au/Si) + (vac.). This is unlike the case of Au on c-Si, which has a pure gold layer sandwiched by intermixed Au/Si complexes along the surface normal. Traces of silicon atoms on top of the composite surfaces appear even at the highest coverage, 205 Å, of the gold deposit. The applicability of the four models previously used for the Au/c-Si interface is also briefly discussed.

For Cr/a-Si:H, the evolution of the interface qualitatively follows that on c-Si, despite differences in the valence band emission. The interface begins with an inactive layer (≤ 1 Å) of Cr, followed by an intermixed Cr/a-Si:H layer (≤ 12 Å). With further Cr deposition, bulk-like Cr metal begins to develop on top of these. Some features exhibited by the Cr/a-Si:H interface are specific to a-Si:H surfaces. For instance, Cr adatoms are found around the dangling bond neighborhoods at coverages below 1 Å, avoiding Si–H bonds. The oxygen residue is responsible for the presence of a 6 eV peak in the valence band as well as a chemical shift in the Si 2*p* core levels. However, it is the intermixed Cr/a-Si:H species occurring above 2 Å of Cr deposition that provokes the presence of these structures, even though at low coverages, the oxygen residue does not show any effect on the surface-electronic structure of the a-Si:H film. At high coverage, a slight trace of silicon atoms is still detectable.

The Ag and a-Si:H interface is abrupt without intermixing. However, a subtle change occurs at a coverage of 1 Å. Below that, silver atoms are likely to distribute at regions that are Si-H-bond free. Further, bands at the surface bend upward, similar to the Au/c-Si:H interface. Above 1 Å, no Si-H bonding states are found either in the valence-band or the core-level spectra.

1

INTRODUCTION

Comprehending completely the metal-silicon interface is a challenge, not only for academic reasons but for improved industrial application. The complexity of interfaces is related to the fact that reactions occur mostly at temperatures well below the temperature required to form silicides. Moreover, the interfacial phenomena are strongly dependent on characteristics of the electronic properties of metal deposits. No models can then uniquely describe the interface reaction [1]. For example, the interaction with Si is weak for the noble metals whose *d*-shell is closed. However, despite the fact that Au and Ag do not form stable silicides, Au intermixes severely with Si, whereas Ag/Si is an abrupt interface. For other metals like Cr with an unfilled *d*-band, various forms of silicides are possible, from a metal-rich silicide (Cr_3Si) to a Si-rich silicide ($CrSi_3$).

To date numerous studies have been done particularly for metals on single-crystal silicon (c-Si) as a substrate. However, information on metals on amorphous substrates is limited. In this dissertation, metals deposited on a hydrogenated amorphous silicon (a-Si:H) film at room temperature are studied. The purpose of this work is mainly understanding the electronic properties of the interface, using high-resolution synchrotron radiation photoemission techniques as a probe. The results can also serve as a complement to the study of the crystalline interface. Amorphous material like a-Si:H is particularly interesting because of its wide application in the solar-cell industry. Atomic hydrogen plays an important role in passivating dangling bonds of a-Si:H films, thus reducing the gap-state distribution. In

addition, singly bonded hydrogen also reduces states at the top of the valence band which are now replaced by deeper Si-H bonding states.

The interface is formed by evaporating metal on an a-Si:H film in successive accumulations at room temperature. Au, Ag, and Cr were chosen as the deposited metals. Because of the effect of increased recombination centers in doped a-Si:H, undoped films are used as substrates. Since some unique features can be found in a-Si:H, such as surface enrichment of hydrogen diffused from the bulk and instability of the free surface, we do not expect the metal/a-Si:H interface to behave exactly as its crystalline counterpart. For instance, for some thicknesses of Au on top of c-Si, a pure gold layer is found to be between the intermixed Au/Si at the substrate and the vacuum sides. Our study of Au/a-Si:H, however, does not find such a layer. More interestingly, metal deposits, at low coverages, are found to gather preferentially around regions deficient in hydrogen. As the thickness is increased, some Si atoms in those regions are likely to leave their sites to intermix with metal overlayers like Au and Cr.

PHOTOIONIZATION PROCESS

Photoemission spectroscopy (PES) has become one of the most powerful techniques for probing the electronic structure of condensed matter. Spectra in PES can give detailed information, for example, the band structure of a crystal, the lifetimes of electrons and holes in solids, valence energy levels of deposits coupling to the substrate, screening response due to electron relaxation. Photoemission is in principle a simple process. A photon of well-defined energy penetrates a sample, and is absorbed by an electron, thereby resulting in the emission of a photoejected electron, the photoelectron. The monoenergetic photon can be produced by an intense gas-discharge line source or by synchrotron radiation. Features in PES spectra can originate from electronic transitions from the bulk of the solid, as well as from transitions involving electronic states at the surfaces.

A Simple Picture

The principle of the photoionization process is shown schematically in Fig. 1. For a solid, the fundamental equation governing the process is

$$E_k = (h\nu - \phi) - E_b \,, \tag{1}$$

where E_k is the kinetic energy of the photoejected electron measured from the vacuum level, ν is the frequency of the incident photon, ϕ is the work function, E_b is the binding energy, referred to the Fermi level E_F, of the electron which is ejected. The parentheses of Eq. (1) emphasizes the necessary condition of the primary photon current supplying the energy at least sufficient to

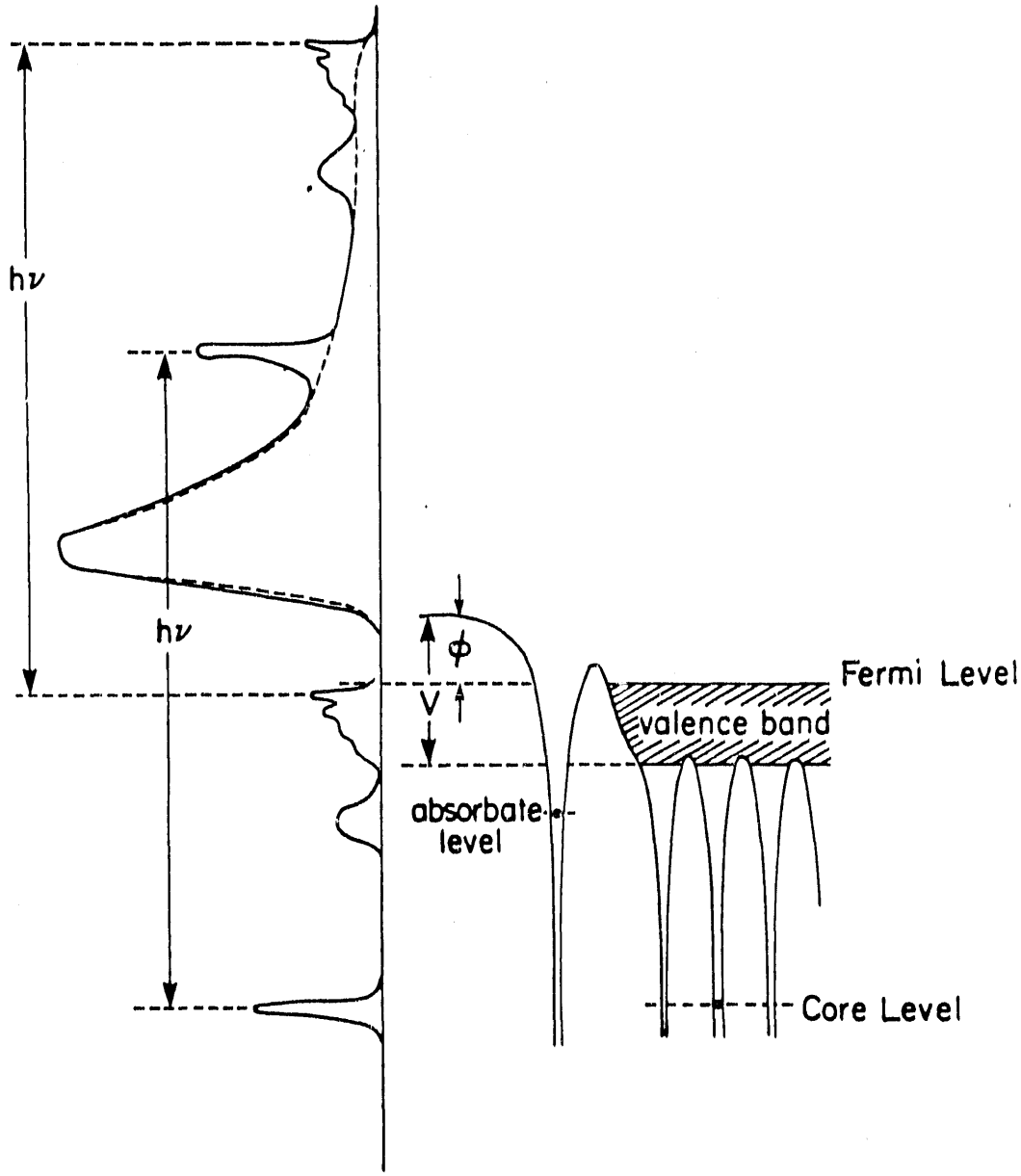

Fig. 1: Schematic of valence band, core levels, an absorbate level, the work function Φ and the inner potential V of a metal. The dashed line of the photoemission spectrum indicates the background distribution from inelastically scattered photoelectron

overcome the work function barrier. It is the photoejected electrons, not the photons, that are collected and analyzed. Each character in Eq. (1) is conventionally signed as a positive number. However, the binding energy of a level in physical sense is a negative value.

The work function is commonly defined as the energy difference between the Fermi level and the vacuum level. For a semiconductor the work function is defined similarly but is a variable because of doping. However, one must understand that work function is a statistical concept and represents a volume contribution due to the periodic potential of the crystal lattice and a surface contribution due to the possible existence of a dipole layer at the surface. The effect of the surface dipole layer is small for metals of low electron density, but can be a few eV for metals of high electron density. Thus the work function is different for different single faces for a given crystal. Further, addition of the sample work function to the binding energy does not necessarily yield the binding energy with respect to the vacuum level [2].

Experimentally speaking, an electron energy analyzer is required to measure the energy distribution of the photoelectrons. As shown in Fig. 2, the sample has to be put in electrical contact with the energy analyzer, establishing the sample contact potential, δ, which is the work function difference, by charge flow and equalizing both Fermi levels. The work function of the analyzer shown is smaller than that of the sample and therefore charge will flow to the sample. From Fig. 2, the photoelectron left the sample and escaped to vacuum with a kinetic energy E_k'. As the photoelectron travels to the analyzer slits, it is accelerated by the sample contact potential so that it becomes E_k as it enters the analyzer. If,

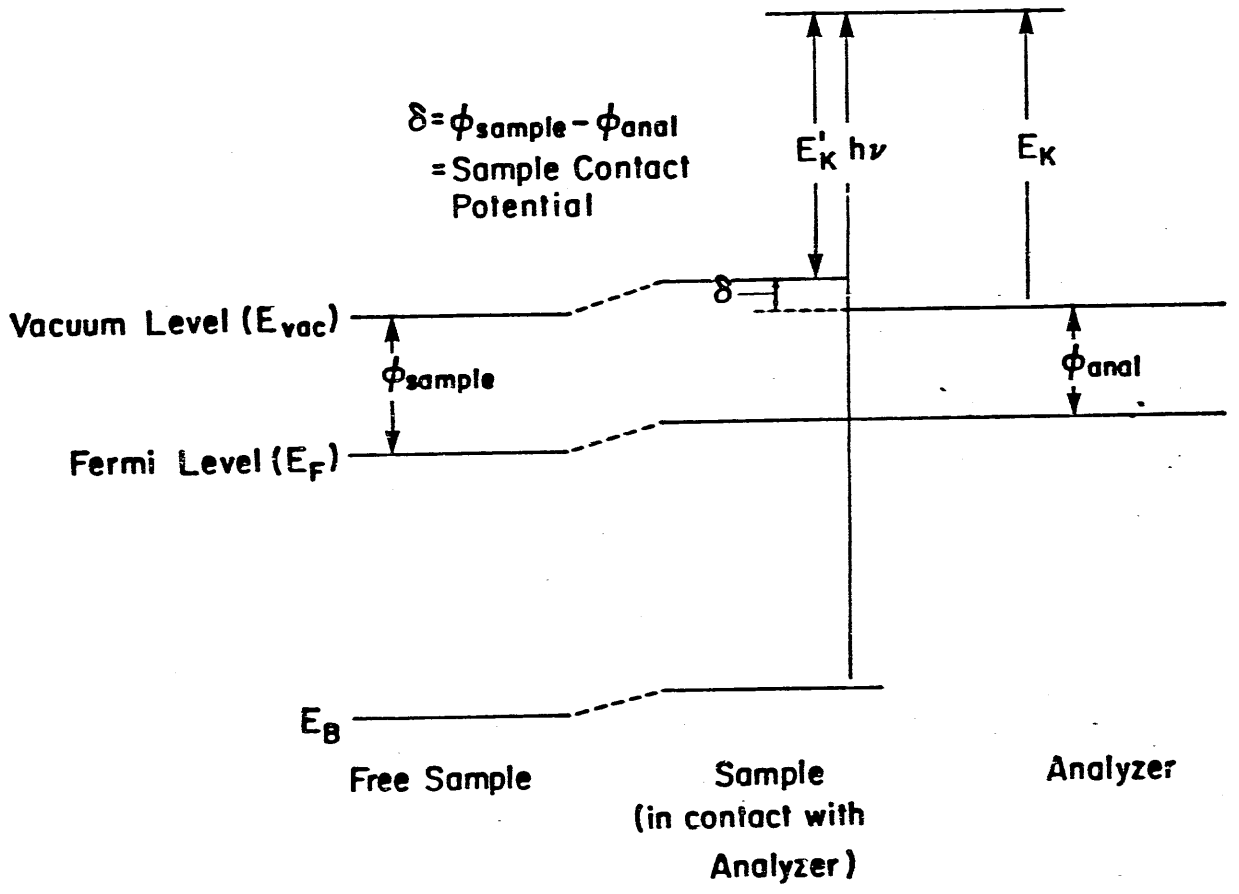

Fig. 2: Schematic of energy level of a metallic sample. At left the sample is free; at center it is in metallic contact with a photoelectron analyzer and the contact potential δ is established. The photoelectron kinetic energy associated with excitation of a bound level is indicated

conversely, the work function of the analyzer is larger than that of the sample, the photoelectron is retarded. In either case, the kinetic energy of the photoelectron appears in the analyzer with the same E_k for a given hν, no matter what the work function of the sample from its Fermi level. Therefore, the actual work-function barrier seen by an excited photoelectron is the work function of the analyzer. Thus, ϕ in Eq. (1) means empirically the work function of the analyzer.

Koopmans' Theorem and Adiabatic Relaxation

With a fixed hν, the measured PES spectra are commonly called energy distribution curves (EDCs). To extract the occupied electronic density of states (DOS), the measured EDCs should be shifted down in energy by an amount ($h\nu - \phi$), as shown in Fig. 1. Ignoring the question of the relationship between peak amplitudes or areas in EDCs and a particular DOS, we can determine the energy of a photoelectron by applying Eq. (1). However, the underlying assumption of Eq. (1) is that if an electron is removed from a system containing N electrons then the energies and the wavefunctions associated with all orbitals in the remaining N–1 electrons are unchanged. In other words, the N–1 electron orbitals are frozen in their original distribution without being allowed to relax. The result is known as Koopmans' theorem [3], which is often referred to as an one-electron or a first-order approximation. Obviously, the final state in this situation is not an eigenstate of the system with the photohole. Nevertheless, the one-electron model has been shown adequate to describe spatially extended electron states. The Koopman energies of these extended states have been

proven approximately the same as the negative of the Hartree-Fock eigenvalue.

However, the one-electron model starts to break down for localized core levels, where the Koopmans' energy is never observed. In reality, the N–1 electrons may relax lowering the energy of the ionized final state. When a photoelectron-photohole pair is created, it forms an electric dipole. For small separations, the surrounding electrons respond to the dipole field and an effective dipole moment is then set up. This can also be viewed as collective screening of the external field of the dipole. As the separation of the photoelectron-photohole pair increases the surrounding electrons start to notice the individual charges of the photohole and the photoelectron and respond in order to screen out those charges by gathering around the photohole and by avoiding the photoelectron. Therefore, the relaxation is the result of a flow of surrounding negative charge towards the photohole in order to screen the suddenly appearing positive charge. The screening lowers the energy of the hole state left behind and therefore makes more energy available to the outgoing photoelectron.

The origin of relaxation may be intra- or extra-atomic. If we take both relaxation channels into account then Eq. (1) is rewritten as

$$E_k = (h\nu - \phi) - E_b + E_a + E_r , \qquad (2)$$

where E_a and E_r are intra- and extra-atomic relaxation shifts, respectively. The relationship of E_a or E_r to the atom or solid is symbolically depicted in Fig. 3. E_a is constant for the core electrons of a given atom. The additional E_r, which is zero for a free atom, in solids is based on the fact that the

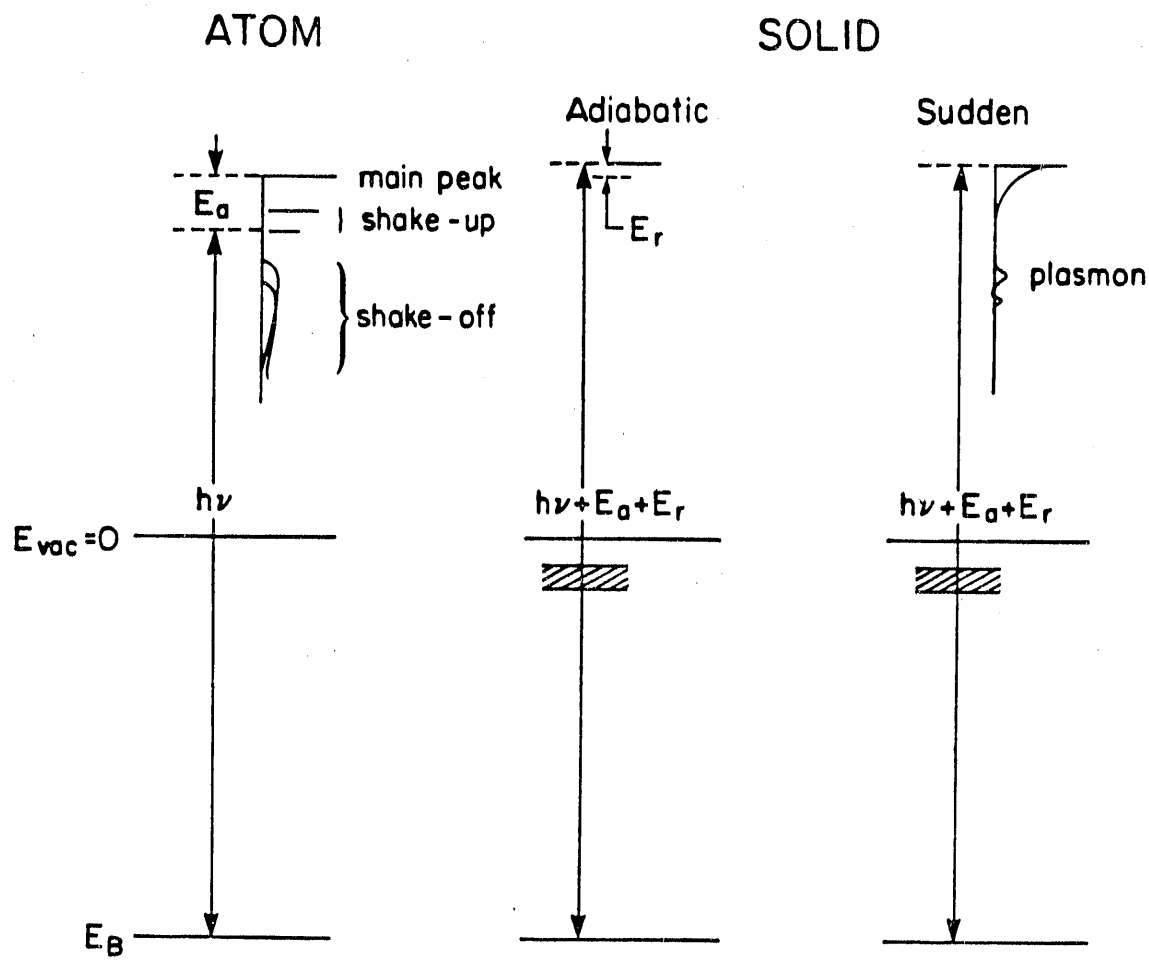

Fig. 3: Schematic photoemission spectra for a core level emission in the sudden approximation. Left: atomic photoionization showing the main peak, shake-up and shake-off satellites. E_a is an intra-atomic relaxation energy shift. Spectra for the same species in a solid for the adiabatic (center) and the sudden limit (right). E_r is an additional interatomic relaxation energy shift

formation of the valence band or hybridized bonds increases channels for the system to relax interatomically. E_r is particularly large in metals where the delocalized valence electrons can easily polarize and screen the core hole efficiently. The magnitudes of E_a and E_r are only a few eV or less. From Eq. (2), the ejected photoelectron gains energy from the additional extra-atomic relaxation and shifts to higher kinetic energy. Evidently, the binding energy is higher for an atom in its atomic state than in a solid state.

If the surrounding electrons relax around the photohole without excitation to the new environment, then the photoionization process is adiabatic. In other words, the ionized final state is always the ground state of the N–1 electron system. The limit of the adiabatic approximation is set in the photoionization threshold region where the photoelectron kinetic energy approaches zero such that it spends more time and possibly dies off in the vicinity of the photohole. In this case the surrounding electrons see no net charge because of the charge cancellation at the source atom. However, the adiabatic approximation is hardly fulfilled as the excitation energy is far above the threshold. Another approximation called *sudden* approximation described below is then more suitable to describe the photoionization process.

Scattering

The photoionization process involves creation of a photoelectron-photohole pair due to the coupling of the photon field with the solid. In the independent-particle approximation, the photoelectrons and photoholes are regarded as well defined excitations of the system and considered to be independent of each other. These excitations will interact with the rest of the electrons in the solid in their characteristic way. For example, the decay of

photohole is via the Auger mechanism in which further electron-hole pairs are created. The photoelectron, on the other hand, can undergo various scattering processes, e.g., electron-electron, electron-phonon and electron-impurity scattering. These scattering processes limit the lifetimes of photoelectron and photohole states, resulting in broadened structure in the photoelectron EDCs. For the *photohole*, lifetime broadening is directly affected by the uncertainty principle. For the *photoelectron*, however, coupling of the final state to the initial state for direct transitions broadens it further due to the uncertainty of the final-state momentum. Uncertainty in final state momentum is $\pm\Sigma_2(\partial k/\partial E)$, where Σ_2 is the imaginary part of the self-energy, or the inverse lifetime, and $k_\perp$ is the perpendicular momentum.

A photoelectron passing through a solid scatters within the solid, thereby suffering energy loss. The electron may be scattered by phonons, a vibrational response of the host lattice. The energy lost in this scattering event is small, typically a few meV, and the experimental resolution is usually not sufficient for phonon scattering to be of importance. However, phonons can broaden the core level lines.

The most important energy loss for an excited electron is via electron-electron scattering events. There are of two major types. The first major loss is that the excited electron may transfer some of its energy to a bound electron, thus creating another excited electron and also a hole in the bound state. The amount of energy transferred to create an electron-hole pair can be arbitrary for a metal, but has to exceed the band gap in a non-metal. If an excited electron is scattered many times, it may not have enough energy to be able to escape at all and finally it falls back to the occupied band. Or it may

eventually escape from the solid as a low energy secondary electron resulting a high background shown near the work function cut-off in Fig. 1.

Another solid state form of characteristic energy loss is the possibility of creating bulk or surface plasmons during the photoemission process or during escape. Plasmons are oscillations of charge density. After a plasmon loss, photoelectrons emerge with reduced kinetic energy and appear in the spectrum as a broad peak at energies lower than the adiabatic peak by amounts which are integral multiples of the plasmon energy (~ 10 to 15 eV) [4], as shown in Fig. 3. Its shape and intensity depend essentially on the material through which the electron is passing and not on which orbital underwent photoionization.

The concept of mean free path [5] is thus generated by the scattering events. If the probability of inelastic scattering is small as a result of insufficient energy of the excited electrons to create electron-hole pairs or to generate plasmons, then the mean free path is large. On the other hand, for electron energies above the plasmon excitation threshold the mean free path is extremely small, less than 10 Å or a few atomic layers. Figure 4 shows the dependence of the measured escape depth as a function of kinetic energy for a number of solids. The escape depth is relatively large at high and low energies but is very small at intermediate energies. Thus electrons with energies in the range of typically 20 to 200 eV originate from a depth of less than 10 Å and therefore carry with them information relating to the surface region.

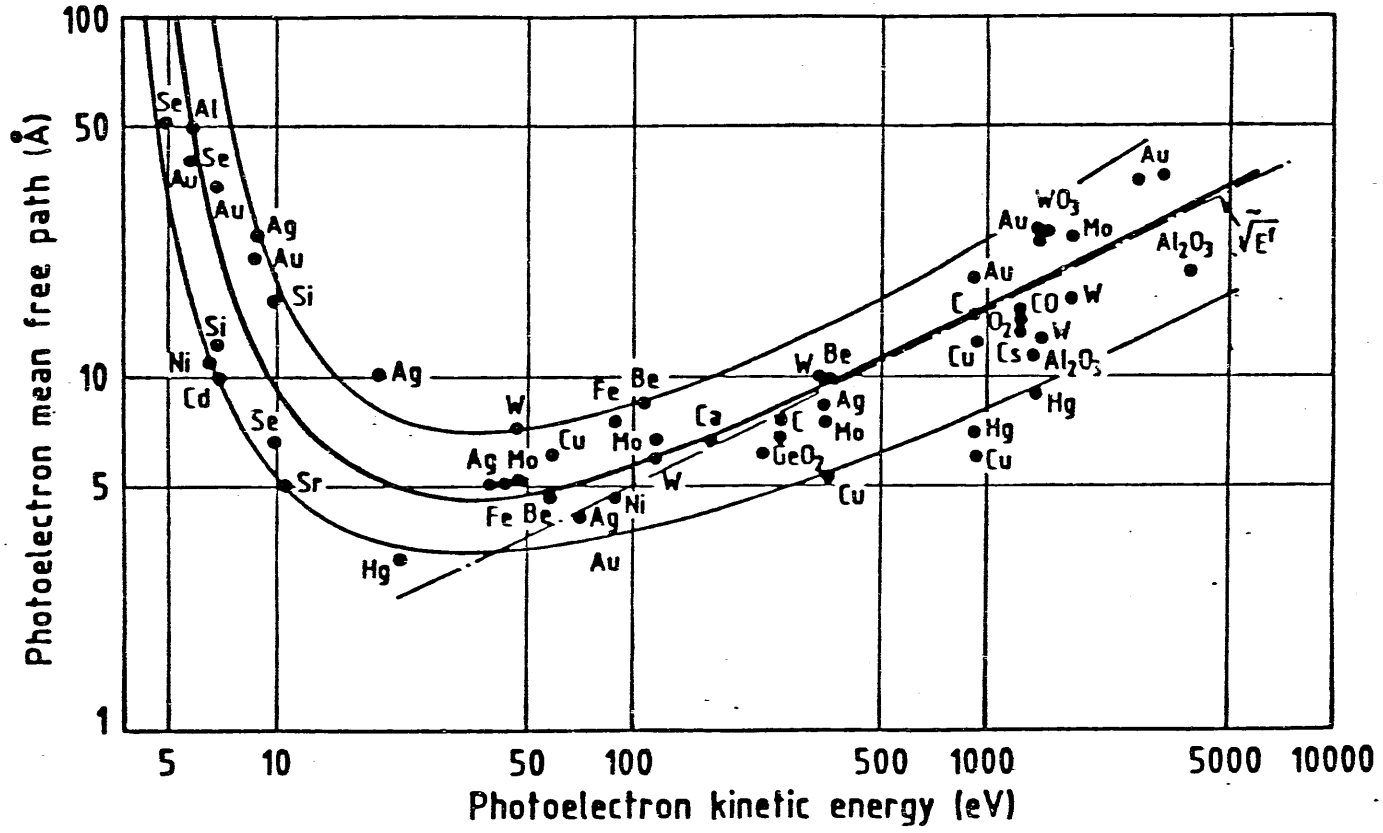

Fig. 4: Mean free path (Å) versus electron kinetic energy (eV). A short mean free path is found at kinetic energies between 20 and 200 eV. (From C. R. Brundle, Surf. Sci. 48, 99 (1975))

Screening in the Sudden Approximation

The adiabatic description of the relaxation shift from the Koopmans' energy is adequate if the photon interaction is slow and the ion is left in its ground state at all times. This condition can be achieved if the photoelectron is excited just above threshold. Then, the excited electron remains near the hole for a longer period of time, and thus the potential which the surrounding electrons respond is switched on slowly. However, with experiments involving kinetic energies far above threshold, a more usual assumption is the sudden approximation. In this approximation, the photoelectron which left the source atom quickly has a large kinetic energy and the hole potential appears to be "switched" on instantly. If the core holes involved are fully screened then the core-level photoelectron spectrum will appear as only a main line broadened, aside from the instrument function, by the core-hole lifetime. However, the final state of the system is indeed perturbed by high-speed outgoing photoelectrons and is not in the electronic ground state. Therefore, additional electronic excitations occur. The energy required for the excitations will reduce the kinetic energy of the outgoing photoelectrons and thus increase the apparent core-level binding energy due to conservation of total energy. Hence the additional excitations will manifest themselves on the larger binding energy side of the main line as satellite structures, as illustrated in Fig. 3. If the excitation of a bound electron is to another bound state, then the satellite structure is called a shake-up satellite. If the excited state is in the unbound continuum, then the structure is called a shake-off satellite. The shake-up satellites often consist of sharp peaks while the shake-off satellite spans a wide continuum. The satellite structure

is dependent on the nature of the orbitals. In solids, satellite structure is observed in the presence of a large general background of secondary electrons. However, for some compounds, like transition metal compounds, the satellite structure is often very intense and easily discernible.

It is generally stated that the actual photoabsorption process occurs nearly instantaneously ($\leq 10^{-17}$ sec). However, screening processes to a *suddenly* created core hole respond on a time scale from 10^{-16} sec to 10^{-12} sec [6]. For instance, localized screening for 15 eV plasmons has a response time of 2.75×10^{-16} sec. On the other hand, the delocalized screening by core-valence-valence Auger transitions takes about 10^{-12} sec [6]. Further, as illustrated by Gadzuk [6], screening processes between these limits can appear as Coster-Kronig transitions, low energy electron-hole pairs, or phonons. Here the Coster-Kronig transition means that one of the two vacancies produced in the radiationless decay is in a different subshell of the same principal shell that contains the initial vacancy [7]. Each screening response has its own field of influence: phonon excitation is most important in ionic solids [8], shake-up is generally but not exclusively associated with insulators, and the electron-hole pairs (a many-body screening response) should occur only in metals and semimetals.

In the framework of the sudden approximation, the shape of the core-level line can faithfully illustrate various screening processes in their own characteristic ways. First, plasmons, created either by the dipole formed by the suddenly created core-hole and the photoelectron or by the photoelectron on its way out to the surface, appear as subsidiary lines on the low kinetic energy side of the main peak. Second, the production of phonons, coming from either the relaxation of the nearby nuclei due to the sudden appearance

of the hole or the photoelectron-phonon scattering on the photoelectron path inside the solid, causes line broadening with essentially Gaussian character [9]. Third, in a metal, the low energy electron-hole pairs result in a long-tailed asymmetric line shape with a power-law character, as shown in Fig. 3.

In a particular case that is dominant in metals, shake-up components can appear as electron-hole (not the photohole) pairs around the Fermi level. This phenomenon can be easily understood from the valence-band and the core-level EDCs of Fig. 5. Valence band emission is shown in the left panel where the upper curve is for Cr metal and the lower curve is for Ag metal, whereas the right panel shows core level emission with the Cr 3*p* core level in the upper curve and the Ag 3*d* level in the lower curve. From the figure, a sharp contrast in the DOS at E_F appears between these two metals. Cr has a higher DOS at E_F than Ag does. This difference affects faithfully the core-level line shape, particularly on the high-binding-energy side. The shape is more asymmetric in Cr than in Ag. This correlation between higher DOS at E_F and greater asymmetric core line can be understood as follows. Upon sudden removal of a core electron in a metal, the conduction electrons tend to screen the positive charge. The wavefunctions of each screening electron are no longer in their original form in the ground state but become modified to a degree that depends on their proximity to the core hole. According to the Anderson theorem [10], the ground state of an infinite electron gas is orthogonal to the same electronic state with a localized core hole produced suddenly. The energy required for the screening process is taken from the kinetic energy of the outgoing photoelectron. The spectrum exhibits a "tail" of lower kinetic energy photoelectrons because the energy which goes into the excitation of electron-hole pairs. The shape of the line reflecting the electron-

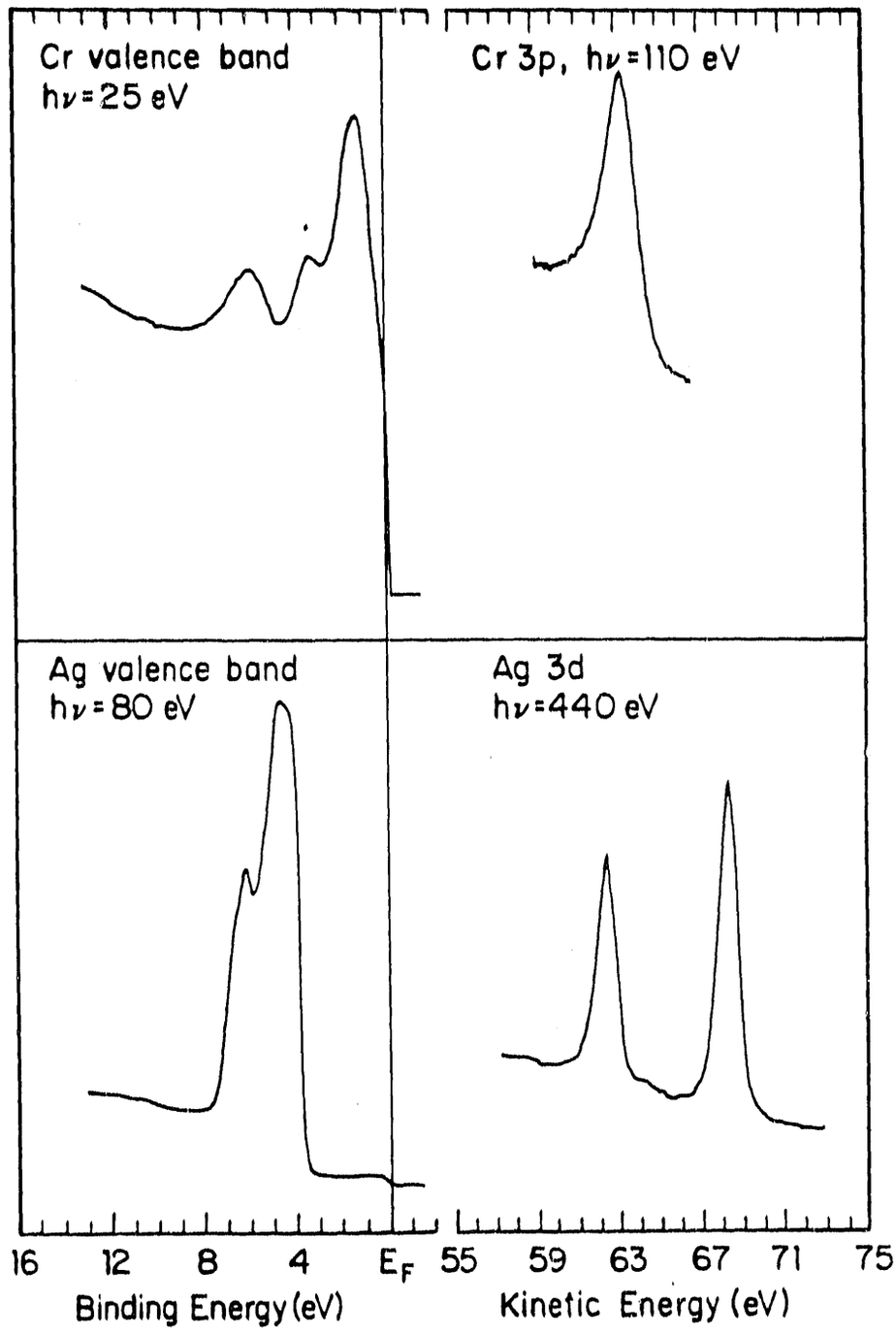

Fig. 5: Valence band and core level photoemission spectra for Cr and Ag. Note the correlation of the density-of-state at E_F and the asymmetry of the line shape of core level

hole pairs excitation is of the form $\omega^{\alpha-1}$ [11], where α, the asymmetry factor, generally lies between 0.0 and 0.5. Since the screening depends on the density of states close to the Fermi energy, the core-level line shapes are likely to be affected by the increased occupation at E_F, giving greater α. The excitations at the Fermi level accompanying the final core-hole state are an intrinsic property of the metal. They, therefore, do not depend either on sample thickness or on incident photon energy. Plasmons, in contrast, do not exist if the sample thickness goes to zero.

In semiconductors and insulators $\alpha = 0$ because the energy band gap eliminates the possibility of exciting low-energy electron-hole pairs.

Another important many-body effect observable especially in the case of metals with incomplete *d*- or *f*-shells is electron-electron correlation [12]. When the core hole is created, a localized empty *d* level at the hole site is pulled down below E_F. When the coupling between the core hole and the incomplete *d*- or *f*-shell states is strong enough, a satellite appears at a larger binding energy than the main peak. The core-level spectrum exhibits mainly two peaks with asymmetric line shapes.

In summary, PES spectra do not give rise to a measurement of the initial ground state property. A photoemission peak reflects an energy difference between the ground state of the sample and the metastable final state of the ionized sample.

Theoretical Models

The photoemission process has been theoretically split off into three independent sequential steps: Optical excitation, transport to the surface, and escape into vacuum. This process is called the "three-step model",

developed by Berglund and Spicer [13]. According to the sequence of three events, the intensity distribution of primary electrons $I(E, h\nu)$ can be factorized:

$$I(E, h\nu) = P(E, h\nu) \times T(E) \times D(E) , \tag{3}$$

where $P(E, h\nu)$ is a distribution of photoexcited electrons by the optical excitation and gives the primary spectrum (zero loss line plus intrinsic plasmons), $T(E)$ is a transmission function characterizing the photoexcited electron transport to the surface, and $D(E)$ is the escape function of the photoexcited electron. A core level spectrum should give a Lorentzian line whereas a valence band spectrum should give a replica of the DOS of the sample.

The distribution of photoexcited electrons $P(E, h\nu)$ is given through the optical excitation of electrons between the occupied valence band Bloch state $|\Psi_i\rangle$ and the empty conduction band Bloch state $|\Psi_f\rangle$ of the excited electron:

$$P(E, h\nu) \alpha \sum_{i,f} \int d^3k \left\langle \Psi_f \middle| H' \middle| \Psi_i \right\rangle^2 \delta(E_f(k) - E_i(k) - h\nu) \, \delta(E - E_f(k)) . \tag{4}$$

The k integration extends over the first Brillouin zone. The first delta function ensures energy and momentum conservation. The second delta function selects the transitions at the specified final state energy determined by electron energy analyzer. Note that the photoemission in this model becomes a very selective process since three δ-functions (including the momentum-conservation in the matrix element) restrict the possible distribution.

The transport function $T(E)$ includes inelastic electron-electron scattering or elementary excitations in the solid. Berglund and Spicer have found in a classical treatment that $T(E)$ can be expressed as $T(E) = \alpha_s\lambda_s/(1 + \alpha_s\lambda_s)$, where α_s is the optical absorption coefficient and λ_s is the inelastic mean free path. If $\alpha_s\lambda_s << 1$, the mean free path is much smaller than the penetration depth of the light, $1/\alpha_s$, then $T(E) \approx \alpha_s\lambda_s$. Thus, in this limit, $T(E)$ is a slowly varying function depending on the energy E of the photoelectrons and reflecting the fact that no single scattering process characterized by one particular sharp threshold energy dominates electron transport.

$D(E)$ is a smooth function of E beyond the threshold for which the energy of the electron E is sufficient to permit it to surmount the potential barrier at the surface. $D(E)$, and $T(E)$, may distort the energy distribution. However, they are not expected to introduce structures or peaks in the intensity distribution $I(E, h\nu)$.

Despite successful application of the three-step model in explaining PES spectra, it has conceptual deficiencies [14, 15]. First of all, it says that the optical excitation taking place at a given point in the solid, then propagation, then transmission of the photoelectron into vacuum are independent processes. It further says that the inelastic electrons lose their energy after they have first been optically excited. As a matter of fact, the process affecting the photohole (or the initial state) and the photoelectron (or the final state) may interfere in certain cases destructively so that the whole photoemission process has to be described as single quantum mechanical event. Secondly, it uses stationary initial- and final-state one-electron wavefunctions to calculate the matrix element. This is certainly not compatible with the fact that the final state is highly excited in

photoemission. Thirdly, the hole in the three-step model is long-lived, which violates the uncertainty principle. Finally, it drops all surface states and surface resonances from consideration by absorbing the whole effect of surfaces into the escape function.

A number of sophisticated theoretical models have been developed to explain photoemission from solids with a many-body formalism [16, 17]. For example, Feibelman and Eastman [18] used steady-state scattering theory to derive a Fermi Golden-Rule formula for a photoelectron current from an independent electron solid. They showed that for sufficiently weak electron damping the Golden-Rule formula devolves into the semiclassical "three-step" formula (4). However, the results of many-body work are very unmanageable and it is hard to compare experimental photoemssion spectra within the context of the different models. Hence, the three-step model can be used as a first approximation for a quantitative description of photoemission spectra.

SYNCHROTRON RADIATION PHOTOEMISSION SPECTROSCOPY

Properties of Synchrotron Radiation

Synchrotron radiation is generated by electrons centripetally accelerated in an orbit produced by a dipole magnetic field. A synchrotron radiation source is characterized by its critical wavelength λ_c expressed as

$$\lambda_c = \frac{4}{3}\pi R \left(\frac{m_0 c^2}{\varepsilon}\right)^3 . \tag{5}$$

Half the power emitted is emitted at wavelengths shorter than λ_c. R is the radius of curvature of the orbit. At low speeds the electrons emit a Larmor pattern in a frame of reference moving with the electron shown in Fig. 6a. But as the electron's speed approaches that of light, this pattern appears in the laboratory frame as a narrow cone with strongest emission in the forward direction of the velocity (Fig. 6b). The angular extent in the plane of the orbit has a characteristic half angle $\psi = m_0 c^2 / \varepsilon \approx$ a milliradian, where m_0 is the mass of electron, c is the speed of light, and ε is the energy of the electron. Thus, for an observer looking tangentially to the circular orbit, the electrons appear as a bright white point and accelerate in a perpendicular direction. Because of the narrow cone of emission, the bright point is very different than that from other point sources.

The properties of synchrotron radiation can be calculated accurately with the theory originally developed by Schwinger [19] in 1949. Since then, a number of review articles [20 - 22] and internal reports for specific machines [20] have been published. The following are some of the properties of synchrotron radiation, which clearly show advantages over conventional

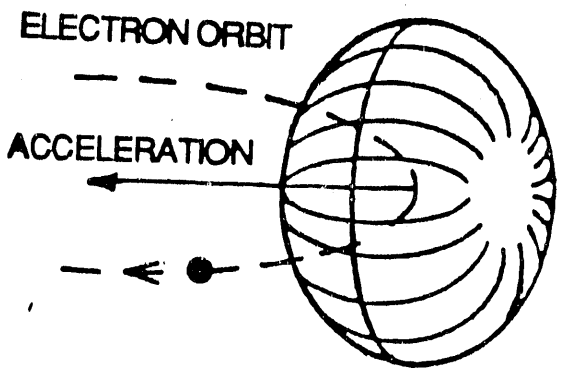

(a)

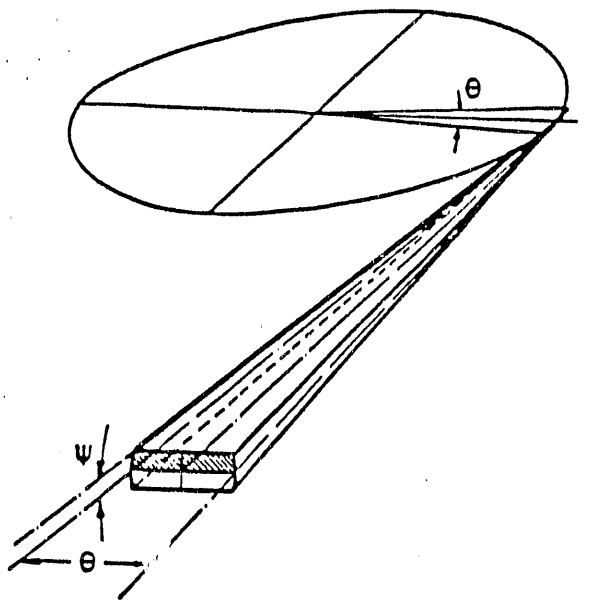

(b)

Fig. 6: Schematic of electron emission at (a) low speed and (b) near the speed of light

line-sources:

1. Synchrotron radiation is an intense spectral continuum up to X-ray wavelengths.
2. Synchrotron radiation is highly collimated radiation, confined in a small elevation angle near the electron orbital plane.
3. Synchrotron radiation has a high degree of polarization. It is completely linear polarized with $\vec{E}$ vector in the orbital plane.
4. Synchrotron radiation is pulsed with fast (nanosecond) time structure.
5. Synchrotron radiation source is an ultra-high vacuum light source, an empirical condition necessary for surface studies.

Although the spectrum of synchrotron radiation consists of many harmonics of the fundamental orbit frequency, these separate components are very close together and indistinguishable. Hence, synchrotron radiation must be used in conjunction with a monochromator to obtain a well-defined photon energy. Monochromators are distinguished by the way the radiation is incident on the concave grating. In the normal incidence region, reflections at the optical components take place at normal, or near normal, incidence. Photon energies at this region can extend up to 40 eV. To reach higher photon energies the radiation must be incident on optical components at angles near to grazing. In a Seya/ERG monochromator [23] for the present study, for example, photon energies between 5 eV and 40 eV are monochromatized by the Seya-Namioka monochromator [24] where the entrance and exit slits subtend an angle of 70°32' at the grating to obtain a good focus condition. Energies above 40 eV are given by the extended range grasshopper monochromator (ERG) [25] where the incidence angle is at 2°

from grazing (or 88° with respect to the surface normal.)

Photoionization Cross Section and Cooper Minimum

The photoionization cross sections (σ or $d\sigma/d\Omega$) are determined by a matrix element of the form $\langle\Psi_f | H' | \Psi_i\rangle$, where H' is the interaction Hamiltonian between the electron and the photon field and $|\Psi_f\rangle$ and $|\Psi_i\rangle$ are the final and initial state. To obtain H', the electron momentum operator $\vec{P}$ in the original Hamiltonian is replaced by $\vec{P} + \frac{1}{2c}\vec{A}$, where $\vec{A}$ is the vector potential of the photon field. Following a proper choice of scalar potential gauge $\Phi = 0$ and neglecting the relatively small diamagnetic term $|\vec{A}|^2$ after expanding the Hamiltonian, H' has then a form proportional to

$$H' \propto (\vec{P}\cdot\vec{A} + \vec{A}\cdot\vec{P}), \tag{6a}$$

or

$$H' \propto (2\vec{A}\cdot\vec{P} - i\nabla\cdot\vec{A}), \tag{6b}$$

The last step has used the commutator $[\vec{P}, \vec{A}] = -i\nabla\cdot\vec{A}$. Various approximations can simplify H' further [26]. First, if the photon field $\vec{A}$ can be expressed as a transverse wave with amplitude $\vec{A}$ and momentum $\vec{q}$, $\vec{A} = \vec{A}_0\exp(i\vec{q}\cdot\vec{r})$, then $\vec{A}_0\cdot\vec{q} = 0$. Second, in the dipole approximation, $\exp(i\vec{q}\cdot\vec{r}) \cong 1 + i\vec{q}\cdot\vec{r} \cong 1$. For photon energies below several keV, q is small enough so that $\vec{q}\cdot\vec{r}$ is small compared to unity for values of r for which the initial state atomic wavefunction has appreciable amplitude. In addition the contributions of the electric quadrupole and magnetic dipole terms are rather small (10^{-4} of the total cross section). Third, if the photon frequency greatly

exceeds the plasmon frequency of the solid then $\nabla \cdot \vec{A} \cong 0$ [27]. Therefore, $\vec{A}$ can be treated as a constant $\vec{A}_0$ by these approximations. Cross sections can then be simply determined, apart from the constant factor, by evaluating the matrix element of the form $\langle \Psi_f | \vec{P} | \Psi_i \rangle$ or $\langle \Psi_f | \vec{r} | \Psi_i \rangle$ or $\langle \Psi_f | \nabla V | \Psi_i \rangle$, where V is the potential in the unperturbed Hamiltonian [28].

If the initial state $|\Psi_i\rangle$ is described by a one-electron wavefunction with quantum numbers, n, l, m of the form $R_{nl}(r)Y_{lm}(\theta, \varphi)$, and the final state $|\Psi_f\rangle$ is written in a similar form (but with no value of n, being in the continuum) as $R_{l'}(r)Y_{l'm'}(\theta, \varphi)$, then the evaluation of the angular integrals in the matrix elements leads to the selection rules

$$l' = l \pm 1$$
$$m' = m, m \pm 1 . \qquad (7)$$

Thus, for any particular l value of the initial state, the final state will contain a coherent sum of two angular momentum states of values $l - 1$ and $l + 1$. In an isolated atom, the bound electron levels are discrete and their wavefunctions are well defined. When atoms are brought to form a solid, the deep-core levels are not significantly changed. However, the outer-shell electron levels are perturbed and form bands with some admixing of atomic wavefunctions. For these band electrons in solids, new selection rules specific to the solid state are required. Apparently, the cross section for these band states will be different due to the changed final state wavefunctions.

If a central potential model, as well as the dipole approximation, is used then the total nl subshell photoionization cross section can be obtained by integrating over the complete 4π solid angle and is given by [29]

$$\sigma_{nl}(E_k) = \int \frac{d\sigma}{d\Omega} d\Omega$$

$$= \frac{4}{3}\pi^2 \alpha_0 a_0^2 N_{nl} h\nu \left(\frac{l}{2l+1} R_{l-1}^2(E_k) + \frac{l+1}{2l+1} R_{l+1}^2(E_k) \right), \quad (8)$$

where σ_{nl} is in cm , $\alpha_0 = 1/137$ is the fine-structure constant, a_0 is the Bohr radius (= 0.52918 Å), N_{nl} is the number of electrons in the nl subshell (= $2(2l+1)$ if filled), E_k is the photoelectron kinetic energy in Rydbergs (1 Ry = 13.605 eV), and hν is the energy of an incident photon. The main contribution to the cross section can be easily realized by the weighting of $R_{nl}(E_k)$ given by

$$R_{l\pm1}(E_k) = \int_0^\infty P_{nl}(r)\, r\, P_{E_k, nl\pm1}(r)\, dr , \quad (9)$$

where $R_{nl} \equiv P_{nl}(r)/r$ and $R_{E_k, l\pm1} \equiv P_{E_k, l\pm1}(r)/r$ is the radial part of the one-electron wavefunctions expressed in Bohr radii of the discrete initial and continuum final states, respectively. For a photon energy well above threshold, transitions to $l' = l + 1$ are more probable than to $l - 1$ [27, 28].

The energy-dependent character of $R_{nl}(E_k)$, which in turn depends on n and l, gives rise to interesting properties. The Ag 4d partial cross section, for example, is given by

$$\sigma_{4d} = 8\pi^2 \alpha_0 a_0 h\nu R_f^2 . \quad (10)$$

For hν well above the 4d threshold $R_f >> R_p$ [29] and therefore the energy dependence of the σ_{4d} is almost entirely determined by R_f. To determine R_f

the final state wavefunction at a photon energy well above the 4*d* threshold is usually assumed to be free-electron like. However, this assumption is challenged by the illustration of Fig. 7, which shows electron emission taken at hν = 35 to 70 eV. The dramatic change in the line shape of the 4*d* band precludes the simple description of the free-electron final states. In addition, in the valence band, there are contributions of electrons with different angular momentum, giving a valence band photoelectron spectrum containing contributions which are weighted by these different cross sections. Hence, the consideration of the wavefunction forms for the initial and final states should be made when evaluating the matrix element.

Second, as seen in Fig. 7, the Ag 4*d* band exhibits an intensity variation with photon energy, which reveals the importance of the cross section effect. To emphasize this point, Fig. 8 shows the work of Yeh and Lindau [30], where the calculated cross section of atomic orbitals *vs* photon energy for selected elements is shown. In Fig. 8, the cross section of *d* band orbitals is three orders of magnitude greater than that of *sp* band orbitals at low photon energy. In other words, *sp* band emission will be severely concealed by *d* band emission. At photon energies above 100 eV, however, a significant reduction of cross section of *d* band orbitals is noticed.

In particular, a dip is shown at about 130 eV in the Ag 4*d* orbital photoexcitation cross section. This dip is called the Cooper minimum (CM) [31]. The atomic nature of the CM effect originates from the presence of a node in the radial part of the initial-state wavefunction and the subsequent cancellation of the dipole matrix element for electron transitions to particular final states. For 3*d* orbitals where no nodes exist, there is no CM. Therefore, a serious reduction of the transition matrix element can be achieved by

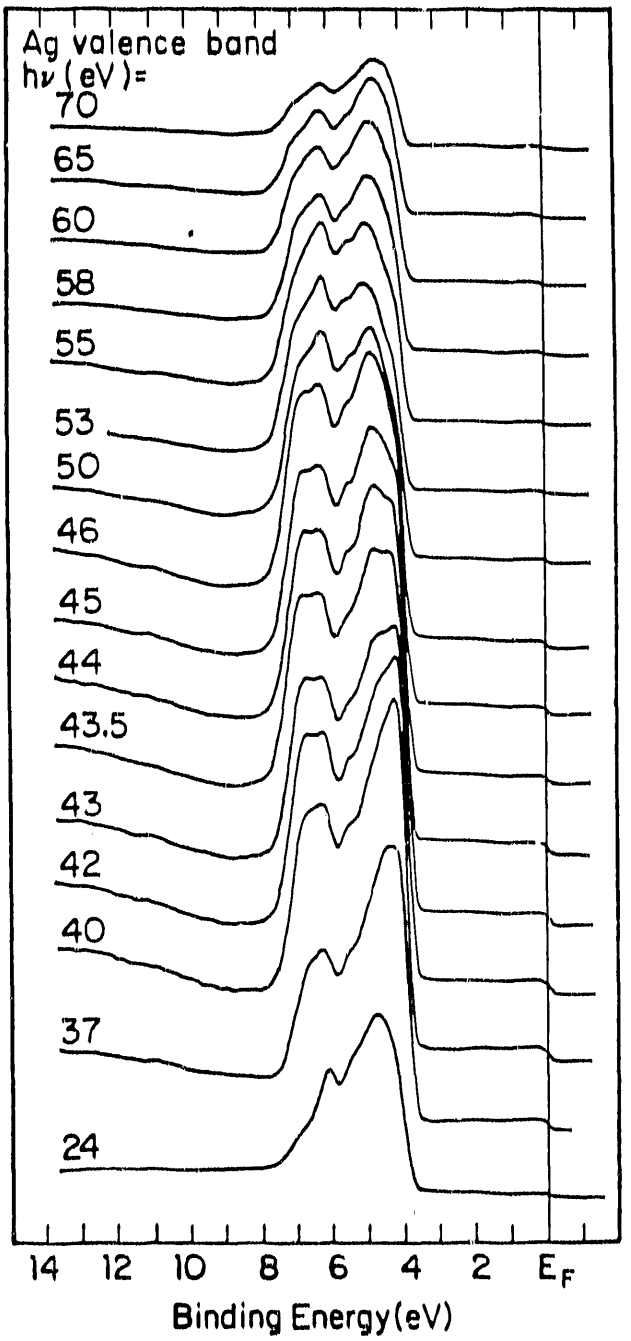

Fig. 7: Valence band photoemission of bulk Ag taken at photon energies of 24 to 70 eV. Spectra are normalized to the same amplitude

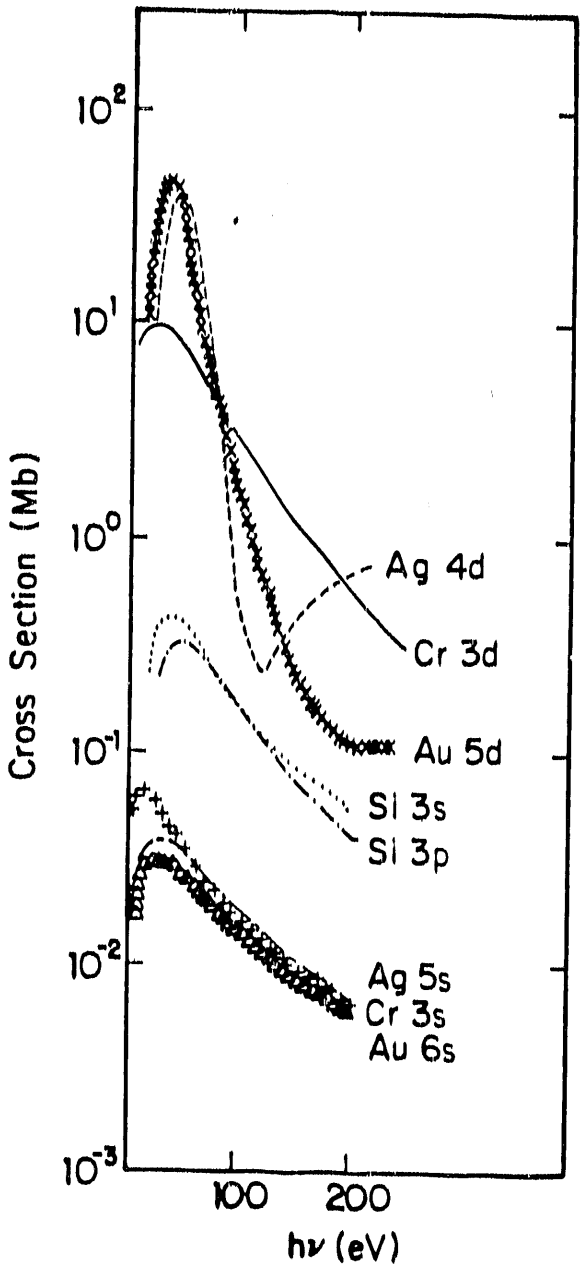

Fig. 8: Photoionization cross section as a function of photon energy for selected materials. The dip of the Ag 4*d* orbital at about 130 eV is the Cooper minimum. Data were excerpted from Ref. 31

properly choosing the photon energy. This property is especially useful to the present study of the noble metals on a-Si:H. At photon energies below 100 eV the cross section effect makes a differentiation of the valence band emission of the a-Si:H substrate from the Au or Ag overlayer difficult. By using a photon energy at the Cooper minimum the difficulty is removed because of the reduced magnitude of the *d*-orbital cross section.

Synchrotron Radiation Photoemission

The ability to vary photon energy lures users to run experiments preferably with synchrotron radiation over laboratory line sources. With this unique option, SRPES can give information in its characteristic ways. First, the escape depth for a given valence or core level can be manipulated by properly choosing the photon energy. Take the silicon 2*p* core level as an example. A photon of energy 160 eV ejects an electron from the Si 2*p* core level with E_b = 100 eV with a kinetic energy of about 55 eV (see Eq. (1)). As Fig. 4 shows, the escape depth at E_k = 55 eV for Si is about 5 Å, thereby enhancing surface emission. On the other hand, if the electron is excited by 110 eV photons, giving E_k of about 5 eV, then the escape depth goes to about 25 Å, giving more bulk-like information. Furthermore, the resolution is better than XPS can achieve.

The continous nature of synchrotron radiation provides three variables, hν, E_k, and E_b. With fixed E_k and E_b, the spectroscopies are called constant final state spectroscopy (CFS) and constant initial state spectroscopy (CIS), respectively. In CFS, also termed as partial yield spectroscopy, the photoemission yield within some energy interval above threshold is measured as hν is varied [32 - 34]. Typically, the intensity of secondary

electrons only a few eV above threshold is monitored in order to avoid hν-dependent contributions. After the primary photoabsorption, decay of the excited core hole occurs largely via Auger emission for low energy (< 1000 eV) core holes. Thus an optical transition takes place from the core hole to an unoccupied state, the core hole recombining with a valence electron with the emission of a second valence electron. Since the yield of secondary electrons is proportional to the total number of core holes created by the photons, the yield spectrum is a direct measure of optical absorption of a specific level in the solid. The resultant spectrum is a measure of the probability of creating a core hole as a function of hν. Note that with a fixed final state, the escape depth is therefore constant.

In CIS, the photoemission yield within some energy interval E to $E + \delta E$ at a fixed initial state energy, $E_b = E - h\nu$ is measured [35]. In this technique, the optical monochromator and electron energy analyzer are scanned synchronously so that $E - h\nu$ is kept constant. The resultant spectrum reflects the number of photoejected electrons as a function of their kinetic energy. In the CIS mode, it is possible to monitor the cross section of a particular initial state as a function of hν.

Resonant photoemission, which gives rise to a better understanding of the electronic structure of solids [36], can be studied by synchrotron radiation. Equation (1) does not necessarily mean a shell electron has to be ejected above the vacuum level (out of the sample). As shown in Fig. 9, an incident energy can excite an core electron to just above the Fermi level and in this case an additional decay channel is created. To illustrate this point clearly, take the first row transition metal as an example (rare earth metals can be discussed in a similar way). In a simplified single-electron picture, a photon with

energy at the 3*p* threshold can excite a 3*p* core electron to above the Fermi level and consequently the excited electron can decay back to the 3*p* core hole (a direct recombination process) accompanied by an ejection of the valence band electron; that is, the process can be described as

$$3p^6 3d^n + h\nu \rightarrow 3p^5 3d^{n+1} \rightarrow 3p^6 3d^{n-1} + e^-(\varepsilon f)\,, \tag{11}$$

where n is the number of electrons in the *d* orbitals and εf is the continuum final state of the ejected electron. The same final state can also be excited by a direct valence band emission,

$$3p^6 3d^n + h\nu \rightarrow 3p^6 3d^{n-1} + e^-(\varepsilon f)\,. \tag{12}$$

Because paths (11) and (12) involve the same initial state and final state, they can interfere quantum mechanically, thereby enhancing (or diminishing) the electron emission at the 3*p* threshold. Note that direct emission can be accessed by any energy so long as it is greater than the *d* band binding energy. On resonance, the energy of the excited 3*p* shell is transferred directly to a valence electron which is ejected with substantially higher kinetic energy than the Auger process would provide. Therefore, operationally, the autoionized electron always occurs with a kinetic energy greater than the 3*p* binding energy, while the Auger electron always occurs with a kinetic energy less than the 3*p* binding energy.

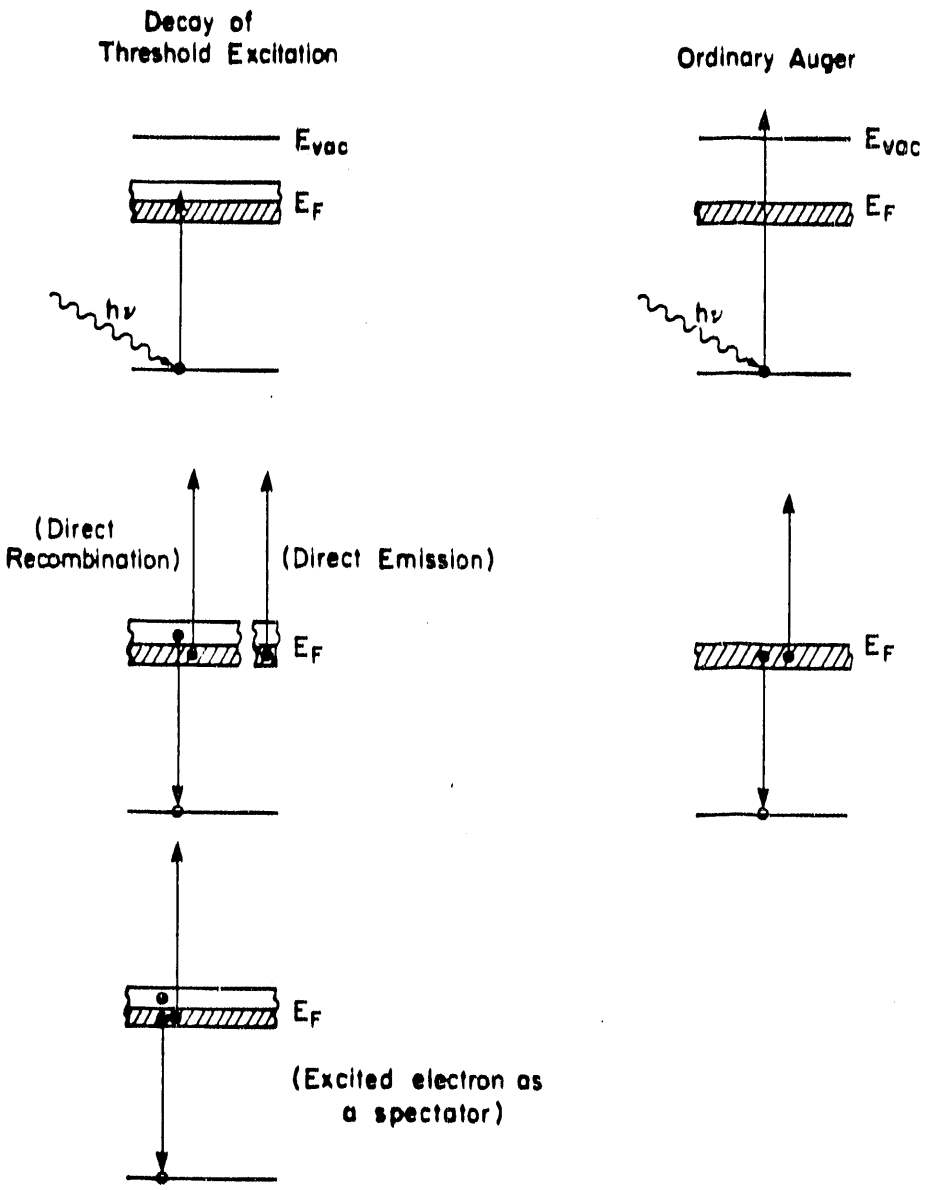

Fig. 9: Comparison of decays of threshold excitation and ordinary Auger. At threshold, the excited electron can be either recombinewith the core hole, or serve as a spectator

METAL - SEMICONDUCTOR INTERFACE

When two metals of different work functions are far apart, the vacuum levels are aligned. As they are brought into contact, the requirement of a unique Fermi level causes charge transfer from the one with the smaller work function to the other. Since there exists approximately one free or unbound electron for each atom in the metal, the charge transfer that takes place upon contact of two metals essentially involves the two outer layers of atoms. An electrostatic dipole layer is formed and the bulk of the metals remains unaffected.

In a semiconductor the situation is rather different. Electrons fill states up to the top of the valence band. There is a band gap between the valence band and the largely empty conduction band. In an n-type semiconductor donor impurity atoms give rise to a small number of electrons in the conduction band. When a metal of higher work function and an n-type semiconductor are brought into contact (a Schottky contact) [37], for example, electrons from the conduction band of the semiconductor flow into the metal till the Fermi levels on the two sides coincide, as shown in Fig. 10. Since the Fermi energy in thermal equilibrium is constant throughout the region and the separation of the conduction band edge E_c from E_F increases with decreasing electron concentration, the conduction band edge bends up as shown in Fig. 10. The transfer of conduction band electrons leaves positively ionized charge (space charge) behind so that the semiconductor region near the metal becomes depleted of mobile electrons. Because of the extent of the band-bending region [38], the bulk electronic structure of the semiconductor is affected by the presence of the metal. Thus, a positive charge is established

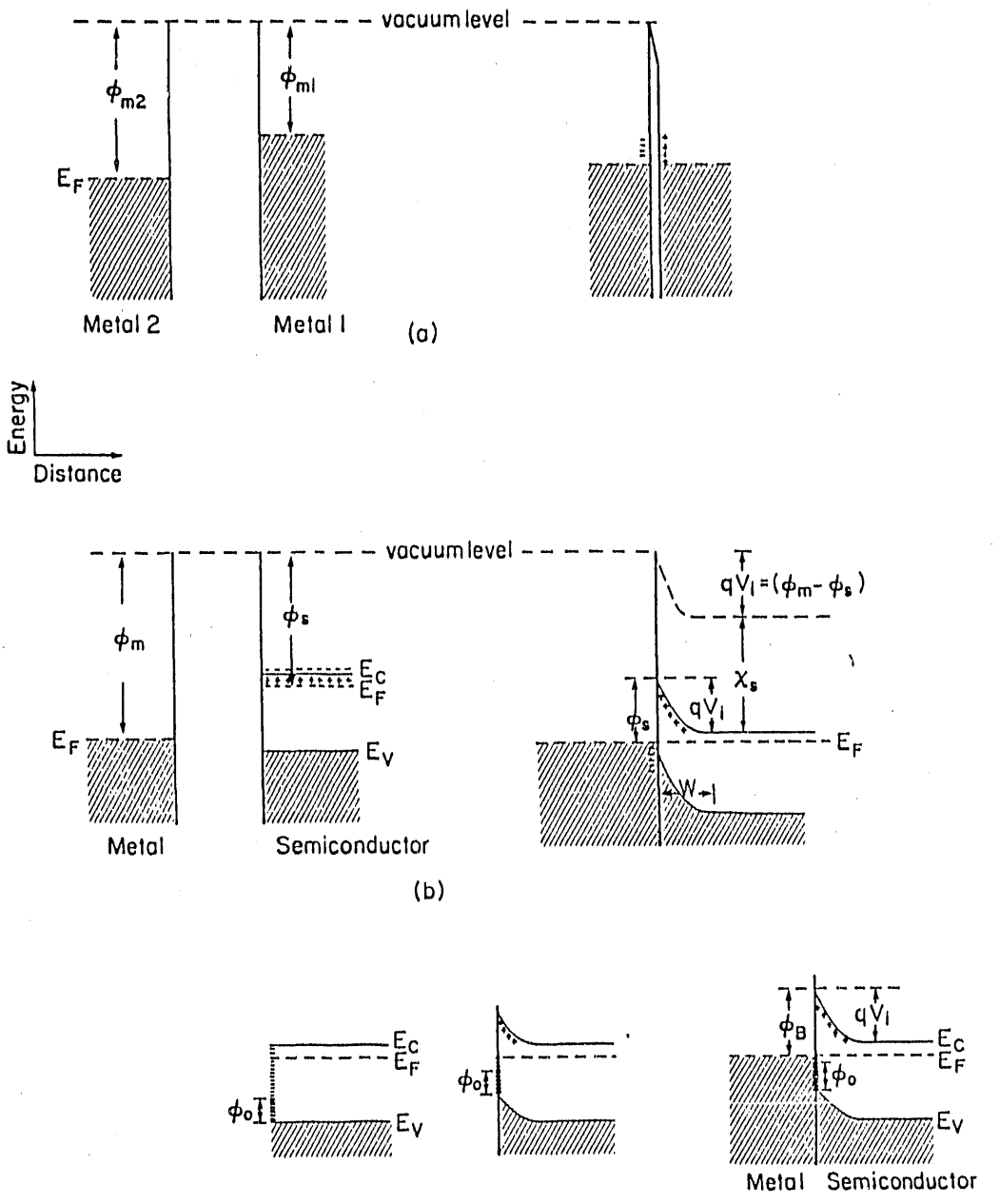

Fig. 10: Metal and semiconductor contact. (a): Two metals with different work functions Φ_m are infinitely separated (left) and in intimate contact (right). (b): An n-type semiconductor and a metal are far apart (left) and in intimate contact (right). Φ_s is less than Φ_m. W is the depletion region. (c): Electron energy diagram of an n-type semiconductor with surface state. Left: flat band at the surface. Φ_0 is a neutral level (see text). Center: surface in thermal equilibrium with the the bulk. Right: the semiconductor in contact with a metal

on the semiconductor side of the interface and the electrons which transfer into the metal form a thin sheet of negative charge confined within the Thomas-Fermi screening distance from the interface (≈ 0.5 Å). A dipole electric field is therefore established.

At the surface of a semiconductor the periodicity of the crystal lattice is terminated. In other words, the surface atoms have neighbors only on the semiconductor side. On the vacuum side, there are no neighbors with which the surface atoms can make bonds. Thus, each of the surface atoms in a covalent crystal has one broken bond in which only one electron is present, excluding the possibility of occurrence of surface reconstruction. The broken covalent bonds are called dangling bonds. Dangling bonds give rise to localized energy states at the surface of the semiconductor with energy levels lying in the forbidden gap. Surface states therefore exist. The localization of surface states arises from the imaginary part of the wave vector and these wave functions are evanescent waves which decay exponentially with distance. These surface states are usually continuously distributed in the band gap and are characterized by a level called the neutral level ϕ_0. The neutral level is the level where electrons fill up to make the surface electrically neutral without band bending. Clearly, the presence of the surface state at a covalent semiconductor surface tends to attract electrons from the conduction band, leading to band bending and a space charge layer even in the absence of a metal contact.

The model of band bending for crystalline semiconductors can be applied to a-Si:H as well. However, due to the disordered nature of a-Si:H, some differences exist. Figure 11 shows a schematic of Schottky-barrier formation for a metal and a-Si:H. Circles in the band gap on the a-Si:H side

indicate defect centers near the Fermi energy, which arise from a gap density of states large enough to pin E_F near midgap. An aspect of this configuration is that band bending is also feasible for a-Si:H in the absence of a metal contact. However, maintaining the electrical neutrality at the surface is achieved by ionized centers near midgap, in contrast with c-Si, in which the ionized donors or acceptor states lie near the band edges. With metal contact, charge in ionized centers is transferred to the metal layer. If the magnitude of the transferred charge is comparable to the surface defect density on the semiconductor, then additional band bending will occur.

Determining the distribution of space charge in the depletion region for a-Si:H is more complicated than for c-Si. For uniformly doped n-type c-Si, the positive charge distribution in the depletion region formed by ionized donors balances the equal negative charge on the metallic interface. The space charge density is normally equated to the constant donor density. As for a-Si:H, the positive charge distribution depends on the distribution of localized states and will therefore be a function of both position and energy [39]. The net space charge in the depletion region is determined by both ionized impurities and the localized states.

The most common Schottky diodes for a-Si:H are formed on undoped or intrinsic films. This is another difference from the case of c-Si, for which doped materials are always used to make Schottky diodes. Doped a-Si:H, either p or n type, contains large densities of defects [40] which enhance carrier recombination. In other words, the carrier lifetime of undoped a-Si:H is significantly longer than that of doped a-Si:H.

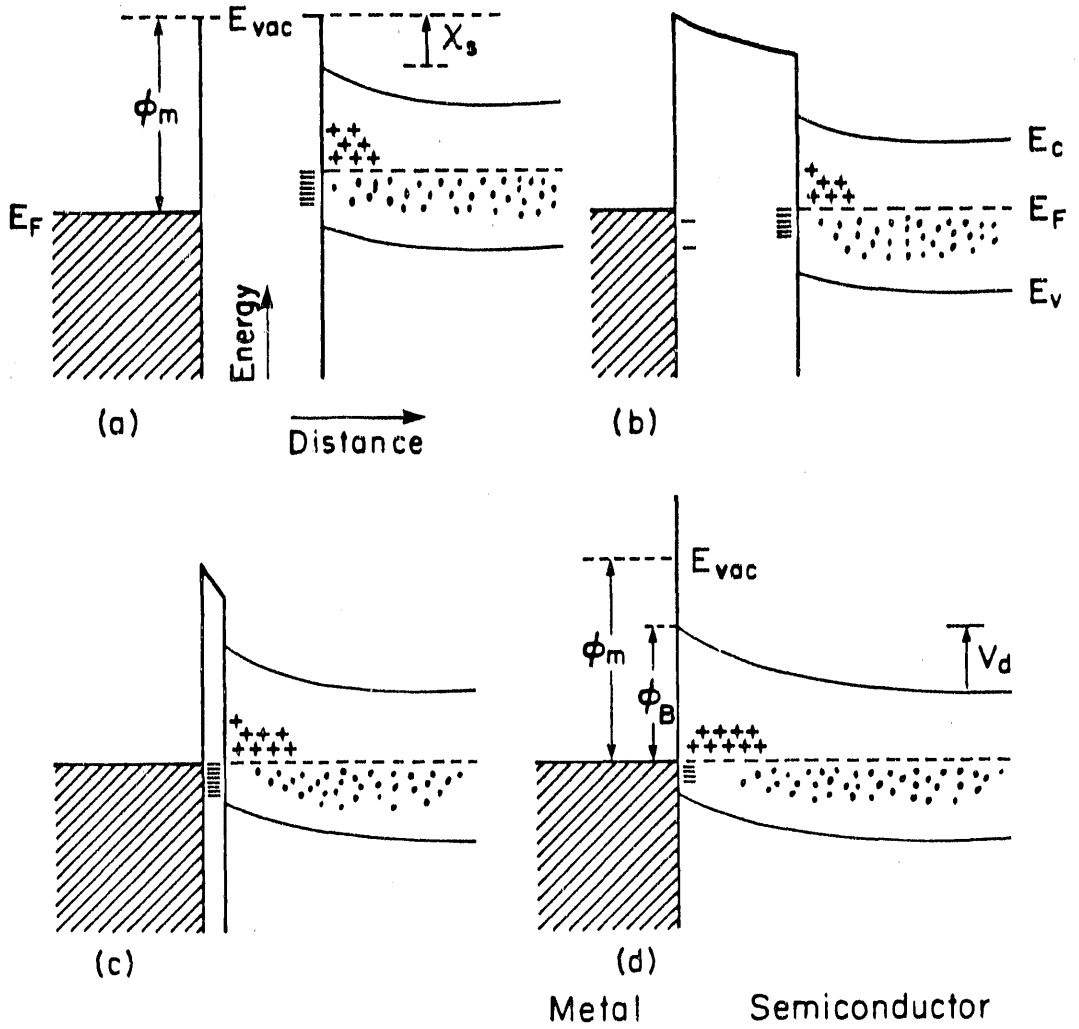

Fig. 11: Schematic of Schottky-barrier formation of a metal and a-Si:H. In (a) the metal is isolated from the a-Si:H, and in (b) and (c) they are in electrical equilibrium, and in (d), they are in intimate contact. (From Ref. 50)

PROPERTIES of a-Si:H

For a perfect crystal, the relative positions of atoms are determined by a few parameters: the size and shape of the unit cell and the locations of the atoms within the cell. In the one-electron approximation, the periodicity of potential in crystalline solids makes all electronic states extended and results the existence of well-defined band edges (van Hove singularities). However, in amorphous materials, the loss of long-range order, or the non-periodic potential, has the electronic states localized and the band edges are no longer sharp due to removal of the van Hove singularities. The former, arising from the effect of defects, gives well-defined energy states typically occurring in the energy gap, while the latter, from the effect of disorder, results in the band tail states. The extent of the band tail increases with increasing disorder. The weak bonds (i.e., the tail states) can, however, serve as precursors to the broken bonds (i.e., the deep states). With increasing bonding disorder, the density of strained bonds increases, and a certain fraction of these strained bonds will "break" and then appear as deep defect states [41].

The lowest energy configuration of silicon is one in which it forms tetrahedrally coordinated bonds at the optimal 109.5° bonding angles with four neighboring atoms. However, in a-Si:H, strains developed during film preparation can force certain atoms to bond with undesirable bond angles and be undercoordinated, or to bond in higher energy local configurations. Since thermal equlibrium is hardly met in preparing a-Si:H films, many defects can be frozen in with no opportunity for relaxation. Band tails extended into the band gap must then exist due to the disorder potential related to bond angle, dihedral angle, and bond length fluctuations.

Therefore, long-range order is absent in a-Si:H materials. Hence, only the atoms that are rather close to each other provide necessary information. However, this information is available in statistical form, because the disorder of an amorphous phase consists in part of spatial fluctuations in interatomic distance. The following are some of the properties of a-Si:H.

1. In a-Si, crystal momentum is not a good quantum number. Optical transitions, therefore, can be viewed as localized transitions. As a consequence, an increased efficiency of optical transitions is expected. In fact, the absorption coefficient for a-Si:H is found to be an order of magnitude larger than that of c-Si, in the visible range of the spectrum [42, 43]. The high absorption coefficient of a-Si:H makes it feasible for photovoltaic applications: 1μm of a-Si:H is sufficient to absorb most usable solar radiation, compared to 100μm for c-Si [44].

2. Localized states in the energy gap act as traps and recombination centers in a-Si, reducing the drift mobility of the carriers. In a-Si:H, however, the effect of combining hydrogen has been shown to cause a dramatic decrease of these defect states in the gap. The passivation effect of the hydrogen not only decreases the concentration of gap states but increases the stability against oxidation [45]. Experiment has shown that 1 monolayer (ML) of chemisorbed oxygen on a Si(111) surface requires an exposure of ~ 10^5 langmuir (1 L = 10^{-6} Torr-sec) of molecular oxygen [46], while more than 10^{11} L of oxygen is needed to acheive the same on a-Si:H [47].

3. One of the consequences of the high concentration of hydrogen is that the energy gap of amorphous Si is much larger than that of crystalline Si: Typically 1.7 ± 0.2 eV for a-Si:H compared to 1.1 eV for c-Si [43]. When a Si atom, for example, is surrounded by three Si atoms and one H atom in a

tetrahedral configuration, the greater Si-H bond strength (3.4 eV, compared to the Si-Si bond strength of 2.4 eV) results in a greater bonding-antibonding splitting. However, H is more electronegative than Si, so that the 1*s* orbitial of H lies below the $3sp^3$ hybridized orbital of Si. This shift of weight in the density of states given by a sharp reduction in the energy of some states near the top of the valence band serves to increase the energy gap with increasing H concentration [48].

4. For c-Si, the Fermi level is controlled by the high surface state density ($\geq 10^{14}$ $cm^{-2}eV^{-1}$), which shows as a sharp peak just below the Fermi level in UPS spectra [49]. Because the number and energy of the bulk defects are known, the amount of band bending at the vacuum/c-Si interface correlates well with bulk and surface state densities. The reconstruction of the cleaved c-Si(111) surface leads to one occupied surface state per atom. The presence of structural disorder and hydrogen at the surface of a-Si:H significantly reduces this density, which hampers the detection of surface states in a-Si:H. Further, the only approximately known properties of the detailed structure and distribution of electronic states in the bulk make the determination of the surface properities difficult. Neverthless, it is generally stated that surface state densities on a-Si:H between 10^{12} and 10^{13} eV^{-1} occur frequently [50].

5. a-Si:H films are often not homogeneous [51]. Because of the process of film growth, the first and the last few hundred atomic layer near the substrate and the surface may have a composition and structure that are quite different from that of the bulk. The top layer may be enriched or partially depleted of hydrogen, depending on out-diffusion and the hydrogen equilibration process. Such vertical heterogeneities have been pointed out in

the literature [52, 53]. Moreover, NMR data also suggested that even "device quality" a-Si:H films could contain regions with relatively low hydrogen concentrations interspersed in regions with higher concentrations [54].

6. Illumination with intense light (≈ 100 mW/cm^2) for several hours can cause structural changes known as the Staebler-Wronski effect. The Staebler-Wronski effect is caused by a reversible increase of the density of neutral dangling bond defects during illumination. The additional light-induced dangling bond defects are metastable, but disappear after annealing. An important feature of the Staebler-Wronski effect is the observation that the structural changes are not a direct consequence of the photon absorption process, but are caused in a more indirect way by the presence of both excess electrons and holes in excited states [54].

7. Infrared absorption (IR) is sensitive to heteropolar bonding and can give information on the H environments. The H vibrations are split into three groups of bands in the IR spectra. The high frequency band at 2000 to 2150 cm^{-1} is due to H motion along the Si-H bond. In contrast the group of lines from 800 to 1000 cm^{-1} and the bands at 600 cm^{-1} represent H motion transverse to the bond. The low-frequency band at 600 cm^{-1} is due to all H atoms (one, two, or three) bonded to a single Si moving in phase, while the band at 800 to 900 cm^{-1} is due to complicated displacements due to multiple-bonded H (two or three) to a single Si atom.

EXPERIMENTAL

The count rate (or intensity) I_{nl} of a photoelectron line from a particular subshell with quantum numbers n, l is determined by

$$I_{nl} = I_0 \, A' \, D' \, \Omega(\phi) \, \sigma_{nl} \, \Phi_{nl}(\alpha) \, \rho_{nl} \, \lambda_{nl} \, F(\eta, \kappa, \theta_i, \lambda_{nl}) \, . \tag{13}$$

I_0 is the incident photon intensity, A' is the effective sample area, D' is the detection efficiency of the analyzer and the detector, $\Omega(\phi)$ is the acceptance angle ϕ of the cylindrical mirror analyzer (CMA), $\Phi_{nl}(\alpha)$ is an asymmetry factor which expresses the angular dependence of the cross section σ_{nl}, ρ_{nl} is the atomic density, and λ_{nl} is the photoelectron escape depth. The attenuation depth of the incident photon beam is about 1000 Å, which is much greater than the photoelectron mean-free-path. Therefore, the photon flux can be considered to be essentially unattenuated over the range where measurable photoelectron signals are recorded. The function F accounts for the variation of effective photoexcitation of the sample from loss of photons due to reflection at the sample surface and from changes of the intensity I_0 within the escape depth λ_{nl} due to refraction of the light [55]. We briefly describe how the count rate is affected by each parameter.

The instrument factor affecting the count rate depends on the effective source area A' (the area seen by the analyzer) and the energy bandpass ΔE, provided a symmetric and flooded source is used [56]. According to Palmberg [57], the effective source area A' (or diameter ρ') follows

$$A' = A / \gamma \, , \tag{14a}$$

or

$$\rho' = \rho / \sqrt{\gamma}, \tag{14b}$$

where $\gamma = E_k/E_p$ is the retarding ratio for electrons in the analyzer, E_p is the analyzer transmission energy (or the pass energy), and ρ (A) is the circular aperture (area) of the analyzer. ρ has a diameter of 4 mm when the CMA runs in PES. The energy bandpass ΔE, on the other hand, increases linearly with the pass energy and it is also a function of analyzer design parameters [58]. The count rate, combining these two factors, is therefore proportional to [58].

$$I_{nl} \propto E_k/\gamma^2 \qquad (\frac{\Delta E}{E_p} = \text{constant}) \tag{15a}$$

or

$$I_{nl} \propto E_p^2/E_k \qquad (E_p = \text{constant}). \tag{15b}$$

With these relations, the CMA is allowed to be operated in either constant retarding-ratio mode (Eq. (15a)) or constant pass-energy mode (Eq. (13b)).

In the constant retarding-ratio mode, used for wide-scan spectra where high intensity is of prime interest, one has to let γ remained fixed so that the electron trajectories, determined by the electrostatic field between the cylinders, are unchanged. The kinetic energy of all electrons is reduced by a fixed factor γ, and the electrons enter the analyzer with varying energies.

On the other hand, in the constant resolution mode used for detailed spectra requiring good resolution, the pass energy E_p is fixed so that all electrons enter the analyzer with the same energy E_p. The transmission is inversely proportional to the kinetic energy (see Eq. (15b)). Moreover, because

the electrons impinging on the channeltron located at the exit of the CMA have a fixed energy, the detection efficiency D' contributes to the count rate by a constant factor only. In the current study, the constant resolution mode was employed.

Eqs. (14) and (15) fit well to a symmetric and flooded source. However, the source is generally not symmetric and not flooded. In this case, some cautions must be taken [59]. Accoding to Olson [59], for instance, if A_p is 2 mm × <1 mm, then the transmission will not change until ρ' is 2mm, i. e. until the kinetic energy E_k is four times the pass energy E_p. After that the transmission will decrease as the square root of E_k. At some point ρ' will reach the other focus dimension, and the transmission will start to follow Eq. (15). As far as the count rate is concerned, it will be proportional to the pass energy at high pass energies. Further lowering E_p the dependence will go as the $\frac{3}{2}$ power, and utimately at some low E_p the flooded source case applies, and the dependence will be quadratic.

The geometry used for photoemission experiments is depicted in Fig. 12. The light propagation vector, sample normal, and axis of the CMA are coplanar. The CMA accepts electrons in a cone between 36.3° and 48.3° with respect to its axis. This configuration assures maximum angle-integrated character free from angular effects, suitable for amorphous samples.

Photoelectrons are generally not emitted isotropically. Within the dipole approximation, $\Phi_{nl}(\alpha)$ follows as

$$\Phi_{nl}(\alpha) = \frac{1}{4\pi}[1 + \frac{\beta_{nl}}{2}(3\cos^2\alpha - 1)] \qquad (16)$$

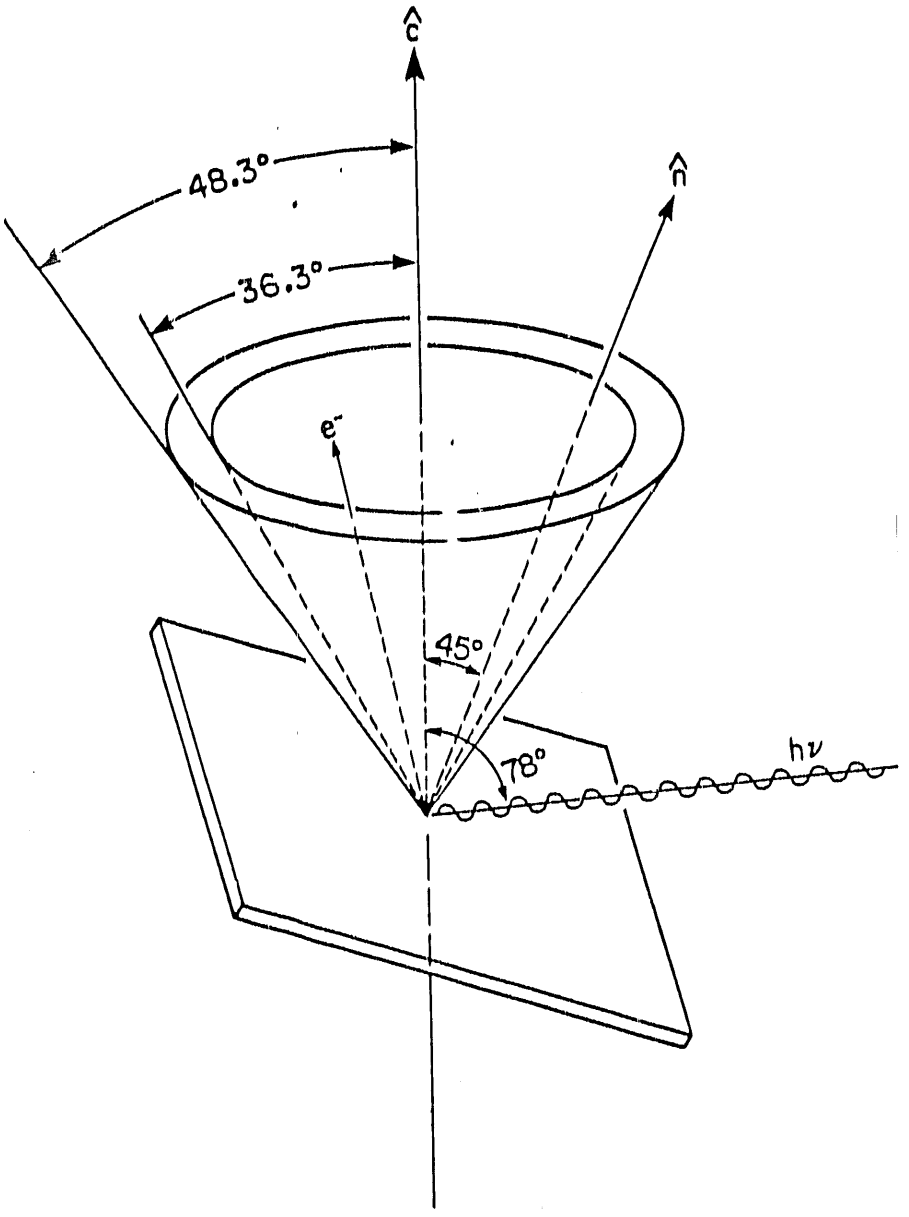

Fig. 12: Geometry of the sample surface and the CMA acceptance cone. The surface normal $\hat{n}$ is tilted 45° with respect to the CMA axis $\hat{c}$. The CMA acceptance cone extends from 36.3° and 48.3° with respect to $\hat{c}$. The photon is incident onto the surface at 78° with respect to $\hat{c}$

for polarized radiation, where α is the angle between the polarization direction of incident light and the direction of the emitted photoelectrons [60]. β_{nl} is a tabulated asymmetry parameter, sensitive to $|\Psi_i>$, $|\Psi_f>$, and photon energy [61]. Eq. (16) is applicable for both atomic orbitals and randomly oriented systems, whose non-preferential direction gives results averaged over all possible orientations.

Sample Preparation

Hydrogenated amorphous silicon substrates were prepared by rf sputtering. A polycrystalline silicon target was the upper electrode of the rf diode sputtering system. The single-crystal silicon substrate held at room temperature rested on a stainless steel disc which, in turn, mounted on the lower electrode with the same diameter as the target. The electrodes were pulled 1 inch apart, to offset the thickness the stainless steel disc. The pressure was reduced to 2×10^{-7} Torr before sputtering. A mixture of argon, with a partial pressure of 25 mTorr, and hydrogen at 2 mTorr, was then allowed to flow kinetically into the chamber during deposition. The 13.56 MHz rf power was set at 500 W, giving a power density of 2.74 W/cm^2. The silicon deposition rate was 6.7 Å/s. The thickness of the product was measured to be 2.2 μm.

The a-Si:H IR spectrum shows vibrational frequencies due to the SiH stretching mode (2100 cm^{-1}), wagging mode (638 cm^{-1}), and SiH_2 bending mode (897 cm^{-1}). Those SiH_x radicals are typical in an a-Si:H sample fabricated at room temperature [62].

The surfaces of the a-Si:H films needed to be chemically clean before insertion into the UHV experimental chamber in order to reduce sputtering

time. They were etched in HF and rinsed with distilled water. The cycle was repeated, if necessary, until water was able to wet the surface. Dry helium was used to blow off the liquid. The cleaned sample was then attached to an OFHC (Oxygen Free High Conductivity) copper rod screwed in the manipulator. An Ar ion-sputter gun was employed at normal incidence to remove residual contamination on the surface. Recently, Lu *et al.* [63] reported a comparison of the oxidation kinetics of HF-etched a-Si:H, c-Si and Ar-etched a-Si:H exposed to the ambient atmosphere. The results indicated a higher oxidation rate for the Ar-etched surface, signifying continuous production of free SiH_x radicals. Nevertheless, heat treatment should not be applied since large bubbles and holes might be formed on the heated sample [64].

The experiments were performed at the Synchrotron Radiation Center, University of Wisconsin. Monochromatized radiation was incident from a Seya/ERG beam line [23], scannable from 5 eV to over 1000 eV. EDCs were recorded at selected photon energies while the kinetic energy of the photoelectrons was swept. Photoelectrons were collected via a double pass CMA with channeltron multiplier detector and CAMAC pulse counting electronics. Measurements were always at a base pressure of 5×10^{-11} Torr.

The metal overlayers were obtained by evaporation onto the substrate kept at room temperature. Well-outgassed metal was evaporated from a tungsten basket. The pressure during evaporation never exceeded 1×10^{-10} Torr for Au and Ag and 8.5×10^{-10} Torr for Cr. The pressure never exceeded 3.5×10^{-10} Torr in obtaining a thick film. The thickness of the deposits was monitored by a quartz crystal oscillator. Thicknesses reported are those of an equivalent uniform homogeneous layer of metal and are integrated

thicknesses for successive evaporations, although the actual coverage may be inhomogeneous.

The Fermi energy was determined from a metal by the location of the inflection point in the high energy cutoff [65]. We use the Fermi energy, E_F, of the copper sample holder as the zero of binding energy. However, when the semiconductor surfaces become metallic, their Fermi levels became the reference for the metal E_F. The position of the top of the valence band maximum (VBM) in a semiconductor was determined at the slope intercept by extrapolating the tangent line to the leading edge of the EDCs back to the energy axis [66]. All spectra are normalized to the current from a nickel mesh placed in front of the sample and the raw experimental data were smoothed, using the Savitzky-Golay algorithm [67].

Au ON a-Si:H

Introduction

Au/c-Si is a good example to demonstrate the complexity of the metal-semiconductor interface [68]. This diffuse interface has triggered a number of researchers to use assorted surface-sensitive techniques, e.g., ultraviolet photoemission spectroscopy (UPS) [69 - 72], Auger electron spectroscopy (AES) [72 - 76], electron energy-loss spectroscopy (EELS) [72 - 74], low-energy electron diffraction (LEED) [73, 75, 79], transmission electron microscopy (TEM) [72, 76, 77] and MeV He^+ ion scattering [78]. The general picture of the growth of gold atoms on single crystal Si at room temperature can be sketched as follows. From the onset of deposition, Au atoms grow on the c-Si surface in a layer-by-layer fashion without interacting with the underlying Si. After a critical equivalent thickness is exceeded, Au commences to intermix with Si atoms. Because the lowest eutectic temperature of Au/Si is 370°C no equilibrium silicide phase can be formed at room temperature [79]. As deposition of gold increases, the interface ends up with the sequence: Si(sub.)–$(Au/Si)_1$–(pure Au)–$(Au/Si)_2$–(vac.), where (Au/Si) denotes intermixing. The thickness of the intermixed region in the vicinity of the vacuum is claimed to be < 1 ML in Ref. 69, but to be 1.5 ML in Ref. 80, where a monolayer is defined as the atomic density of a c-Si surface. The bonding environment of the intermixed Si atoms has been proven different from that of tetrahedrally bonded bulk-Si [81]. The subscripts for the intermixed Au/Si on each side of the pure gold layer mean that their electronic properties and chemistry are not necessarily the same [81].

We present the results in four subsections according to interfacial behavior: null (0 Å), low ($\theta < 2$ Å), intermediate (2 Å $< \theta \leq 9$ Å), and high coverage ($\theta > 9$ Å) regions. Then a discussion leads to explaining the behavior in each region.

Results

The evolutions of the density of states of the valence band taken at photon energies of 40 and 140 eV are shown in Figs. 13 and 14, with Au coverage in Å indicated at the ends of the spectra, while information gained from scanning core levels is shown in Figs. 15, 16, and 17. All spectra are normalized to the current from a nickel mesh placed in front of the sample.

The surfaces of a-Si:H

In Figs. 13 and 14, the EDCs from a clean a-Si:H surface are characterized by the emission from Si 3*p* states, bonding states of Si 3*p* – H 1*s* and Si 3*s* – H 1*s* orbitals. They are located at about 3, 6.5, and 10.8 eV below E_F, respectively. An argon peak at 9 eV also appears in the spectrum taken at a photon energy of 25 eV (not shown), a residue of the sputter-cleaning. Even though the Si 3*p* state appears as a featureless hump, its attenuation can tell us roughly the bonding status between Si and H. Since the formation of hydride bonds in a-Si appears as an intensity-transfer from the upper portion of the valence band to the vicinity of the Si-H bonding states, a decrease in intensity of the Si 3*p* states indicates the fraction of Si atoms bound to hydrogen. Or, oppositely, when a depletion of H atoms occurs, the intensity of the Si 3*p* state increases. The intensity of the Si 3*p* state increased with sputter time, after the loss of contamination. This suggests that the

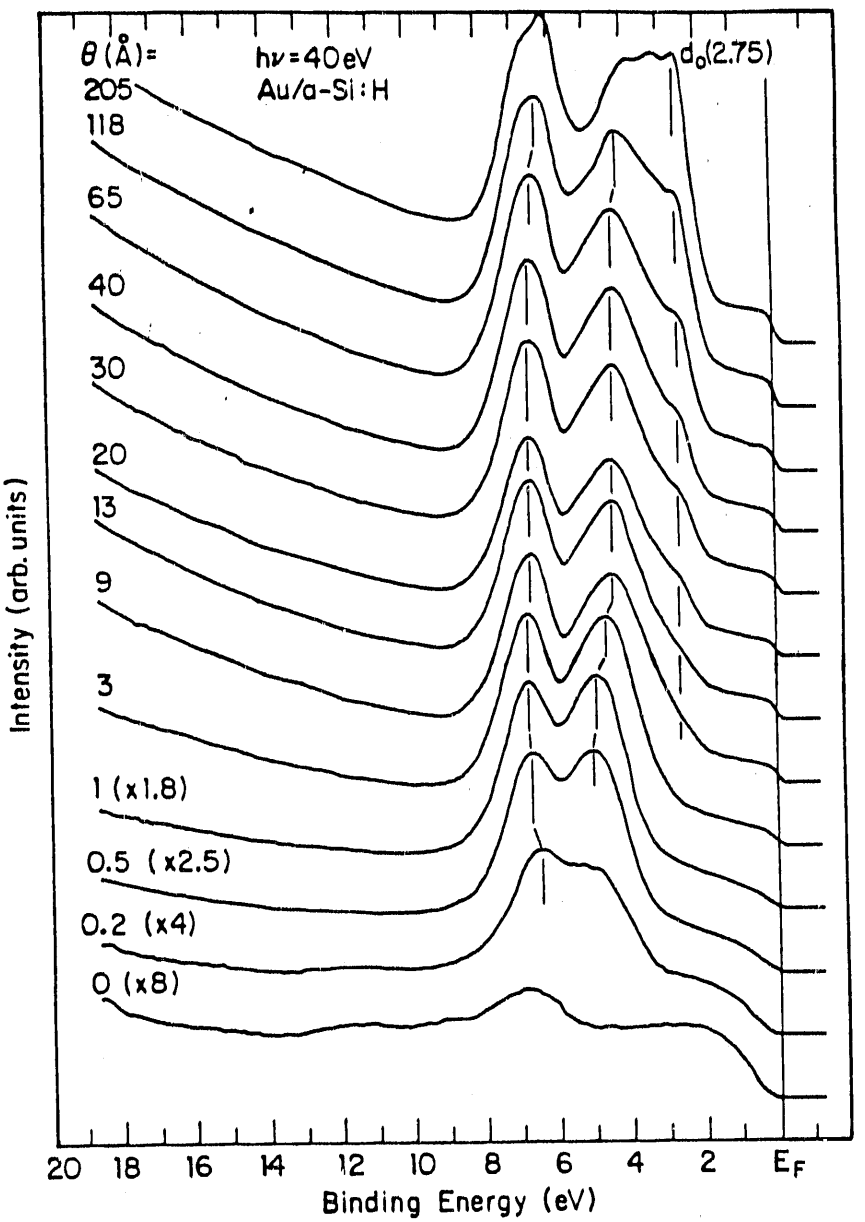

Fig. 13: Valence band spectra taken at hν = 40 eV to enhance the emission from Au 5*d* orbitals. All spectra are normalized to photon flux and then adjusted to the maximum magnitude at 205 Å. Note that the Au 5*d* derived states have already dominated the EDCs at the onset of the deposition. The Fermi level appears at 3 Å. A d_0 peak bulges out at 9 Å of Au and the intensity increases as coverage increases

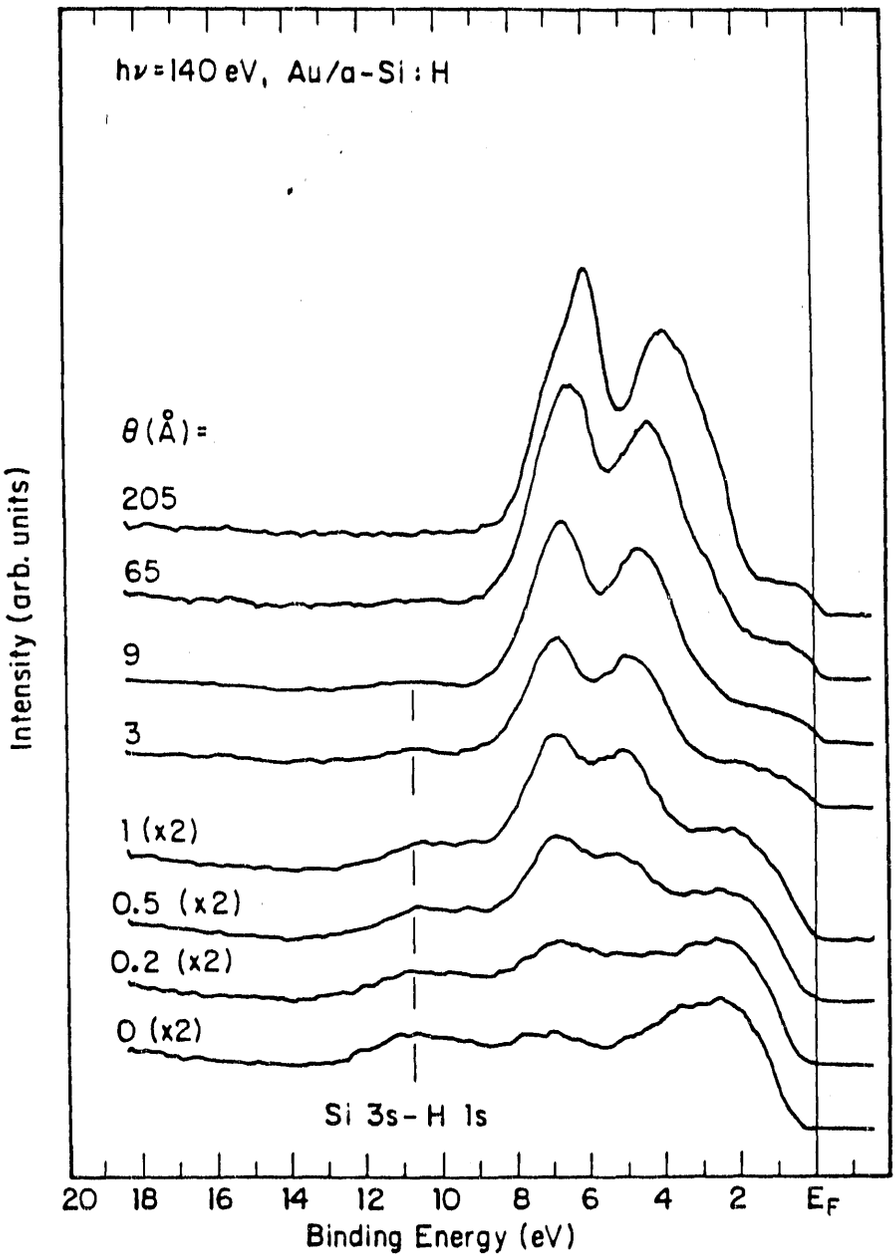

Fig. 14: Valence band spectra taken at hν = 140 eV to enhance the contribution from the *sp*-electron dominated substrate. Normalization scheme is the same as in Fig. 13. The bonding states due to Si 3*s* and H 1*s* orbitals are still visible at coverage over 9 Å, indicating the intermixed Si atoms with gold are those not bonding with H

surfaces have more Si-H bonds than the bulk does, in agreement with the study of Wagner *et al.* [82] and Láznicka [83].

Band-bending effects on the a-Si:H surface have been studied by several groups. Goldstein and Szostak [84] used the surface photovoltage (SPV) technique to study band-bending and surface states on a-Si:H. They found that the energy required to empty a surface-state is different from that to refill it. They then concluded the bands were bent upwards. An upward band bending was also reported by Clemens [85] and Foller and coworkers [86]. On the contrary, Winer *et al.* [87] used total-yield photoelectron spectroscopy to investigate a-Si:H, undoped and doped. They reported a difference of 0.3 eV in the activation energy and work function for undoped a-Si:H. Downward surface band-bending was thus proposed. Schade and Pankove drew a similar conclusion [88].

In the present work, the position of the Si $2p_{3/2}$ line implies the bands bend upward. Our fitted result, using the same schemes as in Ref. 89, to the Si $2p$ core level taken at $h\nu$ = 160 eV shows that the binding energy of a-SiH_0, Si $2p_{3/2}$ without bonding with hydrogen, is at 99.43 eV with respect to E_F at the surface. The energy of the crystalline Si $2p_{3/2}$ state has been reported to be 98.74 eV with respect to the VBM [90]. However, the energy of a-SiH_0 is 0.22 eV higher than that of c-Si, according to Ref. 89, using a bulk-sensitive scan. The energy of a-SiH_0 in bulk is therefore 98.96 eV with respect to the VBM. Assuming that the VBM is below E_F by 0.87 ± 0.05 eV (because for undoped material the Fermi level is pinned at midgap by ionized centers [91]), the binding energy of a-SiH_0 in bulk is then 99.83 ± 0.05 eV. Thus, bands at the surface are bent 0.40 ± 0.05 eV upward.

Low-coverage region ($\theta < 2$ Å)

In Fig. 13, the density of states of the valence band shows the evolution of the Au 5*d* spin-orbit split states. At the lowest coverage, the binding energies of the two prominent spin-orbit split Au 5*d* peaks are 6.53 and 5.03 eV. As coverage increases, they move oppositely, consequently increasing in separation. Further, the d band width expands. However, the contribution from the a-Si:H substrate is seriously masked by the higher cross section of the *d* orbitals from the deposits. The valence band spectra in Fig. 14, where the radiation was tuned to emphasize the Cooper minimum for atomic gold, supply information complementary to that in Fig. 13. Looking at the spectra, we can easily realize that the emission from both Si 3*p* and Si 3*s* – H 1*s* bonding states shows no change in binding energy, but only an attenuation of intensity.

In Figure 15, we present surface-sensitive data using a photon energy of 160 eV to detect the emission from the Au 4*f* and Si 2*p* core levels. As shown in Fig. 15, the Si 2*p* core level shifts to lower binding energy with increasing coverage, meaning the VBM continues to bend toward the Fermi level. The shift is 0.45 eV, at coverages from 0 Å to 1 Å, according to the fitted values. With E_F aligned across the interface, the shift is clearly within the band-bending uncertainty given above. This indicates that the 0.40 ± 0.05 eV band-bending value is reasonable. Also apparent in Fig. 15 is no appreciable line-shape change during the movement. The same features can also be appreciated in Fig. 16, where a bulk-sensitive scan with a photon energy of 110 eV was used. No lines due to chemical shifts appear, indicating that interaction between gold and a-Si:H in this region is weak. Furthermore, the intensity of the Si 2*p* states decreases as coverage increases. In the Au 4*f* core

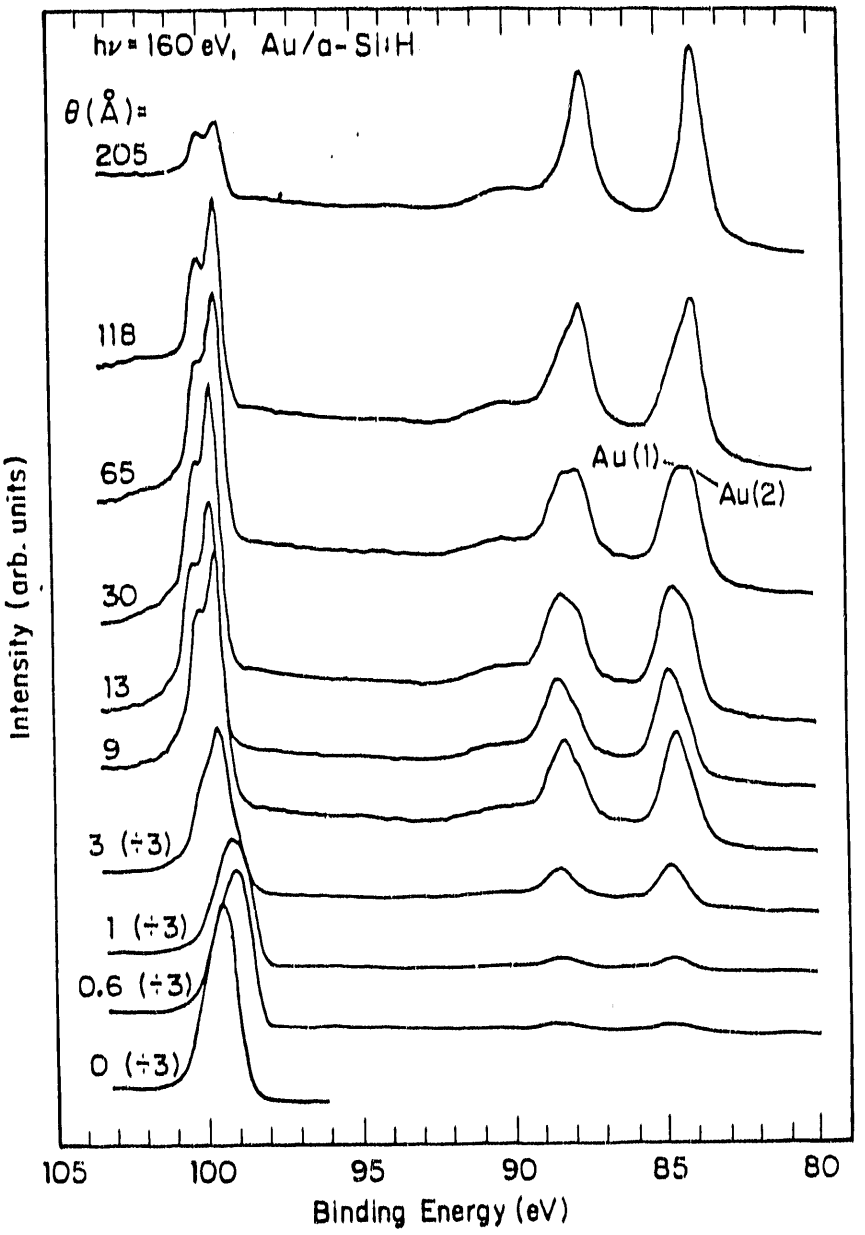

Fig. 15: Surface sensitive core level EDCs taken at hν = 160 eV. The small bump in the high binding energy side of the Au $4f_{5/2}$ state is due to Au NVV Auger emission. Development of two sets of Au 4*f* states are clearly seen. Si 2*p* spin-orbit splitting is easily differentiated at over 9 Å of Au

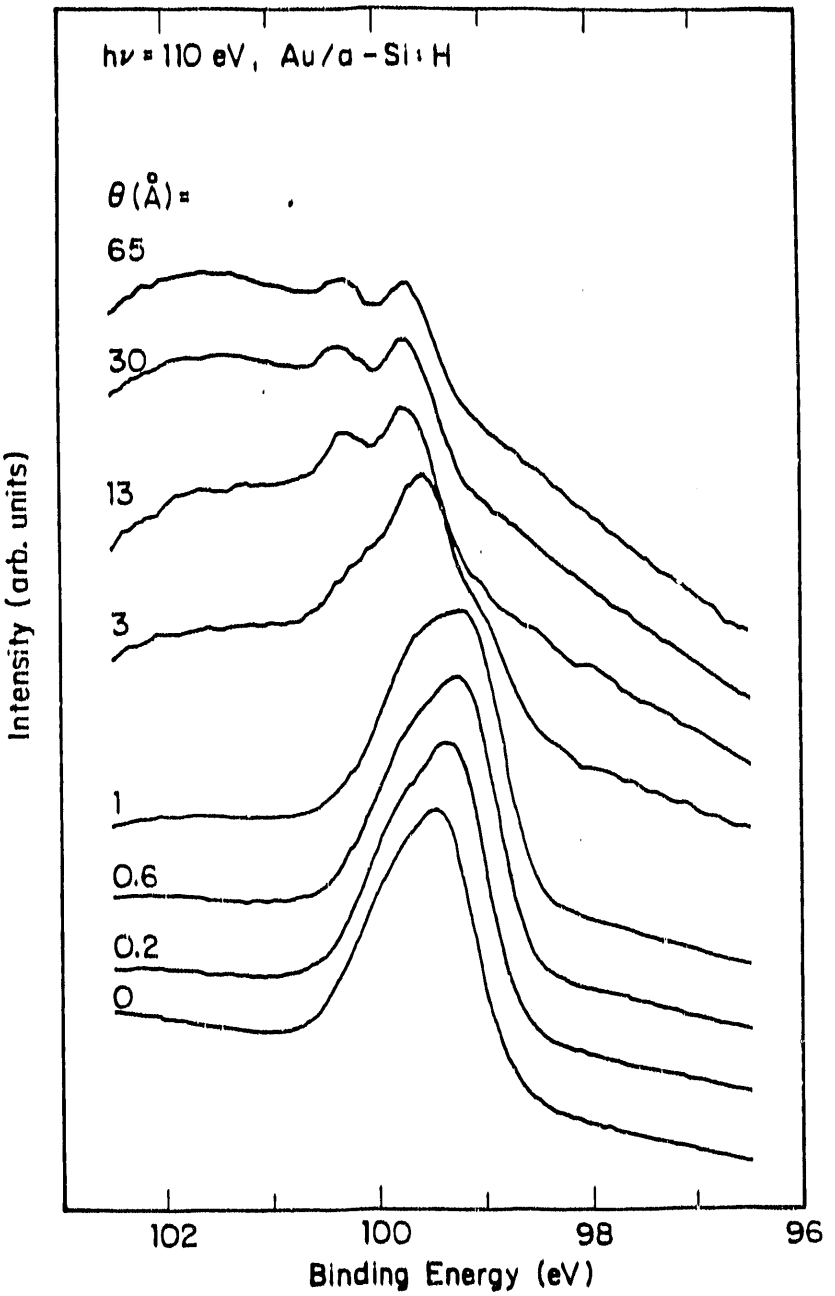

Fig. 16: Bulk-sensitive core level EDCs taken at hν = 110 eV

levels, a shift of 1.1 eV to higher binding energy at the lowest coverage is observed, with respect to the bulk value (83.9 eV). The shift is reduced to 0.9 eV at 1 Å of Au deposition.

In summary, we assign the initial stage (≤ 1 Å) of gold evaporated onto the a-Si:H surface as a *band-bending* region with no significant chemical reaction.

Intermediate region (2 Å ≤ θ ≤ 9 Å)

From Fig. 13 the presence of the Fermi level in the valence band spectra at coverages above 2 Å means that the interface has become metallic. This is evidence that Au atoms have already clustered enough to show a Fermi level. A rapid movement of the Au $5d_{5/2}$ derived state toward the Fermi level is noticed, whereas the Au $5d_{3/2}$ derived state exhibits much less change. The centroid of the Au 5*d* band thus continues to shift toward the Fermi energy, and the band width keeps increasing.

Figures 15 and 16 show a drastic change in the emission from the Au 4*f* and Si 2*p* core levels, both in line shape and binding energy. From Figs. 15 and 16 the energy of the Si 2*p* core lines shifts away from the trend of the band-bending region and moves from 99.13 eV at 1 Å to 99.60 eV at 3 Å. Likewise, the Au 4*f* lines shift in the same direction as the Si 2*p* lines to higher binding energy, from 84.8 eV at 1 Å to 84.9 eV at 3 Å. Most significant of all, however, is the altered line shape. The distinct feature is the moderate intrusion of the Si $2p_{1/2}$ peak. This suggests that an interaction between gold and silicon occurs in the interface. Specifically, Si atoms have been set free by absorbing energy released from clustering gold.

As gold clusters grow in size, when a Fermi level is detected they provoke a reaction with the underlying a-Si:H substrate. However, the reaction occurs at regions deficient in hydrogen. Referring further to Fig. 14, we observe that the peak due to the Si 3*s* – H 1*s* bonding state is still visible, but attenuated. On the contrary, the Si 3*p* state is completely gone. These suggest that the Au atoms forming clusters can be located "over" both Si-Si and Si-H bonds, but the reaction between Au and Si occurs at regions devoid of hydrogen. This is demonstrated by the reduced intensity of those Si atoms which do not bond with hydrogen and the altered line shape of the Si 2*p* levels. Another justification can be made by noticing that a shoulder appears on the low binding energy side of the Si 2*p* states (Figs. 15 and 16). This feature, at about the same energy as in the low-coverage region, corresponds to the Si atoms in Si–H bonding states. The a-Si:H IR spectrum shows vibrational frequencies due to the SiH stretching mode (2100 cm^{-1}), wagging mode (638 cm^{-1}), and SiH_2 bending mode (897 cm^{-1}). Those SiH_x radicals are typical in an a-Si:H sample fabricated at room temperature [31]. Since the Si–Si bond energy is 2.35 eV while that of Si–H is 3.4 eV [32], it is easier to break Si–Si bonds or weaken the back bond of dangling bonds. Thus the clusters form primarily on regions of the surface deficient in hydrogen.

<u>High-coverage region ($\theta \geq 9$ Å)</u>

The evaporation rate was increased by 1 Å/min for coverages between 13 Å and 118 Å. As we will see, this region shows similarities to, as well as differences from, the work on c-Si. In what follows, coverages under discussion will be, unless stated otherwise, those below 118 Å.

In this region, the distinctive double-peak of the Au 5*d* band does not vary dramatically in intensity, line shape and energy position, as are seen in Figs. 13 and 14. However, in Fig. 13, a peak, labeled d_0, appears at the top of the Au 5*d* antibonding state. Its position, 2.75 eV below E_F, is coverage independent, but the intensity increases as the amount of gold increases. The d_0 peak, however, loses its prominence at higher photon energy. The growth of the d_0 peak is the most pronounced change in the valence band over this region. Even so, the appearance of the valence band is far from that of bulk gold, even at the highest coverage.

A number of groups have studied the behavior of gold in the form of small particles [92, 93]. Pertinent in their work is the evolution of the d_0 peak in the vicinity of the antibonding area. The development of the d_0 peak has exhibited a strong dependence on the volume of a cluster. The larger the volume, the more prominent is the d_0 peak. Furthermore, theoretical calculations have precluded an explanation of the two prominent peaks of the Au 5*d* band as simply due to spin-orbit splitting, but rather a strong crystal field effect comes into play [94].

Spectra from both Au 4*f* and Si 2*p* core levels provide information that characterizes the region in a more sensible way. Observing the development of the Si 2*p* core lines as shown in Figs. 15 and 16, we have no trouble differentiating the spin-orbit split peaks. Furthermore, it is interesting to note that the intensity of the Si 2*p* core lines exhibited in Fig. 15 remains quite the same regardless of coverage, except for the highest coverage. The binding energy of the Si $2p_{3/2}$ line peaks at 99.83 eV at 13 Å of thickness, and then shifts gradually to lower values with increasing coverage.

In addition to the well-resolved Si 2*p* spin-orbit core levels in the high coverage region, the most remarkable phenomenon is the development of two sets of Au 4*f* core levels. We call the higher binding energy peak in the vicinity of Au $4f_{7/2}$ Au(1), and the lower binding energy $4f_{7/2}$ peak Au(2), as shown in Fig. 15. Naturally, the same assignment can also be made for the Au $4f_{5/2}$ lines. (The small hump at the high binding energy side of the Au $4f_{5/2}$ peak is from Au NVV Auger electrons.)

In Fig. 15, the Au(1) line shows a monotonic decrease in binding energy as coverage increases. However, larger Au deposition does not cause Au(1) to grow in intensity. A closer examination of the line shape at 9 Å , shows a barely perceptible asymmetry on the low binding energy side of Au(1). This is the position where Au(2) develops. At increased coverage, it becomes more and more evident. The steady growth of Au(2) makes it comparable to Au(1) at 65 Å, and larger for larger thickness. However, the binding energy of Au(2) is coverage independent and remains fixed at a value of 84.15 eV [95].

In order to determine why the intensity of the Au(1) 4*f* or Si 2*p* core lines does not change, we used a different approach: increasing the evaporation rate to 4 Å/min and increasing the coverage to 205 Å in a single step. First of all, from Fig. 15 it is clearly seen that the intensities of the Si 2*p* and Au(1) lines drop simultaneously, while that of Au(2) keeps on growing. Secondly, a binding energy shift of the Au(2) (83.98 eV) to the bulk gold value (83.9 eV) appears. At this point, we attribute the higher binding energy component (Au(1)) to intermixed Au and Si, and the lower binding energy set to pure gold alone. This assignment is indeed in agreement with the work of Ref. 80, whose core-level photoemission study of Au on c-Si indicated the

presence of two Au 4*f* components. They assigned the higher binding-energy component to Au silicide, and the lower to Au itself.

For a coverage as high as 205 Å, the Si 2*p* peak is still present as shown in Fig. 15. The thickness far exceeds the escape length of the Au overlayer [85]. If the interface were abrupt, we would anticipate seeing nothing originating from the a-Si:H substrate. One might argue that the surfaces are certainly rough from either the rf-sputtering sample fabrication or the Ar-etch cleaning treatment, and some clean Si remains in "shadows". To this argument, our study of Ag on similar samples of a-Si:H [43], where no strong interactions occur, revealed no signals from the a-Si:H substrate above 65 Å of silver. Therefore, the continued presence of Si at the surfaces is due to Si outdiffusing through the Au film, consistent with expectations of a high diffusion coefficient for Si in Au.

Discussion

We depict the behavior of the Au 5*d* band in Fig. 17 against coverage. Figure 17(a) plots the individual movement of the two peaks and Fig. 17(b) the energy separation between them. Also included in Fig. 17(a) is the centroid of the 5*d* band marked as "o". Note that what is not shown in Fig. 17 is the d_0 peak whose track would be a straight line located at 2.75 eV. In Fig. 17(b), the two peaks in the Au 5*d* band are separated by 1.5 eV, the atomic Au splitting [96], at the lowest coverage. This indicates that the initial gold deposit is in a dispersed, atomic-like state. As coverage increases, Fig. 17(b) demonstrates a monotonic increase in separation at low coverages followed by a plateau starting at 9 Å. Needless to say, the shift of the centroid toward the Fermi level with increasing coverage is greatly assisted by the presence of the d_0

peak. The evolution of the double-peak separation reflects a trend similar to that found for Au on Si(111) by Braicovich *et al.* [69] and for Si(100) by Carrière *et al.* [70]. However, the trend is unlike that in Iwami *et al.*'s work [71] on Si(111)2×1, which shows a constant separation at low coverages.

We plot the development of the binding energy of the Au $4f_{7/2}$ and Si $2p_{3/2}$ core levels in Figs. 18 and 19, where the former tracks individual binding energies and the latter the energy separation between the Au $4f_{7/2}(1)$ and Si $2p_{3/2}$ core lines. The lines in Fig. 18 serve as a guide to the eye, and are not fitted curves. We simplify by omitting spin-orbit symbols hereafter.

Figure 18 reveals a monotonic decrease in binding energy for both the Au(1) and Si 2*p* lines at low coverages (the band-bending region), followed by an increase (the intermediate coverage region) and then a decrease (the high coverage region) in binding energy. The Au(2) core level, however, remains at the same value independent of thickness. We can see that the binding energy of the Si 2*p* line changes more rapidly than that of the Au(1) line at thicknesses below 13 Å. Above 13 Å, the variation rate of Au(1) and Si 2*p* are basically the same. This implies that Si 2*p* orbitals seem to be more vulnerable to the chemical environment, particularly in the intermixing region where the interaction between the deposit and substrate commences. This strongly suggests that the local strain of the a-Si:H network is disturbed by clustering gold atoms. The disturbance, however, is slow enough that subsequently incoming gold atoms see a different unrelaxed substrate. The slow relaxation process can also explain a decrease in the Si 2*p* – Au(1) energy separation, for example, by 0.2 eV at 9 Å, over 12 hours later at the same coverage. The decrease resulted from an observation of a shift to lower binding energy in both core lines. Láznicka [83] has studied an ion-sputtered

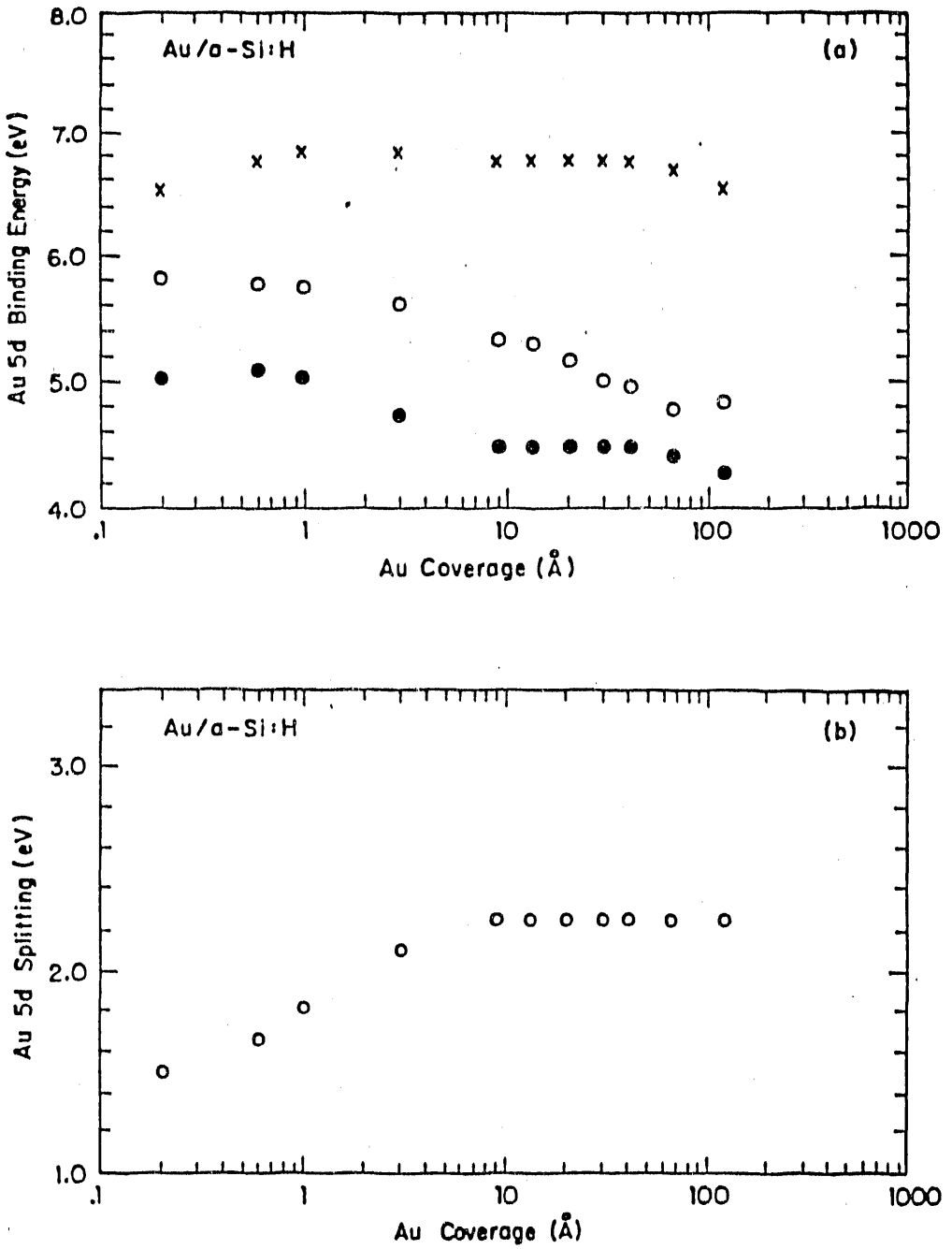

Fig. 17: Individual evolution of Au 5d states. (a): ×: Au $5d_{3/2}$ state, •: Au $5d_{5/2}$ state. Also included is the centroid of the Au $5d$ states at each coverage, marked as "o". (b): the energy separation between Au $5d_{3/2}$ and $5d_{5/2}$ states

a-Si:H surface. He found that a dramatic increase in a hydrogen-bond-related Auger peak appeared after the surface had remained *in situ* in a vacuum chamber for 24 hours. He claimed that hydrogen embedded in the bulk had diffused to the surface because of a concentration gradient at the surface induced by the argon ion sputtering of H atoms. This implies that the dangling bonds on the surface disappear not only by reconstruction but also by bonding with H atoms diffused from the bulk. Carrière *et al.* have done a comparison study of the Au-Si interface using AES, with ordered Si(100), and disordered, ion-bombarded Si(100) substrates [97]. They reported that gold was gettered by bulk defects under the amorphous surface. This mechanism constrained the Si diffusion coefficient and caused silicon to disappear at a thickness over 23 Å. This effect did not occur on ordered Si(100) substrates. More interestingly, diffusion of silicon is relatively slower in a disordered Si(100) substrate than in an ordered one, supported by detection of an increased silicon signal in the disordered substrate after 12 hours. Their work and ours leads to the important point that an amorphous semiconductor surface takes time to relax fully after the surfaces have been sputtered. Metal deposits like gold do not assist the relaxation.

As displayed in Fig. 19, the energy separation between the Au(1) and Si 2*p* lines increases below 13 Å of Au followed by a plateau. At this point, regarding the features shown in Fig. 19, it is worth mentioning that at low coverages the Au/a-Si:H interface does not behave the same way as Au/c-Si does [69, 71]. Braicovich *et al.* [69], using a Si(111) substrate, did not observe an appreciable movement of the Si 2*p* core levels and the Au 4*f* – Si 2*p* energy separation was basically constant at low coverages. Iwami *et al.* [71], who also explored Si(111)2×1, reported that the energy separation between Au 4*f*

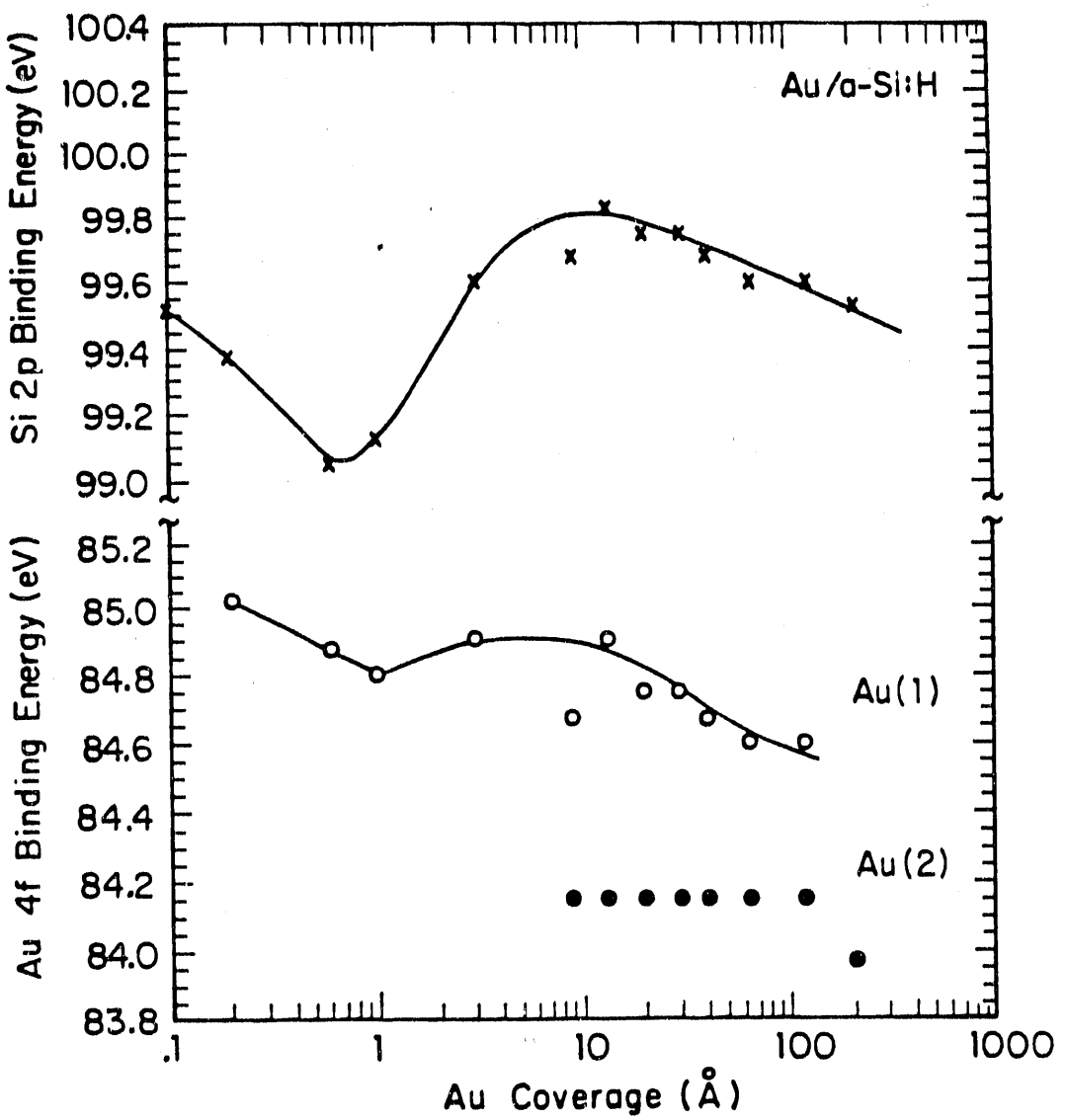

Fig. 18: Evolution of the binding energy of the Au $4f_{7/2}$ (Au(1): o, Au(2): •) and Si $2p_{3/2}$ (×) lines. The line drawn is a guide to the eye

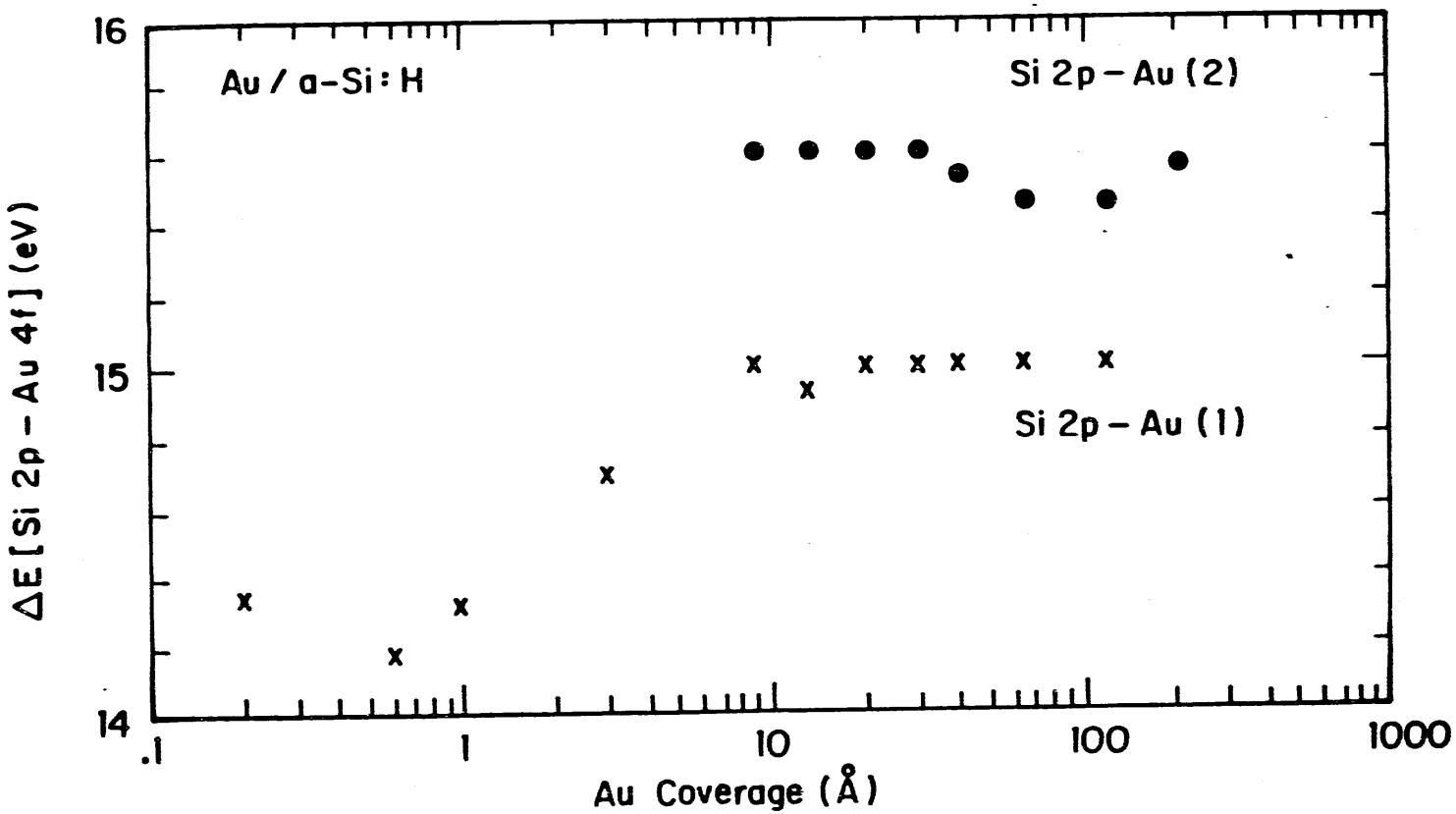

Fig. 19: Energy separation between Au $4f_{7/2}$ and Si $2p_{3/2}$. ×: Au(1) and Si 2*p*, •: Au(2) and Si 2*p*

and Si 2*p* had a minimum at about one monolayer of gold coverage. They further showed that a Fano-like resonant emission of the Au 5*d* peak accompanied by the Si 2*p* core excitation took place at this coverage [98]. On the contrary, our study clearly exhibits features with no similarity to the c-Si results in the initial low-coverage region. Moreover, the rigid Au(1)–Si energy separation and nearly constant intensity of Au(1) in the high-coverage region strongly indicate that the development of Au(1) is associated closely with Si.

In the case of the interface formed by Au on c-Si, there is a pure gold layer sandwiched by intermixed Au/Si at high coverage. In the Au/a-Si:H interface, we find no such layer. As a matter of fact, the two-component feature of the Au 4*f* core levels is always present in a bulk-sensitive scan (not shown) with an escape depth of 25 Å. This, accompanied by undiminished emission from the Si 2*p* core level from Fig. 16, suggests the absence of a pure Au layer. In other words, the interface consists of the intermixed gold along with pure gold, regardless of coverage, after a certain critical thickness is exceeded.

Up to now, there have been four models proposed for the Au/c-Si interface. They are the interstitial model [99], the screening model [74, 79], the thermodynamic model [100, 101], and the chemical-bonding model [72]. All these models emphasize particularly the effect of the gold atoms in the initial stage. We briefly describe the essence of each model. We will see later how applicable each model is to the current study. Tu's interstitial model [99] predicts Au atoms continuously exert stress on the Si lattice, thereby causing breakage of Si–Si bonds and resulting in a silicide-like compound. This occurs at the instant of arrival of the Au atoms. Hiraki's screening model

[79], which was created to explain the existence of an unreacted thickness of Au, postulates the necessity of a critical thickness of Au to provide metallic electrons for electronic screening of the covalent bonding of Si. The effect of metallic screening is to weaken the Si–Si bond. The thermodynamic model [84] explains a core binding energy shift of the Si 2*p* level due to metal deposits from thermodynamic properties of the bulk constituents. Iwami's chemical-bonding model [72] addresses the bonding between gold and silicon that occurs below 1 ML thickness, accomplished by a charge transfer between the Si surface state and Au 6*s* valence electrons.

Applying the four models used for the Au/c-Si interface to the current system, we find none of them explain satisfactorily Au/a-Si:H. First of all, the existence of a nonreacted band-bending region precludes the interstitial model, an instantaneous stress of the substrate surface region by the metal deposit. Second, the nonreacted region of the interface, 1 Å, is not thick enough to justify the applicability of the screening model, where a minimum of about 5 monolayers is required [74]. Moreover, one of the premises in the screening model is a substrate energy gap less than 2.2 eV and a static dielectric constant larger than 12 [79]. For a-Si:H sputtered at room temperature, the dielectric constant is about 7 [102]. Correspondingly, our system does not fit the criteria of the model. Third, the largest magnitude of the Si $2p_{3/2}$ core level shift (0.3 eV at 13.3 Å) is smaller than the thermodynamic model would predict (0.6 eV at 50 at. % of Si) [101]. Last, the absence of a nearly constant separation of the two main peaks of the Au 5*d* states as well as a minimum occuring in the Au 4*f*–Si 2*p* separation preclude the applicability of the chemical-bonding model. Note that surface states, a necessity in the chemical-bonding model, exist on the surface of the a-Si:H

material [91].

Tsai *et al.* [103] have studied the Au/a-Si:H system but used other techniques. They reported that intrinsic differences existed between the interactions of Au with crystal silicon and hydrogenated amorphous silicon. For example, a crystallization phenomenon occurred after a thin film of 80 Å of Au and 350 Å of a-Si:H was annealed at T > 150°C, but below the Au/Si eutectic temperature of 370°C. Therefore, we do not expect identical behavior of Au on a-Si:H and on c-Si. We believe the surface structure of a-Si:H is important to rationalize the behavior of the Au/a-Si:H interface. Roughness of the surfaces [104] might also contribute, but a full understanding of the surfaces is more demanding. Because of a lack of knowledge, we can not comment what kind of role that the surfaces of a-Si:H would play in order to explain discrepancies [105].

Cr ON a-Si:H

Introduction to Cr on c-Si

Detailed photoemission studies of the electronic structure of the Cr/c-Si interface have been reported by a number of groups [106-108]. The consensus picture for the evolution of the interface is an initial inert Cr layer, followed by an intermixed layer and, ultimately, the development of bulk Cr metal, with increasing coverage. The inert threshold coverage has been shown essential to the formation of the following intermixed layer. The latter has exhibited silicide-like valence bands. The eutectic temperature for a $CrSi_2$ phase is about 450°C. The intermixed layer has shown a great degree of instability when exposed to oxygen [108, 109].

Results and Discussion

We present some representative EDCs in Figs. 20 to 23. The changes of the valence band EDCs with Cr deposition are shown in Figs. 20 and 21, with photon energies of 21 and 55 eV, respectively. From the figures, it is clear that the 21 eV photon energy scan emphasizes the Cr 3*d* states, as well as the lower part of the Si valence band. However, at coverages below 6 Å, features more than 6 eV below the Fermi level, E_F, are severely distorted by the secondary electron emission as well as by the contribution from argon atoms. The argon peak, at about 9 eV below E_F, is a residue of the sample preparation. Spectra taken at $h\nu$ = 55 eV manifest clearly the emission from the lower part of the valence band.

Core level spectra are shown in Figs. 22 and 23. The former, taken at a photon energy of 110 eV, are to monitor the emission from the Cr 3*p* states,

while the latter, taken at hν = 160 eV, are for the Si 2*p* states. The photon energies were selected to enhance surface sensitivity, with an escape depth on the order of 5 Å. The combined resolution of the monochromator and the energy analyzer is about 330 meV for hν = 160 eV and 210 meV for hν = 110 eV. All spectra are normalized to the photon flux and further scaled in the figure in accordance with the same magnitude. Initial state energies are referred to E_F.

Low-coverage region (≤ 2 Å)

As shown in Fig. 21, a "clean" a-Si:H spectrum has two main features, located at about 3 and 6.5, which are associated with the emission from Si 3*p* states and bonding states of Si 3*p* – H 1*s*, respectively. Figure 22 shows that the energy of the substrate Si $2p_{3/2}$ line at the highest intensity is 99.6 ± 0.1 eV. Because of possible effects from oxygen, we review previous work on the effects of oxygen in a-Si:H films. Kärcher and Ley [110] reported that the oxygen-induced spectral contributions appeared at 6.7 and 8.0 eV in oxygen-doped a-Si:H. Yang *et al.* [111] reported that for an a-SiO_x:H film, the O 2*p* character was at 7 eV. The absence of these features in Fig. 20 explicitly indicates that residual oxygen does not significantly influence the electronic states of the a-Si:H substrate. Note that the cross section of the Si–O bond at hν = 21 eV has been claimed to be at least fifteen times higher than that of Si–Si or Si–H bonds [110]. Bulk sensitive scans at hν = 110 eV (not shown) show no states due to chemical shifts either.

Upon Cr deposition, it is evident from Figs. 20 and 21 that the emission from the Cr 3*d* orbitals promptly dominates the vicinity of the Fermi level region. More significantly, a Fermi level appears at the lowest coverage, 0.2

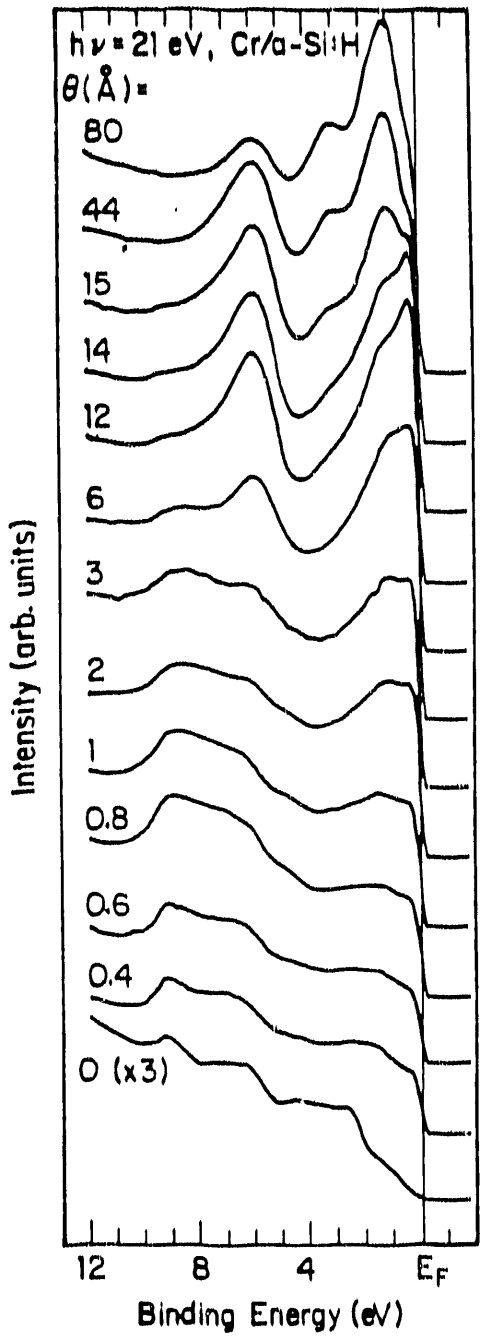

Fig. 20: Valence band spectra taken at hν = 21 eV. The number in the high binding energy end gives the Cr thickness in Å. All spectra are normalized to photon flux and then adjusted to the maximum magnitude at 80 Å. Note that at the onset of the deposition the Cr 3*d* derived states already dominate the vicinity of the Fermi level the EDCs. The Fermi level appears at 0.2 Å

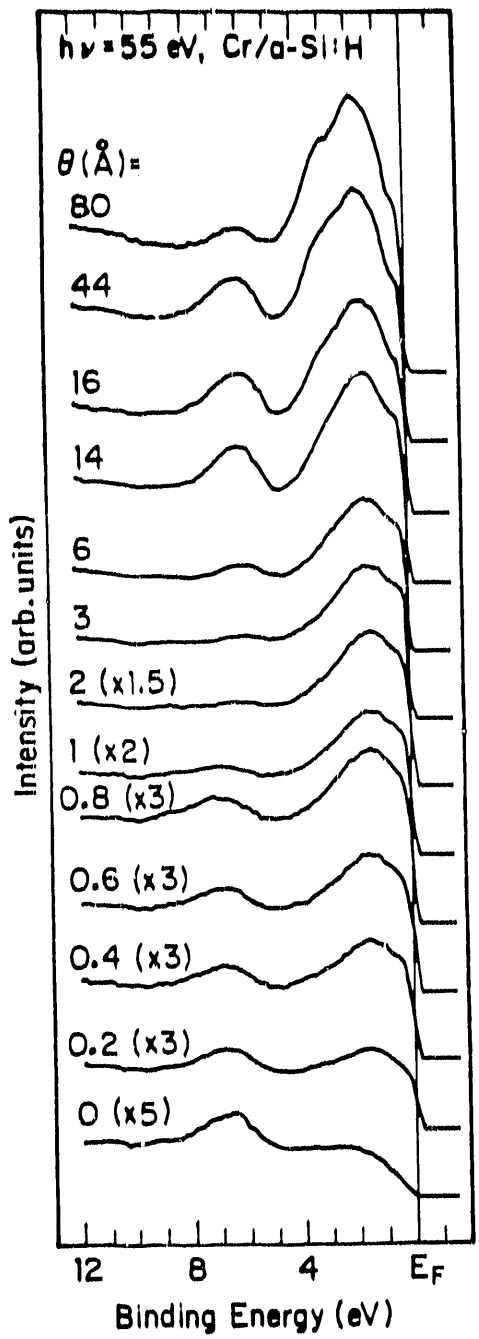

Fig. 21: Valence band spectra taken at hν = 55 eV to enhance the contribution in the lower part of the valence band at low coverage. Normalization scheme is the same as in Fig. 20. The bonding states due to Si 3*p* and H 1*s* orbitals are visible at coverages below 1 Å

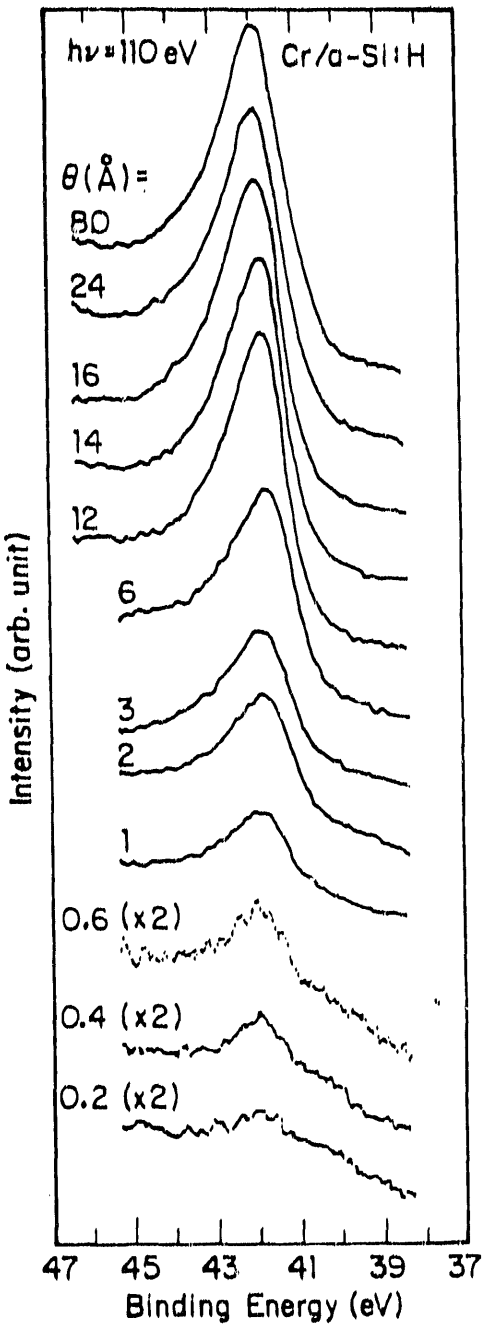

Fig. 22: Surface-sensitive core level EDCs taken at hν = 110 eV to monitor the emission from the Cr 3*p* line

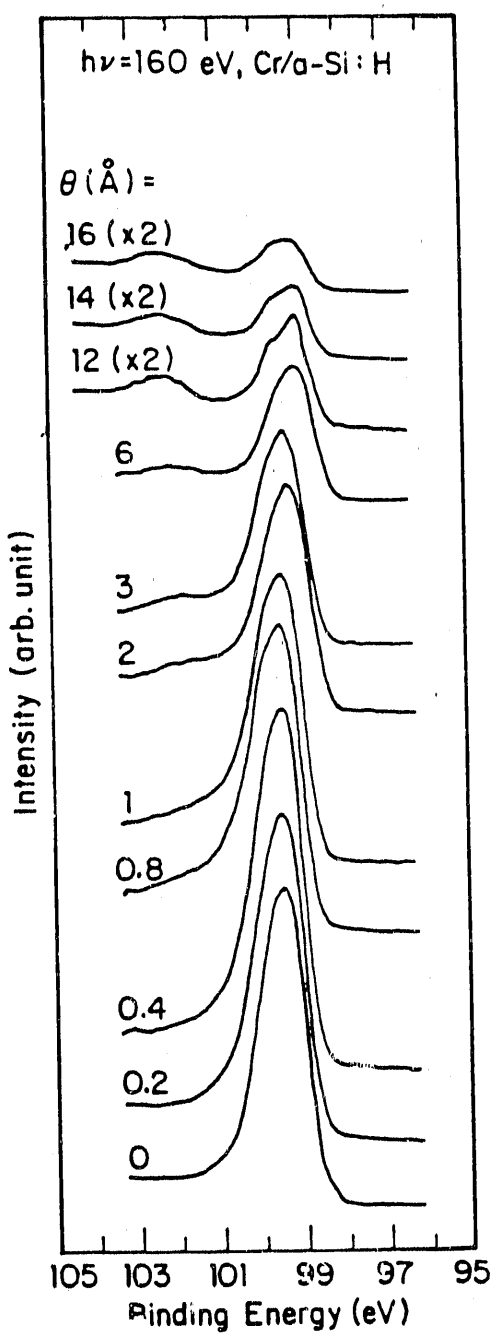

Fig. 23: Surface-sensitive core level EDCs taken at hν = 160 eV to monitor the emission from the Si 2*p* states

Å. As the Cr coverage increases, two peaks, initially located at 1.5 and 0.5 eV at the lowest coverage, move progressively toward E_F and are finally stable at 1.05 and 0.38 eV, respectively, above 2 Å. In the same coverage interval (from 0.2 Å to 2 Å), Figs. 22 and 23 show that the energies of the Cr 3*p* and Si 2*p* core levels remain unchanged. The binding energy of the Cr 3*p* line is 42.0 eV. There is less than 0.1 eV variation of the Si 2*p* lines with coverage, and that is mostly due to the intensity modulation of the Si 2*p* states in SiH_x ($0 \leq x \leq 3$) complexes. As a consequence, we do not regard the variation as due to band bending, in line with the valence band results.

The Cr 3*d* – Si 3*p* bonding and non-bonding structures with different silicide stoichiometries in the Cr/c-Si system have been studied, theoretically [107] and experimentally [107, 108]. Density-of-states calculations [107] infer that the bonding state in a Si-rich silicide has a higher binding energy than in a Cr-rich silicide. Experimental study of a definite silicide like $CrSi_2$ using photoemission reveals the binding energies of the bonding and non-bonding states to be 2.2 eV and 0.2 eV, respectively [108]. Different values have also been given, 1.7 and 0.3 eV, respectively [107]. Wetzel *et al.* further showed the bonding and non-bonding states for CrSi were 1.6 and 0.2 eV, respectively [108]. For a photoemission study of a Cr/c-Si interface formed by evaporation at room temperature, the binding energy of the bonding state shifted progressively toward the Fermi level with increasing coverage. The negative shift appeared only in a reacted Cr-Si region whose thickness was given as 10-15 ML by Franciosi *et al.* [107] and as 25 ML by Wetzel *et al.* [108].

Our room-temperature Cr/a-Si:H system shows a similar shift of states at 2 eV below E_F with increasing coverage (Fig. 20). We do not, however, regard it as an indication of change in stoichiometry or the existence of a

bonding state. Rather, we interpret it as a signature of increasing d orbital overlap. Concurrent with stoichiometry changes in the valence band, Si, as well as Cr, core levels should exhibit shifts, usually to lower binding energy [107, 108]. As seen in Figs. 22 and 23, the Si 2*p* and Cr 3*p* lines have no such shifts upon bonding changes, due neither to chemical reactions nor to an adjustment of the band edge. This leads us to believe that the shift of the valence states within 2 eV comes from increasing *d* orbital overlap [96] instead of stoichiometry changes along the surface normal. The line shape in Fig. 21 further supports our interpretation. For a Si-rich silicide, an EDC taken at a photon energy of 50 eV shows that the intensity of the non-bonding state is higher than that of the bonding state [112]. In Fig. 21, no such feature appears (our data at hν = 50 eV exhibit the same shape as in Fig. 21).

In addition to the development of the Cr 3*d* states, the emission from the Si-H states near 6.5 eV is still seen unambiguously (Fig. 21). Its persistence needs further comment. As one can see, the 6.5 eV emission from the substrate is at a photon energy where the cross section of the d orbitals is predominant. One might argue that the Cr 3*d* and Si-H bonding orbitals appear in different regions in the valence band, reducing the probability of their interfering destructively with each other. However, as shown in Fig. 21, the scaling factor for the spectra is reduced at low coverage (spectra were normalized with respect to 80 Å thickness). The 6.5 eV Si-H bonding state, even so, can be recognized easily without tuning the photon energy to depress the *d*-orbital emission, as in the case of Au or Ag deposits. Thus, the survival of the Si-H states at a photon energy with high *d*-orbital cross section suggests that the sites of the Cr atoms must be those with no Si–H complex in the neighborhood. In other words, they gather around the sites

where dangling bonds are dominant. This also suggests that Cr adatoms do not have a long range effect on the electronic states of the a-Si:H surfaces. The implication is even clearer as we increase coverage. The intensity of the Cr 3*d* states increases with increasing coverage. The intensity of the 6.5 eV peak, however, does not attenuate in proportion. Note that the 6.5 eV peak is seen only at a coverage less than 1 Å, which has a low average metal density on the surface.

The less hybridized Cr 3*d* – Si 3*p* feature in the low-coverage region in the Cr/a-Si:H system can be explained by the great difference in the density of dangling bonds of the c-Si and a-Si:H surfaces. Considering the Cr adatoms gathered only in the dangling bond neighborhoods at this low coverage, we obtain a higher *local* density of Cr adatoms in an a-Si:H surface than in a crystalline surface. In other words, those bonding sites are in a region of Cr enrichment, thereby giving the bonding state a lower binding energy.

Clustering and yet intermixing of Cr adatoms is conceivable in Fig. 24 as well, where the integrated Cr 3*p* intensity scaled to the intensity at 0.2 Å is shown. The inset emphasizes the reduced intensity, R.I. = I(θ)/I(0.2 Å), versus reduced coverage, R(θ) = θ/0.2 Å, at low exposures, with the solid line indicating non-intermixed, homogeneous growth on a smooth surface. It is evident from the figure that at low coverages, the Cr 3*p* intensity (dashed line) does not rise proportionally with coverage. The deviation can be understood as follows: In a submonolayer region, the intensity of an overlayer increases linearly with coverage, thereby giving a slope of unity in $Å^{-1}$ for the solid line in the inset of Fig. 24. However, if the overlayer is thick enough to form clusters, then the escape-depth effect needs to be considered. As a result, the slope of the solid line would be 0.28 $Å^{-1}$ if the geometric factor is included.

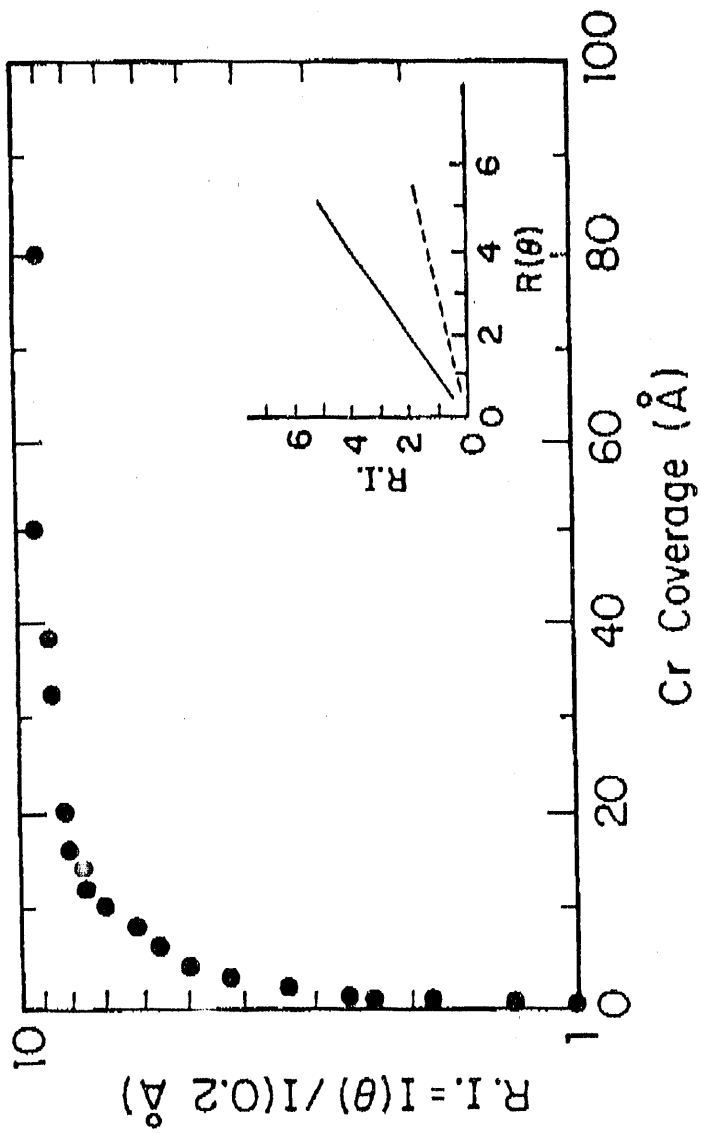

Fig. 24: Integrated intensity of the Cr 3p state normalized to the value at 80 Å as a function of coverage θ. Inset shows the reduced intensity, R. I. = I(θ)/ I(0.2 Å), versus reduced coverage, R(θ) = θ/0.2 Å, at low exposures. The dashed line connects the measued intensity, while the solid line indicates non-intermixed, homogeneous growth on a smooth surface (see text)

This value is consistent with the slope of the actual data (dashed) 0.27 $Å^{-1}$. Therefore, the impinging Cr atoms are clustered on the surface at coverage below 1 Å.

In conclusion, as illustrated by the valence band as well as core level spectra, at low coverage, Cr adatoms gather in the neighborhoods of dangling bonds, thereby giving a local Cr-rich environment. Strong bonding between the overlayer and the substrate does not occur. Further, the clusters are metallic.

Intermediate (≤ 12 Å) and High Coverages (≥ 12 Å)

At coverage above 2 Å, the Cr 3*d* states continue to give rise to strong transitions at 0.38 and 1.05 eV, as seen in Figs. 20 and 21. The 6.5 eV Si–H bonding state disappears in the valence band. In Fig. 21 ($h\nu$ = 55 eV), the line shape and positions of the Cr 3*d* band are essentially the same. Only the intensity increases with increasing coverage. Figure 20 ($h\nu$ = 21 eV), however, shows different behavior of the occupied *d* band. The main features consist of: (1) the bandwidth gradually broadens from 3.8 eV at 3 Å to 4.35 eV at 12 Å and stays constant thereafter; (2) the bonding and non-bonding states exhibit intensity modulations; (3) a peak at 3.07 eV starts to develop at 12 Å. In addition, both Figs. 20 and 21 show that a peak centered at 6 eV appears in the spectra.

As to core levels, Figs. 22 and 23 show displacements of both the Si 2*p* and Cr 3*p* lines. Referring to the bulk position of the Cr 3*p* line at the highest coverage (42.0 eV), we can see that it gradually shifts to lower binding energies at coverages above 2 Å, but moves back to the bulk energy above 12 Å. It is at 42.0 eV above 16 Å with no further change in position. The Si 2*p* line,

referred to the line position at the highest intensity at the zero coverage (99.6 eV), shifts to lower binding energy above 2 Å, but stays fixed at 99.0 eV afterwards. As indicated in Refs. 2 and 3, a shift to lower binding energy of the substrate Si 2*p* states normally occurs in an intermixed or silicide-like interface. Therefore, an intermixed or silicide-like Cr/a-Si:H layer may be present above 2 Å. Later, we will show other behavior that differentiates these.

Although the width of the Cr 3*d* states increases, it is still less than that of the calculated one-particle density-of-states [107]. A number of studies have shown that Coulomb correlation is important for the Cr 3*d* states, in Cr silicides as well as in crystalline Cr [15, 16]. Considering correlation effects in the calculation allows the bonding and non-bonding peaks to move toward E_F, and reduces the intensity of the bonding structure dramatically. A similar correlation effect is expected for the Cr/a-Si:H interface.

To better illustrate valence band feature (2), we show the peak-height intensities of the non-bonding (0.38 eV) and bonding (1.05 eV) states in Fig. 25. Points in Fig. 25 were taken at the corresponding peak height and then normalized to the value at 0.4 Å, respectively. Note that the bonding state is involved to a lesser extent than the case of c-Si. As shown in Fig. 25, the intensity of the bonding state increases linearly at low coverage and becomes nearly constant at high coverage. The intensity of the non-bonding state, on the other hand, evolves differently. It rises to a maximum at 12 Å and drops to saturation afterwards. The intensity evolution of the non-bonding state is quite different from the case of c-Si. In the Cr/c-Si interface, the intensity of the bonding state at $h\nu$ = 21 eV is always higher than that of the non-bonding state, and no turn-over in intensity of the non-bonding state like that in Fig.

25 has been reported [107]. Even though the bonding state emission is weaker in a definite silicide like $CrSi_2$, its binding energy is 0.5 eV higher than in the Cr/c-Si interface formed at room temperature. Therefore, based on the behavior of the valence band, we find that the criteria for silicide formation set by the Cr/c-Si interface are hardly applicable to the Cr/a-Si:H interface. Nevertheless, the interface is an intermixed one but to a lesser degree, a statement reinforced by core-level behavior. In addition, if a Cr $3d$ – Si $3p$ bonding state were formed, then the hybrid would have a higher binding energy than either of the states [113]. As shown in Fig. 20, the supposed bonding state is located at 1.05 eV, starting from 2 Å until bulk Cr forms. As discussed below, we attribute the 6 eV structure to oxygen.

Switendick [114] has made a density-of-states calculation for a hexagonal CrH. It showed that excess electrons from hydrogen would be added to the system, moving the Fermi level upward and subsequently lower the density of states at E_F. Moreover, a hydrogen-induced feature would occur 6 ~ 7 eV below the Fermi level. In our system, a CrH compound is possibly formed. Although a new feature at about 6 eV appears, the behavior at E_F does not match the calculated prediction, so we can not confirm that a hexagonal CrH phase is formed in the Cr/a-Si:H interface.

In Fig. 23, at 2 Å thickness, a weak hump appears on the high binding energy side of the substrate Si $2p$ line, 2.7 eV higher. The chemical shift becomes even larger with increasing coverage. However the separation, due partially to a shift of the hump itself to higher binding energy and partially to the displacement of the substrate Si $2p$ line to lower binding energy, becomes constant at 3.2 eV above 12 Å. The intensity of the chemically-shifted peak increases with increasing coverage until the development of bulk Cr. Along

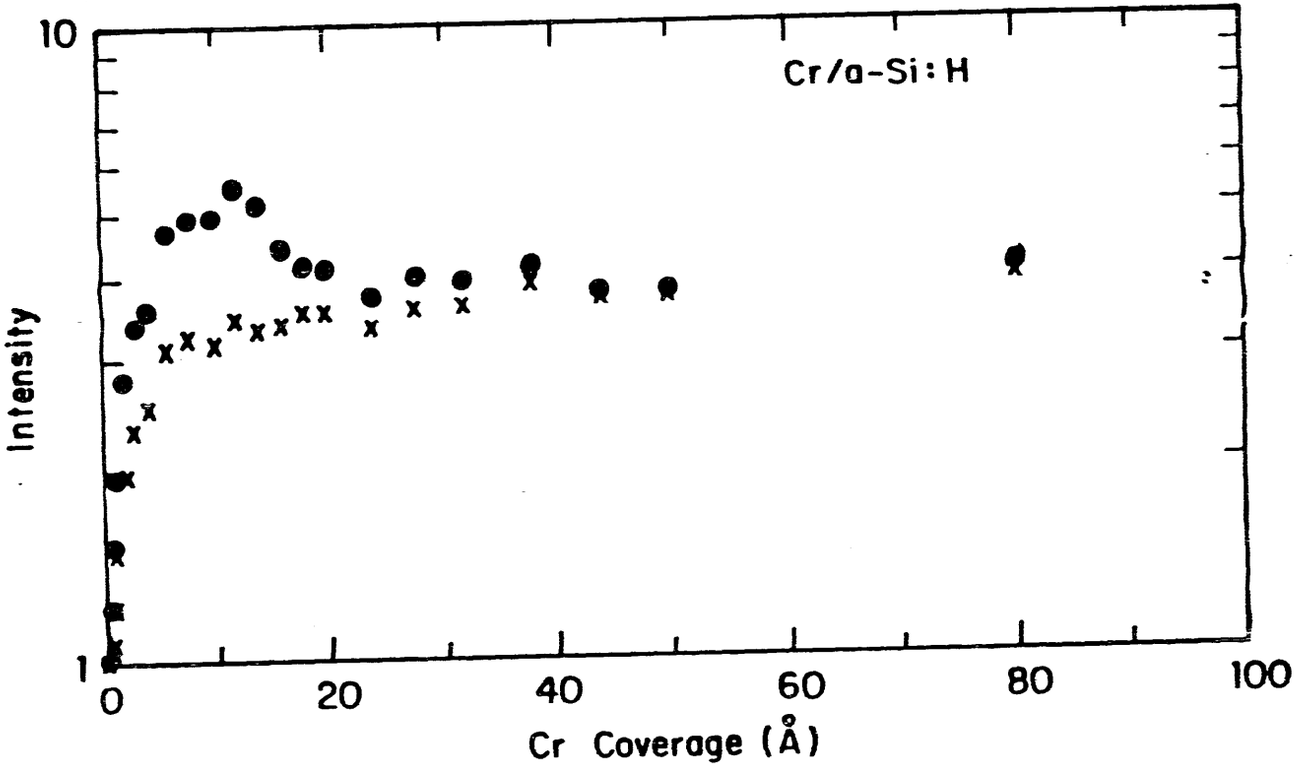

Fig. 25: Intensity evolutions of the 0.38 eV and 1.05 eV peaks in the valence band. Data are taken from Fig. 20 (see text). Note that a maximum intensity occurs at 12 Å for the 0.38 eV peak.

with the presence of the chemically-shifted peak in the neighborhood of the Si 2*p* core levels, valence band emission (Figs. 20 and 21) shows a 4-eV wide feature centered at about 6 eV below E_F. Its intensity evolved similarly to the chemically shifted Si 2*p* peak, increasing with increasing coverage, suggesting that it might be caused by Cr itself or by the Cr/Si interface.

The presence of the chemically shifted Si 2*p* structure is somewhat surprising. According to the magnitude of the shift, it is possibly an oxide-driven feature. However, as shown in the valence band, as well as core level, spectra, no oxygen effects appear at low coverages. Furthermore, the energy positions induced by the oxygen do not correspond to those found in the study of the oxidation of Cr [115] and c-Si [116] and Cr/c-Si [117], or a-SiO_x:H [111]. Nevertheless, other evidence (see below) suggests that it really is oxygen induced. Excluding the Cr evaporator as its origin (pressure always below 8.5 x 10^{-11} Torr), we speculate that the oxygen residual was incorporated during a-Si sample preparation in the rf sputtering chamber. In an abrasion study, Ballutaud *et al.* [118] have illustrated that a hydrogenated silicon sample made by rf sputtering shows traces of oxygen after 500 Å of the film has been milled away by argon bombardment. Moreover, they found that the oxygen does not induce any chemical or substrate shift of the Si 2*p* core levels. Similar features are also observed empirically in our study. We intermittently measured the emission from the oxygen K edge and found a proportional increase in intensity with increasing chemical-shift intensity. This gives further evidence that the chemically-shifted peak is due to Si atoms reacting with oxygen which are from the substrate itself.

Franciosi *et al.* [109] have illustrated that the oxidation rate increases in the Cr/c-Si interface after a critical Cr thickness. Wetzel *et al.* [108] have

further found that oxygen uptake for a Cr/c-Si interface formed at 300 K is at least tenfold greater than for stoichiometric silicides. The intermixed Cr/Si layer has been claimed responsible for the increased oxidation [108, 109]. In the Cr/a-Si:H system, we obtain an unreacted thickness at 1 Å of deposition. Above that, the interface has become an intermixed one. Therefore, referring to the Cr/c-Si study, we suggest that the residual oxygen undergoes a reaction provoked by the intermixed Cr/a-Si:H interface to form amorphous silicon oxide, a-SiO_x, where x is less than 1 [119]. The more intermixed product, the higher the emission of the oxidized state.

A 6 eV peak has also appeared on Cr metal itself [120] and $CrSi_2$ [107]. However, its origin has been controversial. For $CrSi_2$, Weaver *et al.* [107] have attributed it to a Si *p* state. For Cr metal, some groups [120] have discussed it as a valence band satellite, while another [121] has proven that it is due to oxygen 2*p* states. The explanation is hindered by the fact that the 6 eV peak in Cr metal shows resonant behavior near the photon energy of the $3p - 3d$ threshold transition energy and a correlation effect takes place in the *d* band. However, as indicated in the work of Raaen and Murgai [121], the 6 eV peak is absent in a polycrystalline Cr film. With the clean surface exposed to oxygen, the 6 eV peak starts to appear. They have further shown that the oxidized surface resonates when photon energy sweeps through the Cr $3p - 3d$ transition, identical to other reports [120]. We have observed a similar resonant-like enhancement of the 6 eV peak at low (6 Å) and high (120 Å) Cr coverages. Therefore, with the heritage of the residual oxygen in our system and with assistance of the study in Ref. 121, we can assign the 6 eV peak to an oxygen-induced structure. Further, carefully examining the evolution of the valence band, we find that the presence of the 6 eV peak does

not inhibit the emission of the Cr 3*d* states. In other words, the oxygen does not bond strongly with the Cr overlayer to give rise to Cr_2O_3. Otherwise, the emission near the Fermi level would attenuate drastically [115].

In summary, the 6 eV peak in the valence band and the chemical shift of the Si 2*p* line are due to oxygen. The 6 eV peak also appears in the Sm/a-Si:H interface after a certain thickness [122].

The intermixing effect exhibited in the Cr/a-Si:H system is certainly not found in our study on the Au/a-Si:H system. In the latter, the interface also became intermixed above 2 Å of Au deposition. However, no oxygen-induced features like the 6 eV peak in the valence band or the chemically-shifted peak in the core level spectra appeared in that study. This clearly indicates that the intermixed Cr/Si species are more unstable.

After the intermixed overlayer, bulk Cr starts to develop after 12 Å of Cr deposition. The evidence is: (1) the intensity of the non-bonding state begins to fall from a maximum at 12 Å; (2) a feature at 3.07 eV in the valence band starts to develop at 12 Å; (3) the band width of the Cr 3*d* states does not increase above 12 Å; (4) the intensity of the Cr 3*p* state stays nearly constant above 12 Å (Fig. 24). Despite the development of bulk Cr, silicon atoms can still be detected. At 80 Å of Cr coverage, there are slight traces of silicon atoms. Silicon at this coverage can be thought of as atoms that diffuse through the interface. Interface-controlled diffusion occurs in the case of c-Si as well [108].

Ag ON a-Si:H

Introduction to Ag on c-Si

The growth of Ag on c-Si at room temperature has been understood to proceed the Stranski-Krastanov mode; that is, a layer-by-layer growth followed by island formation [68]. However, the detailed structure of the silver overlayer, at low coverage, depends on the surface structure of c-Si. On a cleaved Si(111)2×1 surface, an ordered $(\sqrt{7} \times \sqrt{7})$–R19.1° silver overlayer is superimposed on, but does not disrupt, the underlying ordered structure. On the other hand, the 7×7 ordered pattern is lost when silver adatoms are deposited on a Si(111)7×7 surface. For Si(100), both Ag(100) and Ag(111) ordered overlayers were reported to grow in an orientation parallel to the (100) direction [68]. Moreover, if heat is appplied to a Ag/Si(111)7×7 interface then an ordered $(\sqrt{3} \times \sqrt{3})$–R30° silver surface will be formed [68, 122]. This particular structure has been the subject of numerous studies in recent years.

Judging from the evolution of the intensity of the Si $L_{2,3}VV$ transition, Hanbücken and Ley found that the intensity attenuated more rapidly on a (100) surface than on a (111) surface. Nonetheless, the interaction between Ag and Si is rather weak and the interface, unlike the Au/c-Si system, is abrupt without intermixing. The abruptness, or lack thereof, has been questioned by Rossi *et al.* [123], who observed an energy shift of Si 3*s* states toward E_F with increasing Ag coverage. They interpreted the shift as due to breaking the Si $3sp^3$ configuration and setting free the silicon atoms to intermix with silver. However, a redistribution of valence states is not neccessary to lead to silicide formation. The energy shift is rather

interpreted as due to chemisorption, which is more appropriate in compliance with results from other techniques [1].

Results and Discussion

Figures 26 and 27 shows valence band emission taken at photon energies of 80 eV and 130 eV, respectively. The latter utilized the Cooper minimum effect, suppressing the cross section of the Ag 4*d* orbitals, in order to manifest the emission from a-Si:H substrate. The results of Fig. 26 show that for the lowest Ag coverage of 0.5 Å, the 4*d* spin-orbit splitting, and the centroid of the 4*d* states are 0.95 eV and 5.82 eV, respectively. They become 1.31 eV and 5.36 eV, respectively, at 2 Å. The band widths (full width at half maximum) are 2.0 eV and 2.91 eV for 0.5 Å and 2 Å, respectively. These values, lower than those of pure Ag, are indicative of dispersed adatoms, mainly due to low coordination number. Other features in Fig. 26 are the intensity of the Ag 4*d* band increasing with increasing Ag coverage and a Fermi level that starts to show at θ = 3 Å. From θ = 3 Å and above, the line shape and positions are not very far from those of bulk Ag.

At the Cooper minimum (Fig. 27), emission from the a-Si:H substrate is clearly seen. As shown, the position of the VBM and the binding energies of the bonding states of the Si 3*p*, Si 3*p* – H 1*s*, and Si 3*s* – H 1*s* orbitals, at θ = 0 Å, are 0.6, 3, 7, and 9.5 eV, respectively. The binding energy of the Si 3*s* – H 1*s* state is lower than that of the state shown in the case of the Au deposit, because of a lower hydrogen content due to the Ar^+ etching cleaning process [85]. Upon Ag deposition, the VBM shifts gradually toward the Fermi level with increasing coverages. The negative shift of the VBM indicates that bands at the surface of a-Si:H film are bent upward, in agreement with a

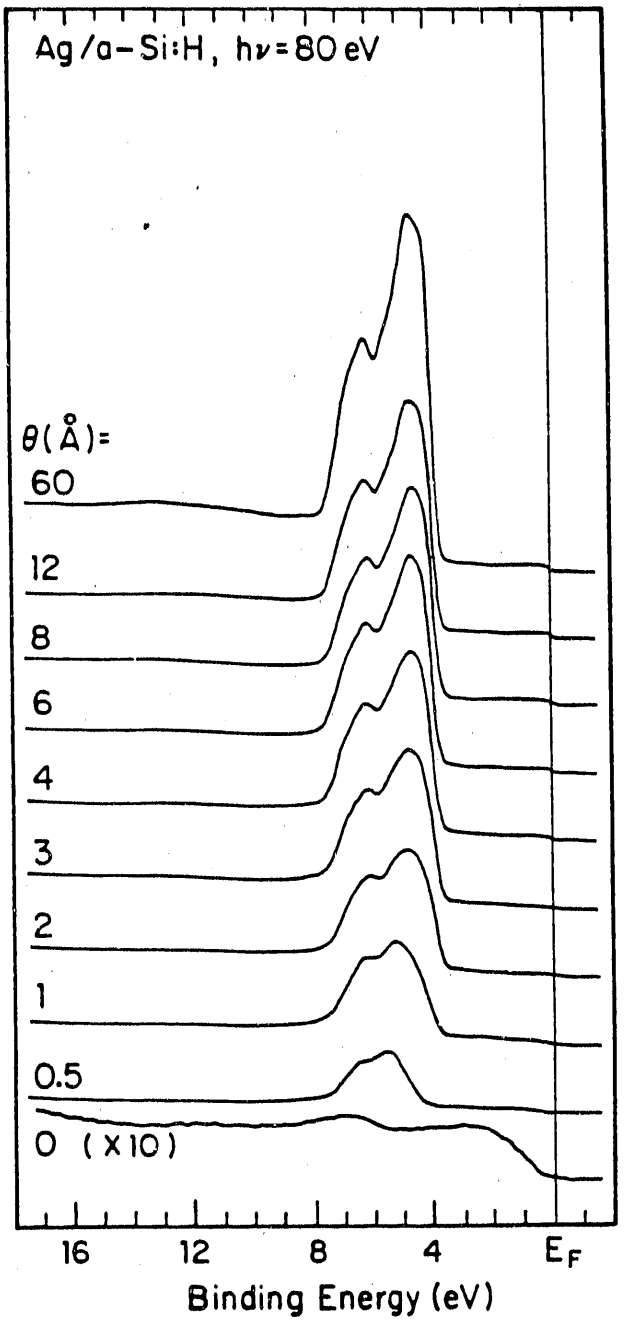

Fig. 26: Valence band emission taken at hν = 80 eV. All spectra are normalized to photon flux and then adjusted to the same magnitude

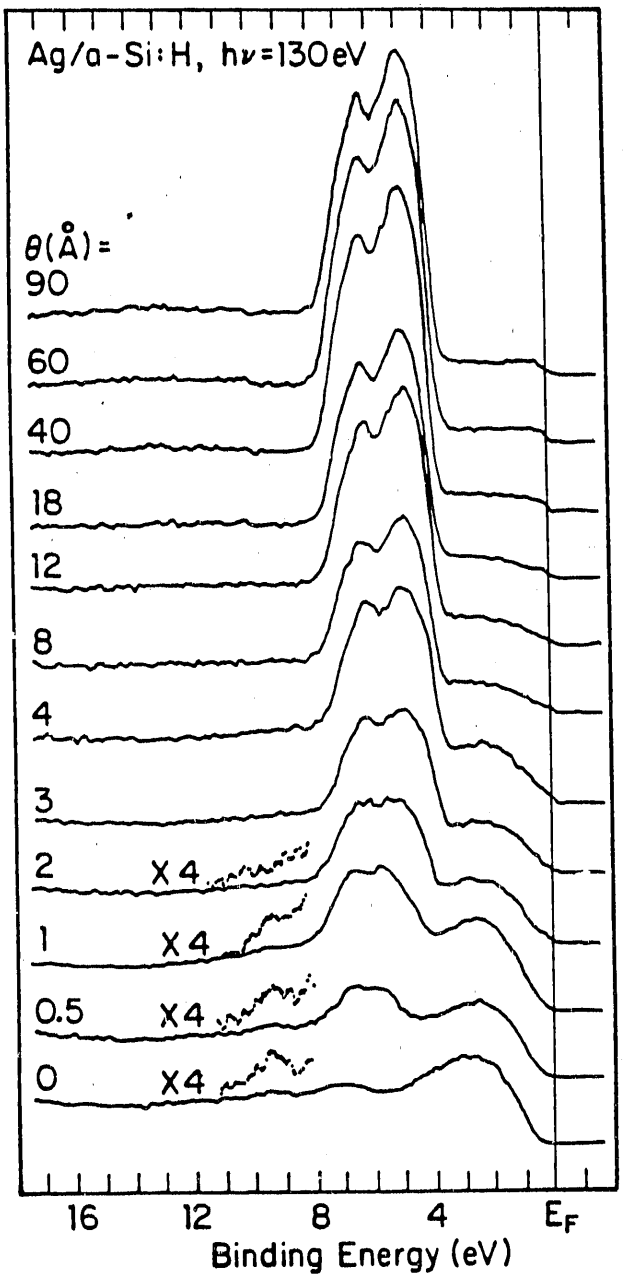

Fig. 27: Valence band emission taken at hν = 130 eV. Normalization scheme is the same as in Fig. 26. The bonding states due to Si 3*s* and H 1*s* orbitals are visible at coverages below 1 Å

conclusion in the Au/a-Si:H interface. Furthermore, as prominent for the Au deposit as for the Ag deposit, the Si 3*s* – H 1*s* state is visible and unshifted of energy at coverages below 1 Å. This means that Ag adatoms, at low coverages, prefer to gather in regions devoid of hydrogen.

Figure 28, taken at hν = 160 eV, shows a core-level emission from the Si 2*p* states. The spectra represent surface a-Si atoms because of the short mean free path (~ 5 Å) of electrons with ~ 55 eV kinetic energy. From a curve-fitting routine [124], the binding energy of a-SiH_0, the Si atoms not bonded with H, is 99.45 eV at 0 Å. It shifts to 99.35 eV at 0.5 Å and to 99.23 eV at 1 Å. The negative shift of the Si 2*p* core level reinforces the conclusion that bands at the surface of a-Si:H are bent upward. Further, hydrogen concentration can also be determined from the result of a fit by taking the ratio of the summed intensity of Si atoms that bond with hydrogen, and the total intensity of Si atoms that bond and unbond with hydrogen [85]. The result then gives 10 at. % of hydrogen. This is lower than the film used for the Au study, which has 15 at. % of hydrogen.

At coverage above 1 Å, the inclusion of hydrogen into the model function did not give a good fit; χ^2 did not converge. Since silicon charge transfer to hydrogen gives the Si 2*p* states a shift of about 0.34 ± 0.1 eV to higher binding energy [85], the exclusion of it from the model function is consistent with a valence band result that the Si 3*s* – H 1*s* state is absent at θ = 2 Å and above. This suggests that the charge distribution of Si atoms at the surface is disturbed by the Ag overlayer. Nonetheless, the interaction between the silver overlayer and a-Si:H substrate is weak and no intermixing occurs. These are realized by observing Fig. 28 that the Si 2*p* states have no dramatic changes of line shape as the Ag coverage is increased. Weak

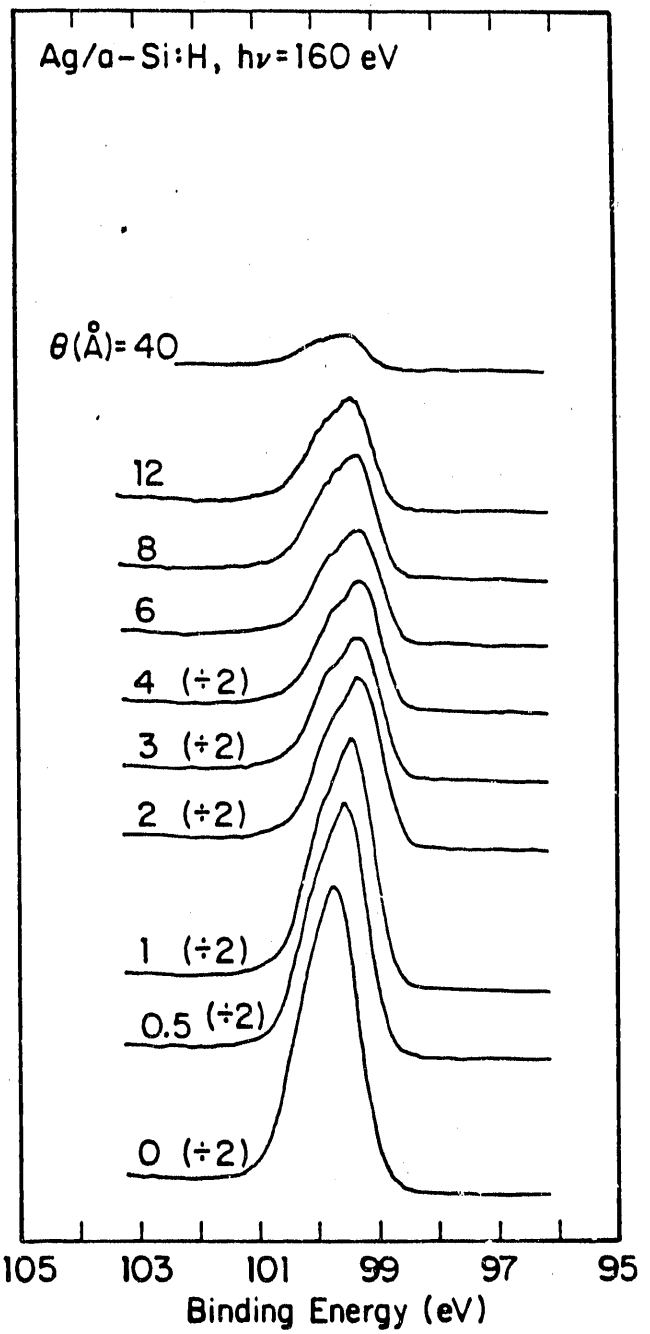

Fig. 28: Surface-sensitive core level EDCs taken at hν = 160 eV to monitor the emission from the Si 2*p* states

interaction also occurs in the Ag/c-Si interface.

To further delineate the non-intermixing, we plot the total integrated intensity of the Si 2*p* states (scaled to the value at θ = 0 Å) against coverage for the Ag overlayer in Fig. 29a and the Au overlayer in Fig. 29b. The figure clearly shows that the intensity of the Si 2*p* states attenuates faster in the Ag overlayer than in the Au overlayer. Further, unlike Si in an Au environment where silicon diffusion through the gold overlayer is apparent, silicon atoms do not diffuse through the silver overlayer. Particularly, no Si 2*p* signal is perceivable at coverages above 65 Å. This clearly indicates that Ag atoms do not intermix with a-Si:H.

Unlike the Cr/a-Si:H system, the Ag/a-Si:H system shows no oxygen induced feature on the high binding-energy side of the Si 2*p* core level spectra. Rossi *et al.* [125] reported an enhancement of silicon reactivity to oxygen as one monolayer of silver was deposited onto a Si(111) surface. They asserted the oxidation enhancement to the broken Si sp^3 configuration by Ag adatoms. With just the oxygen incorporated in a-Si:H film, such enhancement is not seen in our study.

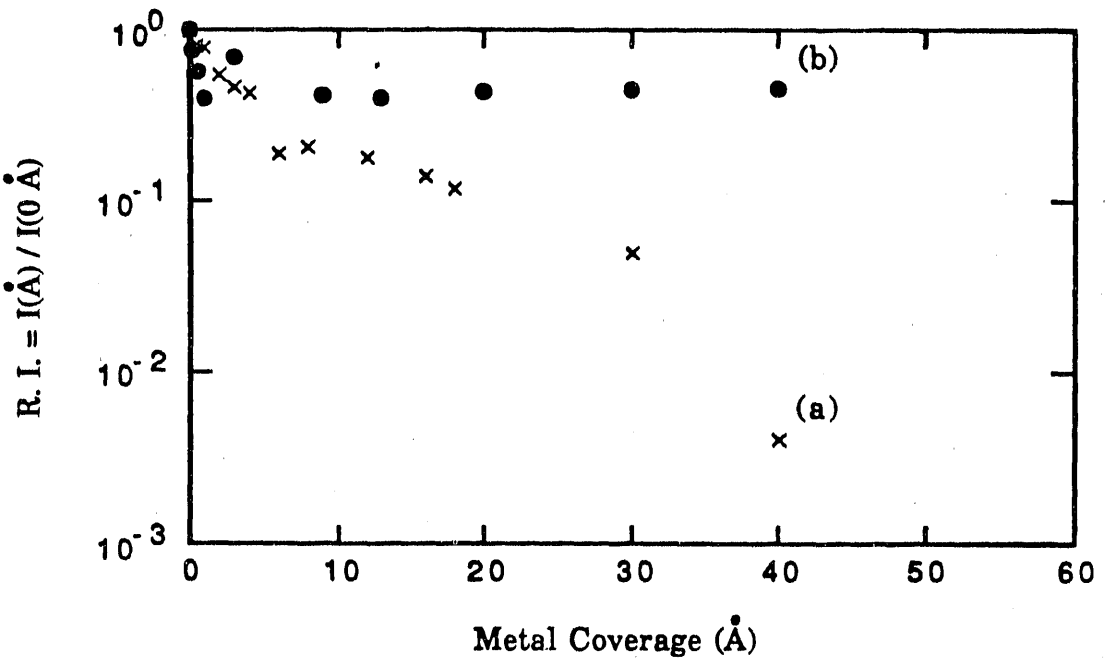

Fig. 29: Integrated intensity of the Si 2*p* states *vs* (a) Ag and (b) Au coverages. Data were normalized to the value at 0 Å

CONCLUSIONS

Au on a-Si:H

Three regions are identifiable in the Au/a-Si:H interface. From the outset of gold deposition, a band-bending region, at a coverage below 1 Å, exhibits no strong interactions between the deposit and the substrate. This appears as a monotonic shift of the Si 2*p* core level to higher kinetic energy without a change in line shape, as well as a continuous decrease in intensity. As coverage increases from 1 to 9 Å, a simple-intermixing region appears. In this region, Si atoms not bonded to H leave the substrate and intermix with the gold thin film. Continued deposition leads us to the final region, the dual-phase region. The noticeable features in this region are development of a 2.67 eV peak in the valence band, well-resolved silicon 2*p* spin-orbit core levels, and two sets of Au 4*f* core levels with one set associated closely with Si, the other exhibiting the character of pure gold. The observation of a silicon signal and a shifted Au signal is understood by a high diffusion rate of Si through the Au film, giving rise to a surface layer of Si in Au. Instead of the sequence of Si(sub.)–$(Au/Si)_1$–(pure Au)–$(Au/Si)_2$–(vac.) at the Au/c-Si interface, the Au/-Si:H interface exhibits a-Si:H(sub.)–(Au/a-Si+pure Au)–(vac.). Namely, a pure Au layer is not found in the Au/a-Si:H interface. The intermixed overlayer persists, once an unreacted thickness is exceeded. Whether or not Au forms a silicide with a-Si:H in the intermixed region is still unclear at this moment. This is also an unresolved point in the case of Au on c-Si.

Cr on a-Si:H

At coverages below 1 Å, the interface is inert. But the surface has become metallic at as little as 0.2 Å effective thickness. Moreover, Cr adatoms cluster in the vicinity of the Si that is not bonded with hydrogen. Above 2 Å, the Cr overlayer begins to intermix with the a-Si:H substrate, but to a lesser degree than the crystalline counterpart. No definite silicides can be identified in this region. This statement is reinforced by the study of Nava, Tien, and Tu [126] who showed that the $CrSi_2$ film is a semiconductor. Because of the inevitable incorporation of oxygen in the a-Si:H substrate in the hydrogen plasma, the intermixed Cr/Si layer serves as a catalyst to increase the rate of the interaction between the residual oxygen and elemental silicon. The residual oxygen initially does not have a chemical effect on the substrate. The thickness of the intermixed layer is about 12 Å. Above that, a bulk-like Cr feature develops. A slight trace of silicon atoms is still found at a thickness of 80 Å.

Ag on a-Si:H

The a-Si:H film for the Ag overlayer was determined to have 10 at. % hydrogen concentration, by a curve-fitting routine to a surface Si 2*p* core level. This hydrogen content is lower than the films for the Au and Cr overlayers, which had 15 at. % of hydrogen. The relatively lower H content makes the position of the VBM further from the Fermi level, and a lower binding energy of the Si 3*s* – H 1*s* bonding state.

In general, the Ag and a-Si:H interface is abrupt without intermixing. However, a subtle change can be seen at a coverage of 1 Å. Below that, silver atoms are likely to distribute at regions that are Si-H-bond free. Further,

bands at the surface bend upward, similar to the Au/c-Si:H interface. Above 1 Å, no Si-H bonding states are found either in the valence-band or the core-level spectra.

The persistence of Si-H bonding states, at low metal coverages, is one of the features uniquely observed in the metal/a-Si:H interfaces. Figure 30 shows valence band spectra, emphasizing low metal coverages. As shown, the persistence of the Si-H bonding states is striking. This strongly suggests that the metal deposits, at low coverages, are likely to distribute on surface regions devoid of hydrogen. Surface roughness [127] increases the densities of valleys, steps, kinks, or microvoids. Those are the regions that are likely to attract diffused adatoms. If dangling bonds in these regions were satisfied by passivated hydrogen, then the emission of the Si-H bonding states would attenuate in proportion to increasing adatom coverage. On the contrary, the intensity of the Si-H bonding states persists until a reaction between the overlayer and the substrate occurs.

Furthermore, it is noteworthy that because of the intrinsic properties of the a-Si:H sample, such as an aging effect [128] and the phenomenon of H atoms diffusing from the bulk [87], we found the intensities of the 6 eV peak and of the chemically shifted Si 2*p* line increased overnight at a fixed Cr thickness. Changes overnight occurred to the Au/a-Si:H system as well, which shows quantitative differences of the interface built by processes of one or several accumulated depositions to a given thickness. To obtain the same line shapes in the valence band or the core level spectra from these two processes requires less thickness for the single-deposition mode than for the accumulated-deposition mode.

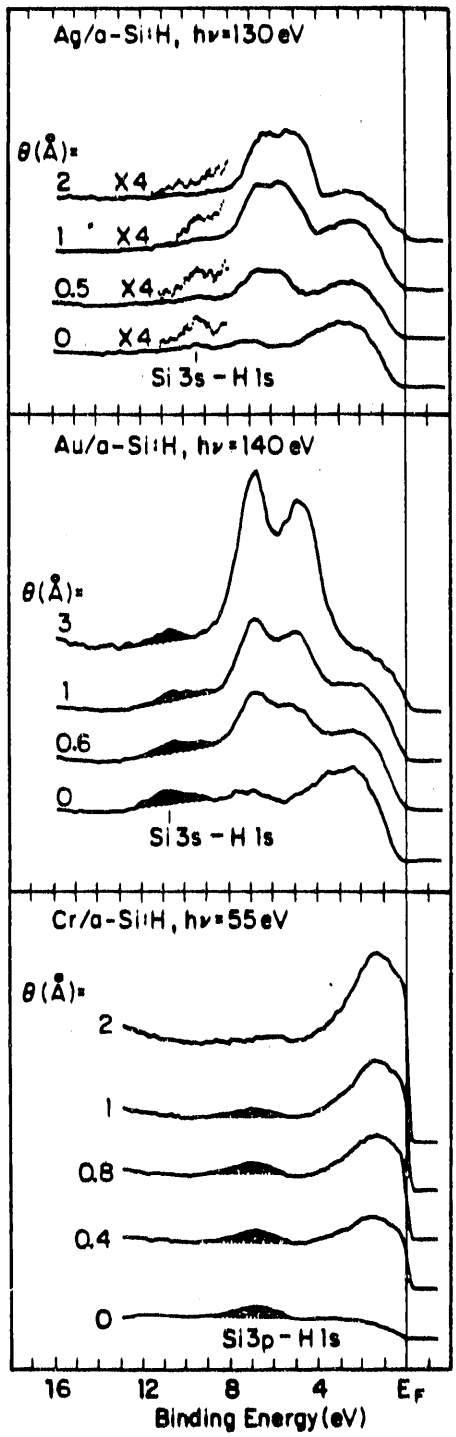

Fig. 30: Valence band emission at low metal coverage. Note the persistence of the Si-H bonding states

As distinct for the Au 4*f* core level as for the Ag 3*d* core level, there is a time-dependent shift as the 3*d* level, at a given thickness, was measured overnight. For example, at a thickness of 3 Å, the 3*d* lines shifted 0.25 eV toward higher binding energy on a sample which sat *in situ* 13 hours. This shift was not due to a measurement uncertainty, but to an intrinsic property of the metal/Si interface. A similar time-dependent shift was also observed on the Si(111)–($\sqrt{3} \times \sqrt{3}$)R30°–Ag surface [129]. According to Ref. 129, a surface state in the Si(111)–($\sqrt{3} \times \sqrt{3}$)R30°–Ag surface was observed at a binding energy of 0.1 eV below E_F when the surface was fresh, but shifted to 0.4 eV below E_F after 18 hours. Therefore, we can say that although silver atoms are able to stabilize the amorphous substrate from outdiffusion, they do not relax the surface fully.

BIBLIOGRAPHY

[1] See a recent review of L. Braicovich in The Chemical Physics of Solid Surfaces and Heterogeneous Catalysis: Vol. 5, Surface Properties of Electronic Materials, ed. by D. A. King and D. P. Woodruff (Elsevier, North-Holland, 1988) and references therein.

[2] The vacuum level is conventionally defined as the energy of an electron at rest at infinity. Some people define the vacuum level in terms of the energy of an electron far enough outside the surface of a sample for the image potential to be considered zero. Caution is required for the latter usage because of the surface dipole layer.

[3] T. A. Koopmans, Physica, 1, 104 (1933).

[4] D. A. Shirley, in Photoemission in Solids I, ed. M. Cardona and L. Ley (Springer-Verlag, Berlin, 1978).

[5] Inelastic mean free path (IMFP), escape depth, and attenuation depth have been used interchangably. To resolve the confusion, the committee E-42 on Surface Analysis of the American Society for Testing and Materials (ASTM) has settled definitions, particularly for IMFP and escape depth. Attenuation depth is under discussion. By definition, IMFP is the average distance that an electron with a given energy travels between successive inelastic scattering events. Escape depth is the distance normal to the surface at which the escape probability of an electron without significant energy loss due to inelastic scattering processes drops to e^{-1} (36.8%) of its original value.

[6] J. W. Gadzuk, in Photoemission and the Electronic Properties of Surfaces, ed. by B. Feuerbacher, B. Fitton, and R. F. Willis (Wiley, Chichester, 1978).

[7] D. Coster and R. de L. Kronig, Physica 2, 13 (1935).

[8] P. H. Citrin, P. Eisenberger, and D. R. Hamann, Phy. Rev. Lett. 33, 965 (1974).

[9] See, for example, M. H. L. Pryce, in Phonons in Perfect Lattices with Point Imperfections, ed. by R. W. H. Stevenson (Oliver and Boyd, Edinburgh, Scotland, 1966), p.403; J. J. Markham, Rev. Mod. Phys. 31, 956 (1959).

[10] P. W. Anderson, Phys. Rev. Lett. 18, 1049 (1967); Phys. Rev. 164, 352 (1968).

[11] J. J. Hopfield, Commun. Solid State Phys. 2, 40 (1969).

[12] A. Kotani and Y. Toyozawa, J. Phys. Soc. Jpn 35, 1073 (1973); 37, 912 (1974).

[13] C. N. Berglund and W. E. Spicer, Phys. Rev. 136, A1030 (1964); 136, A1044 (1964).

[14] L. Ley and M. Cardona (eds.), Photoemission in Solids II, (Springer-Verlag, Berlin, 1979).

[15] C. Caroli, B. Roulet, and D. Saint-James in Handbook of Surfaces and Interfaces, Vol. 1, ed. L. Dobrzynski (Garland, New York, 1978).

[16] I. Adawi, Phys. Rev. 134, A788 (1964). G. D. Mahan, Phys. Rev. B 2, 4334 (1970).

[17] I. W. Schaich and N. W. Ashcroft, Solid State Comm. 8, 1959 (1970); Phys. Rev. B 3, 2452 (1971).

[18] P. J. Feibelman and D. E. Eastman, Phys. Rev. B 10, 4932 (1974).

[19] J. Schwinger, Phys. Rev. 75, 1912 (1949).

[20] R. P. Godwin, in Springer Tr. s in Modern Physics, Vol. 51 (Springer-Verlag, 1969) and references therein.

[21] H. Winick and S. Doniach (eds.), Synchrotron Radiation Research, (Plenum Press, New York, 1980).

[22] A. A. Sokolov and I. M. Ternov, Synchrotron Radiation, (Pergamon Press, London, 1968).

[23] C. G. Olson, Nucl. Intrum. Methods, A 266, 205 (1988).

[24] M. Seya, Sci. Light 2, 8 (1952); T. Namioka, *ibid* 3, 15 (1954).

[25] F. C. Brown, R. Z. Bachrach, and N. Lien, Nucl. Instru. Methods 152, 73 (1978).

[26] C. S. Fadley, in Electron Spectroscopy, Theory, Techniques, and Applications, Vol. 2, ed. C. R. Brundle and A. D. Baker (Academic Press, London, 1978).

[27] At a surface $\nabla \cdot \vec{A}$ is usually not zero and may not be small compared to $\vec{A} \cdot \vec{P}$. See, for example, P. J. Feibelman, Phys. Rev. Lett. 34, 1092 (1975); Phys. Rev. B 12, 1319 (1975). K. L. Kliewer and R. Fuchs, Phys. Rev. 172, 607 (1968).

[28] S. M. Goldberg, C. S. Fadley, and S. Kono, J. El. Spectra. Rel. Phen. 21, 285 (1981). N. J. Shevchik and D. Leibowitz, Phys. Rev. B 18, 1618 (1978).

[29] Each form has its unique usefulness, see Ref. 4.

[30] J. J. Yeh and I. Lindau, At. Data Nucl. Data Tables 32, 1 (1985).

[31] J. W. Cooper, Phys. Rev. 128, 681 (1962).

[32] W. Gudat and C. Kunz, Phys. Rev. Lett. 29, 169 (1972).

[33] D. E. Eastman and J. L. Freeouf, Phys. Rev. Lett. 33, 1601 (1974).

[34] G. J. Lapeyre and J. Anderson, Phys. Rev. Lett. 35, 117 (1975).

[35] G. J. Lapeyre, J. Anderson, P. L. Gobby, and J. A. Knapp, Phys. Rev. Lett. 33, 1290 (1974); G. J. Lapeyre, A. D. Baer, J. Anderson, J. C. Hermanson, J. A. Knapp, and P. L Gobby. Solid State Comm. 15, 1601 (1974).

[36] See, for example, Giant Resonances in Atoms, Molecules, and Solids, ed. J. P. Connerade, J. M. Esteva, and R. C. Karnatak (Plenum Press, New York, 1986).

[37] There are two types of metal-semiconductor contact: (1) Non-ohmic contacts, Schottky type, do not allow easy flow of electrons from the metal to the semiconductor to balance space charge in the semiconductor; (2) Ohmic contacts allow a ready flow of electrons. Schottky barriers can form on either metals of larger work function contacted with an n-type semiconductor or of smaller work function with a p-type semiconductor.

[38] Suppose 10^{14} electrons per square centimeter of surface are transferred. If the volume conduction electron density is 10^{18} cm^{-3}, electrons will be depleted from the semiconductor to a depth of 10^{-4} cm.

[39] W. E. Spear, P. G. Le Comber, and A. J. Snell, Phil. Mag. B 38, 303 (1978).

[40] R. A. Street, J. Non-Cryst. Solids, 77&78, 1 (1985).

[41] M. Stutzmann, Phil. Mag. B 60, 531 (1989).

[42] R. J. Loveland, W. E. Spear, and A. Al-Sharbaty, J. Non-Cryst. Solids 13, 55 (1973).

[43] P. J. Zanzucchi, C. R. Wronski, and D. E. Carlson, J. Appl. Phys. 48, 5227 (1977).

[44] D. E. Carlson and C. R. Wronski, Appl. Phys. Lett. 28, 671 (1976).

[45] S. Veprek, F. -A. Sarrott, S. Rambert, and E. Taglauer, J. Vac. Sci. Technol. A 7, 2614 (1989).

[46] C. M. Garner, I. Lindau, C. Y. Su, P. Pianetta, J. N. Miller, and W. E. Spicer, Phys. Rev. Lett. 40, 403 (1978).

[47] N. Kasupke and M. Henzler, Surf. Sci, 92, 407 (1980); J. K. Gimzewski and S. Veprek, Solid State Comm. 47, 747 (1983).

[48] D. Adler, in Semiconductors and Semimetals, Vol. 21A, Chap. 14 (Academic Press, 1984).

[49] G. Lucovsky, R. J. Nemanich, and J. C. Knights, Phys. Rev. B 19, 2064 (1979).

[50] A. Madan and M. P. Shaw (eds.) in The Physics and Applications of Amorphous Semiconductors, Chap. 2 (Academic Press, 1988).

[51] H. Fritzsche, Thin Solid Films 90, 119 (1982).

[52] T. A. Postol, C. M. Falco, R. T. Kampwirth, I. K. Schuller, and W. B. Yelon, Phys. Rev. Lett. 45, 648 (1980).

[53] H. Fritzsche, in Semiconductors and Semimetals, Vol. 21C, Chap. 9 (Academic Press, 1984) and references therein.

[54] N. Maley, L. J. Pilione, S. T. Kshirsagar, and J. S. Lannin, Physica, 118B, 880 (1983).

[55] B. L. Henke, Phys. Rev. A 6, 94 (1972).

[56] A flooded source is defined as one in which the photon image on the sample is greater than the photoelectron sampling diameter without the retarding grids.

[57] P. W. Palmberg, J. Vac. Sci. Technol. 12, 379 (1975).

[58] H. G. Nöller, H. D. Polaschegg, and H. Schillalies, J. El. Spectr. Rel. Phen. 5, 705 (1974).

[59] C. G. Olson, private communication.

[60] J. W. Cooper and S. T. Manson, Phys. Rev. 177, 157 (1969).

[61] S. M. Goldberg, C. S. Fadley, and S. Kono, J. El. Spectr. Rel. Phen. 21, 285 (1981).

[62] K. Tanaka and A. Matsuda, Mat. Sci. Rep. 2, 139 (1987). J. Stuke, Ann. Rev. Mater. Sci. 15, 79 (1985) and references therein.

[63] Z. H. Lu, E. Sacher and A. Yelon, Phil. Mag. B 58, 385 (1988).

[64] Y. Mishima and T. Yagishita, J. Appl. Phys. 64, 3972 (1988).

[65] D. A. Shirley, Phys. Rev. B 5, 4709 (1972); G. Aeppli, D. E. Eastman, R. W. Johnson, R. A. Pollak, and H. J. Stolz, J. El. Spect. Rel. Phen. 14, 121 (1978).

[66] D. E. Eastman, W. D. Grobman, J. L. Freeouf, and M. Erbudak, Phys. Rev. B 9, 3473 (1974); R. Ludeke, L. Ley, and K. Ploog, Solid State Commun. 28, 57 (1978).

[67] A.Savitzky and M. J. E. Golay, Anal. Chem. 36, 1627 (1964).

[68] G. Le Lay, Surf. Sci. 132, 169 (1983); M. Hanbücken and G. Le Lay, *ibid* 168, 122 (1986) and references therein.

[69] L. Braicovich, C. M. Garner, P. R. Skeath, C. Y. Su, P. W. Chye, I. Lindau, and W. E. Spicer, Phys. Rev. B 20, 5131 (1979).

[70] B. Carrière, J. P. Deville, M. Hanbücken, and G. Le Lay, in The Structure of Surfaces II: Proceedings of the 2nd International Conference on the Structure of Surfaces (ICSOS II), Amsterdam, the Netherland, ed. by J. F. van der Veen and M. A. Van Hove (Springer-Verlag, New York, 1988).

[71] M. Iwami, T. Terada, H. Tochihara, M. Kubota, and Y. Murata, Surf. Sci. 198, 115 (1988).

[72] G. Mathien, R. Contini, J. M. Layet, P. Mathiez, and S. Giorgion, J. Vac. Sci. Technol. A6, 2904 (1988).

[73] K. Okuno, T. Ito, M. Iwami, and A. Hiraki, Solid State Comm. 34, 493 (1980).

[74] K. Nakashima, M. Iwami, and A. Hiraki, Thin Soild Films, 25, 423 (1975). P. Perfetti, S. Nannarone, F. Patella, C. Quaresima, M. Capozzi, A. Savoia, and G. Ottaviani, Phys. Rev. B 26, 1125 (1982).

[75] K. Oura and T. Hanawa, Surf. Sci. 82, 202 (1979).

[76] M. Hanbücken, Z. Imam, J. J. Metois, and G. Le Lay, Surf. Sci. 162, 628 (1985).

[77] T. J. Magee and J. Peng, Phys. Stat. Sol. (a) 49, 313 (1978).

[78] For a review, see A. Hiraki, Surf. Sci. 168, 74 (1986), Surf. Sci. Rep. 3, 357 (1984).

[79] G. Ottaviani, Thin Solid Films, 140, 3 (1986).

[80] J. -J. Yeh, J. Hwang, R. Cao, K. A. Bertness, and I. Lindau, J. Vac. Sci. Technol. A 6, 1557 (1988).

[81] L. Calliari, M. Sancrotti, and L. Braicovich, Phys. Rev. B 30, 4885 (1984).

[82] I. Wagner, H. Stasiewski, and B. Abeles, Phys. Rev. B 28, 7080 (1983).

[83] M. Láznicka, Surf. Sci. 87, L269 (1979).

[84] B. Goldstein and D. Szostak, Surf. Sci. 99, 235 (1980).

[85] H. J. Clemens, Solid State Comm. 51, 483 (1984).

[86] M. Foller, W. Beyer, J. Herion, and H. Wagner, Surf. Sci. 178, 47 (1986).

[87] K. Winer, I. Hirabayashi, and L. Ley, Phys. Rev. B 38, 7680 (1988).

[88] H. Schade and J. I. Pankove, Surf. Sci. 89, 643 (1979).

[89] L. Ley in The Physics of Hydrogenated Amorphous Silicon II, Topics in Applied Physics Vol. 56, ed. by J. D. Joannopoulos and G. Lucovsky (Springer-Verlag, Berlin Heidelberg, 1984).

[90] F. J. Himpsel, G. Hollinger, and R. A. Pollak, Phys. Rev. B 28, 7014 (1983).

[91] R. J. Nemanich, Semiconductors and Semimetals, Vol. 21C, Chap. 11 (Academic Press, 1984).

[92] S. -T. Lee, G. Arai, M. G. Mason, R. Benbow, and Z. Hurych, Phys. Rev. B 23, 505 (1981). M. G. Mason, Phys. Rev. B 27, 748 (1983).

[93] G. K. Wertheim, S. B. DiCenzo, and S. E. Youngquist, Phys. Rev. Lett. 51, 2310 (1983). H. Roulet, J-M. Mariot, G. Dufour, and C. F. Hague, J. Phys. F 10, 1025 (1980).

[94] L. Ley, S. P. Kowalczyk, F. R. McFeely, and D. A. Shirley, Phys. Rev. B 10, 4881 (1974).

[95] The binding energies cited for the two components of the Au 5f levels are determined from their individual positions in the spectra, not from a curve fitting routine.

[96] C. E. Moore, Atomic Energy Levels, National Bureau of Standard Circular No. 467 (U. S. CPO, Washington, D. C., 1958).

[97] B. Carrière, J. P. Deville, and A. El Maachi, Surf. Sci. 168, 149 (1986).

[98] M. Iwami, M. Kubota, T. Koyama, H. Tochihara, and Y. Murata, Phys. Rev. B 38, 1047 (1988).

[99] K. N. Tu, Appl. Phys. Lett. 27, 221 (1975).

[100] L. J. Brillson, Surf. Sci. Rep. 2, 123 (1982).

[101] M. del Giudice, J. J. Joyce, and J. H. Weaver, Phys. Rev. B 36, 4761 (1987).

[102] N. M. Pavindra, C. Ance, J. P. Ferraton, A. Donnadieu, and S. Robin, Phys. Stat. Sol. (b) 115, 347 (1983).

[103] C. C. Tsai, R. J. Nemanich, and M. J. Thompson, J. Vac. Sci. Technol. 21, 632 (1982).

[104] R. M. Feenstra and G. S. Oehrlein, Appl. Phys. Lett. 47, 97 (1985). R. Wiesendanger, L. Rosenthaler, H. R. Hidber, H. -J. Güntherodt, A. W. McKinnon, and W. E. Spear, J. Appl. Phys. (to be published)

[105] J. Kanicki, in Amorphous Silicon Semiconductor-Pure and Hydrogenated: Material Research Society Symposia Proceedings, Vol. 95, ed. by A. Madan, M. Thompson, D. Adler, and Y. Hamakawa (Pittsburgh, Pa., Material Research Society, 1987).

[106] A. Franciosi, D. J. Peterman, and J. H. Weaver, J. Vac. Sci. Technol. 19, 657 (1981).

[107] A. Franciosi, D. J. Peterman, J. H. Weaver, and V. L. Moruzzi, Phys. Rev. B, 25, 4981 (1982). A. Franciosi, J. H. Weaver, D. G. O'Neill, F. A. Schmidt, O. Bisi, and C. Calandra, *ibid*, 28, 7000 (1983). J. H. Weaver, A. Franciosi, and V. L. Moruzzi, *ibid*, 29, 3293 (1984).

[108] P. Wetzel, C. Pirri, J. C. Peruchetti, D. Bolmont, and G. Gewinner, J. Vac. Sci. Technol. A 5, 3359 (1987).

[109] A. Franciosi, S. Chang, P. Phillip, C. Caprile, and J. Joyce, J. Vac. Sci. Technol. A 3, 933 (1985).

[110] R. Kärcher and L. Ley, Solid State Comm. 43, 415 (1982).

[111] L. Yang, B. Abeles, W. Eberhardt, and H. Stasiewski, Phys. Rev. B 35, 9395 (1987).

[112] A. Franciosi and J. H. Weaver, Physica 117B & 118B, 846 (1983).

[113] S. Valeri, L. Grandi, and C. Calandra, J. El. Spect. Rel. Phe. 43, 121 (1987).

[114] A. C. Switendick, in the Hydrogen in Metals I, Vol. 28 of Topics in Applied Physics, ed. by G. Alefeld and J. Volkl (Springe, New York, 1979).

[115] G. Gewinner, J. C. Peruchetti, A. Jaegle, and A. Kalt, Surf. Sci. 78, 439 (1978). *ibid* 122, 383 (1982).

[116] G. Hollinger and F. J. Himpsel, J. Vac. Sci. Technol. A 1, 640 (1983).

[117] P. Wetzel, C. Pirri, J. C. Peruchetti, D. Bolmont, and G. Gewinner, Surf. Sci. 178, 27 (1986).

[118] D. Ballutaud, G. Moulin, and M. Aucouturier, Surf. Sci. 178, 70 (1986).

[119] J. Finster, O. Schulze, and A. Meisel, Surf. Sci. 162, 671 (1985).

[120] J. Barth, F. Gerken, K. L. I. Kobayashi, J. H. Weaver, and B. Sonntag, J. Phys. C 13, 1369 (1980). D. Chandesris, J. Lecante, and Y. Petroff, Phys. Rev. B 27, 2630 (1983). H. Sugawara, K. Naito, T. Miya, A. Kakizaki, I. Nagakura, and T. Ishii, J. Phys. Soc. Jpn. 53, 279 (1984).

[121] S. Raaen and V. Murgai, Phys. Rev. B 36, 887 (1987).

[122] See a recent review of scanning tunneling microscopy by R. M. Tromp, J. Phys.: Condens. Matter, 1, 10211 (1989).

[123] G. Rossi, I. Abbati, L. Braicovich, I. Lindau, and W. E. Spicer, Surf. Sci. 112, L765 (1981).

[124] A. -B. Yang, Ph. D. Thesis (Iowa State University, 1989).

[125] G. Rossi, L. Caliari, I. Abbati, L. Braicovich, I. Lindau, and W. E. Spicer, Surf. Sci. 116, L202 (1982).

[126] F. Nava, T. Tien, and K. N. Tu, J. Appl. Phys. 57, 2018 (1985).

[127] R. Wiesendanger, L. Rosenthaler, H. R. Hidber, H. -J. Güntherodt, A. W. McKinnon, and W. E. Spear, (submitted to J. Appl. Phys.)

[128] H. Oheda, Phys. Rev. B 39, 10179 (1989).

[129] L. S. O. Johansson, E. Landemark, C. J. Karlsson, and R. I. G. Uhrberg, Phys. Rev. Lett. 63, 2092 (1989).

ACKNOWLEDGEMENTS

I sincerely thank Professor David W. Lynch for his valuable discussions and inspiration on this work. His sagacious supervision has not only broadened and strengthened my knowledge in physics, but also elevated my attitude toward outstanding scientific research. Being under his advice, I truly believe that having a professional carrer as an experimental physicist in the future will be promising.

The substantial assistance of Dr. Clifford G. Olson during my research at Synchrotron Radiation Center is heartily appreciated. It was a privilege that I could partake in the final assembly of the Seya/ERG monochromator, designed by Dr. Olson. I learned a lot from him, especially on vacuum technology and caring of instruments, knowledge essential to obtaining exceptional results.

I am indebted to members of the Synchrotron Radiation Center, who have provided many helping hands and a hospitable working environment. The Synchrotron Radiation Center is operated by the University of Wisconsin under NSF contract no. DMR-80-20164.

Saibal Mitra's assistance in making the a-Si:H samples is acknowledged.

Most of all, no words can express my gratitude to my wife, Wen-Ling, and parents-in-law, Mr. and Mrs. Chen, who have given their firm support and encouragement during the extended graduate study. Now pursuing a Ph.D. degree in the Department of Child Development, Wen-Ling not only has to study for the degree, but also takes good care of our two-year old son, David. I owe her too much.

- END -

DATE FILMED

11 / 15 / 90